Technische Universität München
Institut für Energietechnik

Lehrstuhl für Thermodynamik

Experimental Investigation of Ignition and Combustion of Diesel-Piloted Natural Gas Jets in a Rapid Compression-Expansion Machine

Georg Fink

Vollständiger Abdruck der von der Fakultät für Maschinenwesen der Technischen Universität München zur Erlangung des akademischen Grades eines

DOKTOR – INGENIEURS

genehmigten Dissertation.

Vorsitzender:

Prof. Dr.-Ing. Johannes Fottner

Prüfer der Dissertation:

Prof. Dr.-Ing. Thomas Sattelmayer
Prof. Dr. techn. Helmut Eichlseder

Die Dissertation wurde am 16.10.2020 bei der Technischen Universität München eingereicht und durch die Fakultät für Maschinenwesen am 02.02.2021 angenommen.

Danksagung

Diese Arbeit basiert auf Erkenntnissen, welche im Zuge des Forschungsprojektes „FlexDi: Flexible direkteinspritzende Motoren für die Schifffahrt“ während meiner Zeit am Lehrstuhl für Thermodynamik der TU München entstanden sind. Das Forschungsvorhaben wurde gemeinsam mit MTU Friedrichshafen, Woodward L’Orange und dem Lehrstuhl für Verbrennungskraftmaschinen der TU München durchgeführt. Die Förderung durch das BMWi im Rahmen des Programmes „Maritime Technologien der nächsten Generation“ (FKZ: 03SX387C) sei an dieser Stelle dankend erwähnt.

In erster Linie gilt mein Dank Prof. Thomas Sattelmayer für das entgegengebrachte Vertrauen und die Möglichkeit, dieses Forschungsprojekt von der Beantragung bis zum Abschluss eigenverantwortlich gestalten zu dürfen. Die fachliche Unterstützung und kritische Auseinandersetzung mit meiner Arbeit haben diese maßgeblich vorangebracht. In diesem Zuge möchte ich auch Prof. Helmut Eichlseder für die inhaltliche Begutachtung, und Prof. Johannes Fottner für die Übernahme des Vorsitzes der Prüfungskommission meinen herzlichen Dank aussprechen.

Zahlreiche Personen haben direkt und indirekt zum Gelingen dieser Arbeit beigetragen. Vielen Dank an Helga Bassett und Sigrid Schulz-Reichwald für die Unterstützung bei organisatorischen und administrativen Angelegenheiten, sowie stellvertretend für die Werkstatt an Jens Hümmer, Gerhard Giel und Thomas Schleussner für den Fleiß und Schweiß beim Aufbau des Prüfstandes. Manuel Boog, Joachim Schwarte, Ingmar Berger, Stefan Gleis und Stephanie Frankl gebührt mein spezieller Dank für die konstruktive Kollaboration im Forschungsverbund.

Ganz besonders hervorzuheben ist die freundschaftliche Zusammenarbeit mit Michael Jud, der durch zahlreiche, manchmal auch kontroverse Diskussionen und Anregungen maßgeblich zum Erfolg unseres gemeinsamen Forschungsprojektes und damit auch dieser Arbeit beigetragen hat. Durch die tägliche Arbeit am Lehrstuhl, gemeinsame Konferenzbesuche, Reisen und manche ausgelassene Feier sind einige tiefe Freundschaften entstanden. Insbesondere die Erlebnisse mit Nicolai

Stadlmair, Frederik Berger, Tobias Hummel und Noah Klarmann sind untrennbar mit dieser Zeit verknüpft.

Liebe Tamara, du warst über die gesamte Promotionszeit an meiner Seite, hast mich stets unterstützt und mir insbesondere während der letzten Phase den Rücken freigehalten. Ich bin stolz darauf, dass wir die Herausforderungen der langen Fernbeziehung so erfolgreich gemeistert haben.

Obwohl hier erst zum Schluss angeführt, haben meine Eltern doch den größten Anteil daran, dass diese Arbeit überhaupt entstehen konnte. Mein tiefster Dank euch beiden für die unermüdliche jahrelange Unterstützung.

Dornbirn, März 2021 Georg Fink

Kurzfassung

Beim High-Pressure Dual-Fuel (HPDF) Brennverfahren wird Erdgas unter hohem Druck nahe dem oberen Totpunkt in den Brennraum eines Verbrennungsmotors eingebracht und mittels einer kleinen Menge Diesel-Pilotkraftstoff entzündet. Durch die Überlappung von Gemischbildung und Verbrennung wird Flammenlöschen an den kalten Brennraumwänden, und damit der beim Erdgas-Homogenbrennverfahren auftretende Methanschlupf, vermieden. Das Potenzial dieses Brennverfahrens wurde bereits erfolgreich nachgewiesen, jedoch fehlt es bislang an einer detaillierten Beschreibung der ablaufenden Prozesse und der Möglichkeiten, diese zu beeinflussen. Das dafür notwendige Verständnis wird in dieser Arbeit anhand von Grundlagenuntersuchungen zweier isolierter Kraftstoffstrahlen in einer schnellen Kompressions-Expansions-Maschine generiert.

Abhängig vom Zündverhalten des reinen Dieselpiloten kann die für eine stabile Zündung notwendige Interaktion zwischen Diesel- und Gasstrahl beschrieben werden. Bei starker Strahlinteraktion scheitert die Selbstzündung des Pilotkraftstoffes. Darüber hinaus zeigt sich eine nur marginale Beeinflussbarkeit von Zündort und initialer Flammenausbreitung am Gasstrahl durch die Betriebsbedingungen, die Strahlanordnung und den relativen Injektionszeitpunkt der beiden Kraftstoffe. Als direkte Konsequenz lässt sich die Form der Wärmefreisetzung an einem sich frei ausbreitenden Erdgasstrahl alleine durch dessen Vormischgrad beschreiben. Mittels einer umfassenden Analyse von simultan fortschreitender Mischung, Verbrennung und Schadstoffbildung lassen sich Designrichtlinien formulieren. Diese werden erfolgreich auf den speziellen Fall eines wandgeführten Strahles angewandt, was insbesondere bei starker Vormischung Vorteile bietet.

Abstract

With high-pressure dual-fuel (HPDF) combustion, natural gas is injected at high pressure directly into the combustion chamber of a reciprocating engine close to top dead center and is ignited by a small amount of diesel pilot fuel. The direct coupling of mixture formation and combustion allows to prevent methane slip, typically observed with homogeneous-charge natural gas combustion and caused by flame quenching at the cold walls. Even though low emissions and high engine performance have been demonstrated for HPDF combustion, a detailed description of the processes involved and the means to influence them is not available. In the present work, this understanding is generated based on a fundamental investigation of two single fuel jets in a rapid compression-expansion machine.

Stable ignition is limited to a certain interaction between the two jets and governed by the ignition characteristics of the bare diesel pilot. Strong interaction between the jets causes pilot fuel auto-ignition to fail. If pilot ignition is successful, the natural gas jet ignition location and initial flame propagation are found to be only marginally affected by the operating conditions, jet arrangement and relative fuel injection timing. As a direct consequence, the heat release rate is influenced only by the degree of premixing of the natural gas jet. The combined analysis of simultaneously progressing mixture, combustion and pollutant formation by experimental and numerical means is used to formulate design objectives. These are successfully applied to the combustion chamber design for a wall-bounded natural gas jet, which is shown to be particularly beneficial at partially-premixed combustion.

Contents

List of Figures

List of Tables

Nomenclature

Abbreviations

0D/3D	zero/three-dimensional
AMR	adaptive mesh refinement
AMS	accelerometer mass spectroscopy
ASOI	after start of injection
BTE	brake thermal efficiency
CFD	computational fluid dynamics
EGR	exhaust gas recirculation
EOI	end of injection
FPGA	field-programmable gate array
GHG	greenhouse gas
GIMEP	gross indicated mean effective pressure
GWP	global warming potential
HCCI	homogeneous charge compression ignition
HPDF	high-pressure dual-fuel
IMO	International Maritime Organization
IPPC	Intergovernmental Panel on Climate Change
KH/RT	Kelvin-Helmholz/Rayleigh-Taylor
LIF	laser-induced fluorescence
LPDF	low-pressure dual-fuel
LPSI	low-pressure spark ignition
LTC	low-temperature combustion
MFB	mass fraction burned
NG	natural gas
NMHC	non-methane hydrocarbons
ODE	ordinary differential equation
OP	operating point
PAH	polyzyclic aromatic hydrocarbons
PM	particle matter
PPC	partially-premixed combustion

PSR	perfectly stirred reactor
RANS	Reynolds-averaged Navier-Stokes
RCEM	rapid compression-expansion machine
RNG	re-normalization group
SCRE	single cylinder research engine
SG	shadowgraph
SI	spark ignition
SOE	start of energizing
SOI	start of injection
TDC	top dead center
TR	trigger
TWC	three-way catalyst
UHC	unburned hydrocarbons
UV	ultraviolet

Latin Letters

c_v	[J/kg/K]	isochoric heat capacity
c_p	[J/kg/K]	isobaric heat capacity
d	[mm]	nozzle diameter
D	[mm]	maximum jet diameter
H	[J]	enthalpy
$\dot{H}_{HR}$	[W]	heat release rate
h	[J/kg]	specific enthalpy
h_f	[j/kg]	specific enthalpy of formation
I	[A]	injector current
J	[−]	image pixel intensity
K	[−]	proportionality constant
L	[mm]	imaging distance
m	[kg]	mass
$\dot{m}$	[kg/s]	mass flow rate
M	[kg/mol]	molar mass
$\dot{M}$	[$kg \cdot m/s^2$]	momentum flow rate
n	[−]	refractive index
p	[bar]	pressure
Q	[J]	heat

R_s	[J/kg/K]	specific gas constant
s	[mm]	piston stroke
T	[K]	temperature
t	[s]	time, duration
t'	[−]	non-dimensional time
Δt	[s]	time shift/offset
u	[m/s]	longitudinal/axial flow velocity
U	[J]	internal energy
u	[J/kg]	specific internal energy
V	[m^3]	volume
v	[m^3/kg]	specific volume
w	[−]	fuel mass relative to full load
x	[mm]	distance in axial/downstream direction
y	[mm]	distance in radial/lateral direction

Greek Letters

α	[°]	angle between natural gas and pilot jets
δ	[°]	angular deflection
ϵ	[−]	compression ratio
Γ	[−]	penetration constant
γ	[−]	power factor for gamma correction
κ	[−]	ratio of specific heats
λ	[W/m/K]	thermal conductivity
ν	[−]	molecule vibratory state
ϕ	[−]	fuel-air equivalence ratio
ρ	[kg/m^3]	density
τ	[s]	delay
θ	[°ASOI]	crank angle

Subscripts

$(\ldots)_{\mathrm{a}}$	ambient
$(\ldots)_{\mathrm{ad}}$	adiabatic
$(\ldots)_{\mathrm{ax}}$	axial

$(\ldots)_{\mathrm{CG}}$	crevice zone to gap zone
$(\ldots)_{\mathrm{ch}}$	charge
$(\ldots)_{\mathrm{dwell}}$	mixture dwell
$(\ldots)_{\mathrm{eff}}$	effective
$(\ldots)_{\mathrm{ent}}$	entrainment
$(\ldots)_{\mathrm{eq}}$	equivalent
$(\ldots)_{\gamma}$	gamma-corrected
$(\ldots)_{\mathrm{GC}}$	gap zone to crevice zone
$(\ldots)_{\mathrm{g}}$	global
$(\ldots)_{\mathrm{ign}}$	ignition
$(\ldots)_{\mathrm{i,j}}$	counting indices
$(\ldots)_{\mathrm{IM}}$	isentropic zone to mixing zone
$(\ldots)_{\mathrm{inj}}$	injection
$(\ldots)_{\mathrm{lift}}$	lift-off
$(\ldots)_{\mathrm{m}}$	mean
$(\ldots)_{\mathrm{MFB80}}$	80 percent mass fraction burned
$(\ldots)_{\mathrm{MB}}$	mixing zone to burned zone
$(\ldots)_{\mathrm{n}}$	nozzle
$(\ldots)_{\mathrm{N}}$	normalized
$(\ldots)_{\mathrm{pen}}$	jet penetration
$(\ldots)_{\mathrm{P}}$	pilot
$(\ldots)_{\mathrm{rad}}$	radial
$(\ldots)_{\mathrm{s}}$	specific
$(\ldots)_{\mathrm{st}}$	stoichiometric
$(\ldots)_{\mathrm{steady}}$	steady-state jet
$(\ldots)_{\mathrm{tip}}$	leading flame tip
$(\ldots)_{\mathrm{w}}$	wall

Dimensionless Numbers

Re	Reynolds number
Ma	Mach number

1 Introduction

1.1 Motivation

Early efforts to minimize emissions from combustion engines were focused on substances hazardous to humans and the environment. But as the anthropogenic climate change continues to accelerate, the reduction of climate-active emissions becomes increasingly important. Since legislation and therefore new technologies for pollutant emission reduction were applied only slowly to heavy-duty applications in the past, modern heavy-duty engines are required both to become cleaner and emit less greenhouse gases at the same time. For example, global shipping contributes more than 15% to global SO_2 emissions and about 12% to NO_x emissions, while its share on CO_2 emissions is only about 3%, according to a report by the International Maritime Organization (IMO) [95]. Apart from combustion technology, the choice of fuel has a strong influence on the emission characteristics. Among the alternative fuels globally available today, natural gas (NG) stands out since it contains none or only very little sulfur and furthermore allows up to 28% lower specific CO_2 emissions relative to diesel fuel due to the low C/H-ratio of its main constituent methane [3]. In addition, the currently observed growth of infrastructure for liquefied natural gas as well as attractive market prices are important arguments for natural gas as a potential fuel for heavy-duty applications.

The use of alternative fuels with different and sometimes strongly varying properties entails new requirements to the combustion system. As the very high compression ratios required for controlled natural gas auto-ignition are not met by compression ignition engines, NG is usually premixed with air and the charge ignited by an ignition source. Although NG has a relatively high knocking limit, knocking still restricts the compression ratio of premixed NG combustion engines. Since natural gas quality and composition strongly depend on the fuel source, a considerable margin to the knocking limit must be guaranteed. Natural gas engines running on a stoichiometric mixture therefore usually suffer from poor thermal efficiency when compared to a diesel engine.

In order to increase the knocking limit and therefore the efficiency, heavy-duty natural gas engines often operate in lean-burn mode with fuel-air equivalence ratios down to $\phi = 0.5$ [43, 103, 104]. Moreover, such a lean mixture causes the fuel-specific heat capacity of the reacting mixture to increase and therefore the combustion temperature to be reduced, which is why lean-burn combustion is considered a low-temperature combustion (LTC) strategy. LTC strategies are applied to achieve low NO emissions since NO formation in the reacting zones as well as in the hot combustion products scales exponentially with temperature [49]. Unfortunately, the lower combustion temperature increases the flame's susceptibility to quenching close to the cold wall and especially in small gaps. This effect is particularly strong with natural gas since a high activation energy is required to split the chemically very stable methane molecule. As a consequence, unburnt methane emissions of lean-burn NG engines (methane slip) tend to be considerably elevated while very low levels of NO and soot are achieved [4].

Methane does not impose a direct health threat to humans, and is therefore traditionally not considered in many emission control regulations for unburned hydrocarbons (UHC) by explicitly excluding it via the definition of a limit value for non-methane hydrocarbons (NMHC, e.g. EPA TIER). However, methane is a climate-active gas with a strong global warming potential, which is why emission regulations are increasingly being extended to it (e.g. EURO IV). A substance's effect on global warming is commonly rated by the Global Warming Potential (GWP), defined as the energy added to the atmosphere by a substance relative to the energy input the same amount (mass) of CO_2 would cause. Since various substances experience a different lifetime in the atmosphere before decomposition, the GWP is usually integrated over a period of 20 or 100 years ($GWP_{20/100}$). The Intergovernmental Panel on Climate Change (IPCC) lists a GWP_{100} value of 34 for methane, which is considerably higher than in previous reports due to new insights on the climate-carbon feedback [73]. As methane is decomposed relatively fast in the atmosphere compared to CO_2, its short-term impact on global warming is even higher, reflected by a GPW_{20} of 86 [97].

As a consequence, the net greenhouse gas emissions of a natural gas engine strongly depend on the applied engine technology. Figure 1.1 shows the net greenhouse gas (GHG) benefit of various heavy duty NG engines compared to a diesel engine as a function of unburned CH_4 emissions. On-road natural gas engines are most frequently operated with a stoichiometric mixture, allowing the use of a three-way catalyst (TWC) that cuts down on NMHC and NO emissions. Even though stoichiometric operation limits methane slip from the combustion chamber, the TWC shows a very poor conversion efficiency of the stable CH_4 molecule. Since brake thermal efficiency (BTE) is restrained by knocking, the maximum GHG benefit is only about half of the value theoretically achievable by the lower carbon content. Larger natural gas engines in marine or locomotive applications are usually operated in lean-burn mode (low-pressure spark ignition - LPSI, low-pressure dual-fuel - LPDF) and thereby allow efficiencies comparable to those of a diesel engine. The wide range of specific CH_4 emissions reflects the achievements of methane slip mitigation in the last few years. Nevertheless, replacing a heavy-duty diesel engine with a lean-burn natural gas engine shows to be GHG-neutral at best. This analysis does not include the strong short-term effect of methane on global warming, since the GWP_{100} value was used. Furthermore, all presented data does not consider any greenhouse gas emissions caused by the natural gas supply chain. Fuel production, distribution and storage considerably increase the GWP of any NG application, especially when fracking is used.

Since methane oxidation catalysts are made from precious metals and require high engine-out temperatures, methane slip from the combustion chamber needs to be avoided first hand. This can only be achieved if lean mixtures are kept away from the cold chamber wall and the combustion chamber crevices. One way to control the mixture distribution in the combustion chamber is late admission of natural gas by direct-injection close to top dead center (TDC). If a small amount of directly injected diesel pilot fuel is used as ignition source, it is referred to as high-pressure dual-fuel (HPDF) combustion. With conventional HPDF the diesel pilot is injected first and auto-ignites before combustion is passed on to the natural gas jets by direct interaction with the hot pilot combustion products. After

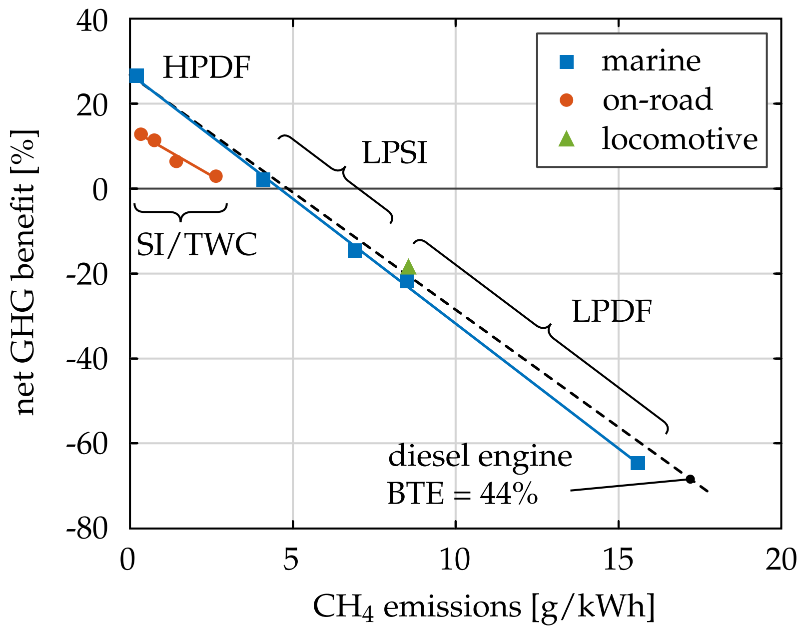

Figure 1.1: Impact of methane emissions on the net GHG benefit ($GWP_{100}(CH_4) = 34$) when replacing a conventional heavy duty diesel engine (BTE = 44%) with low-pressure dual-fuel (LPDF), low-pressure spark-ignition (LPSI), stoichiometric spark-ignition with three-way catalyst (SI/TWC) and high-pressure dual-fuel (HPDF) natural gas engines; adapted from [54] with data from [15,16,55,95,96].

the small amount of premixed NG is consumed, the main heat release is governed by mixture-limited burnout similar to conventional diesel combustion. This strong analogy with diesel combustion results in very similar heat release rates and allows high efficiencies at part load, since the global mixture quality does not need to be preserved by intake throttling. With HPDF the full theoretical net GHG benefit of natural gas over diesel fuel of about 28% can be realized, since very low CH_4 emissions of only 0.2 g/kWh have been demonstrated e.g. by the MAN ME-GI concept (see Fig. 1.1) [55].

While methane slip can be successfully avoided, the strong similarity of HPDF and diesel combustion causes comparable emission characteristics. It is therefore evident to assess the applicability of in-cylinder emission reduction methods developed for diesel engines by extensive research in the past. A wide range of equivalence ratios is involved in the mixture-limited reaction of a fuel jet. Oxygen deficiency in the core favors strong soot formation while only little NO is formed due to the low temperatures of the reacting rich mixtures. The diffusion flame covering the jet allows some of the soot to be oxidized while the associated high temperatures make this region the main source for NO. Exhaust gas recirculation (EGR) is considered a LTC strategy since it aims to cut down on NO emissions by reducing the oxygen partial pressure and thereby also the combustion temperature across all equivalence ratios. Even though the lower temperatures slow down the formation of soot – the primary component of particle matter (PM) emissions – as well, engine-out PM emissions increase with EGR. This so called NO/PM trade-off is caused by drastically reduced soot oxidation rates during burnout. Since soot oxidation requires excess oxygen and leads to high temperatures, it is impaired by any measure capable of suppressing NO formation.

As soot forms in the rich zones, some combustion strategies for direct fuel injection combine the use of EGR with increased pre-combustion mixing. Even with moderate mixing by ignition shortly after the end of fuel injection, partially-premixed combustion (PPC) has proven a viable way to escape the emission trade-off equally for diesel and HPDF combustion [22, 68]. In contrast to natural gas lean-burn combustion or diesel homogeneous charge compression ignition (HCCI), a heterogeneous mixture including rich zones is still present at the time of ignition. Although partially-premixed low-temperature combustion has demonstrated low PM and NO_x emissions, this strategy in turn suffers from increased CO and UHC (including unburned CH_4) emissions. Furthermore, consumption of the premixed zones is fast and results in harsh combustion events with high pressure rise rates and intense combustion noise. As a consequence, the application of PPC to diesel and HPDF combustion is mostly limited to low-load conditions.

Although conventional diesel and HPDF combustion are very similar and even show the same drawbacks at partially-premixed LTC, there are some major differences. Delaying the ignition for diesel PPC requires retarding the ignition kinetics via a reduced compression temperature or very high EGR rates. In contrast, partially-premixed HPDF can be realized by simply increasing the split between both injections at unaltered conditions in the combustion chamber. Furthermore, the HPDF combustion progress is determined by flame propagation within the natural gas jet starting from the pilot ignition location, and is neither spatially distributed nor determined by the kinetics of auto-ignition. The ability to directly influence the ignition timing, ignition location and thus the flame propagation has the potential to overcome the drawbacks of partially-premixed HPDF combustion. By igniting the leanest zones first and limiting the subsequent fuel conversion via controlled flame propagation, UHC and CO emissions may be minimized while avoiding harsh combustion events.

Since high-pressure dual-fuel combustion was first mentioned in the early nineties [35], research has been able to proof the potential and general emission characteristics of conventional and partially-premixed HPDF combustion [22, 36, 62]. As most of this past research was done on single cylinder and production engines, parameter variation flexibility was low and optical access not possible. In order to realize the full potential of HPDF combustion, a general understanding of the governing processes needs to be developed.

1.2 Research Focus

The present work aims to provide an in-depth understanding of the processes involved in HPDF combustion and thereby to identify the important factors that determine the evolution of mixture formation, ignition and combustion. This is achieved with simplified experiments under well defined, engine-like boundary conditions. A wide experimental range of operating conditions, injection parameters and geometrical jet arrangements is applied to generate a broad data base. Besides analyzing the combustion progress by means of heat release rates and simultaneous shadowgraph (SG) and OH* imaging, reactive computational fluid dynamics (CFD) simulations are used to complement the experimental observations. Since the experimental setup is not capable of providing emission data for reliable engine-out emission correlations, conclusions on the emission behavior have to be drawn from a combination of literature data review, implicit observations (e.g. soot luminescence or flame propagation) and numerical simulations.

The value of the insights gained from the fundamental study of two freely propagating fuel jets is demonstrated by the formulation of design guidelines for conventional and partially-premixed HPDF combustion.

These guidelines are applied to tailor the mixture field, ignition timing and ignition location of a wall-bounded natural gas jet. Even though the resulting wall contour design is not directly applicable to the combustion chamber of a HPDF engine, it shows that the drawbacks of partially-premixed HPDF can be directly addressed based on the conclusions from the fundamental study.

By providing an insight into the relevant processes, the investigations furthermore allow to formulate a phenomenological description of HPDF combustion in heavy-duty engine applications. For this purpose the complex process of mixture formation, ignition, reaction progress and pollutant formation is illustrated by a simplified sequence, sometimes referred to as a *conceptual model* in literature. Such phenomenological descriptions have proven to be a valuable tool for understanding and improving in-cylinder combustion processes.

1.3 Thesis Outline

The first background chapter sets off with a review of high-pressure natural gas injection, including the effects of mass flow variation, compressibility and under-expansion. This is followed by an introduction of existing phenomenological descriptions for conventional and partially-premixed diesel combustion. Besides explaining the basic features of such descriptions, they directly applicable to diesel pilot ignition and combustion in the context of HPDF. Due to some strong similarities between the combustion of directly injected diesel and natural gas, the diesel process is furthermore a good reference for the main HPDF combustion phase. The last part of the first chapter summarizes the available literature on HPDF combustion research.

The second chapter presents a detailed description of the experimental setup based on a rapid compression-expansion machine (RCEM). For the fundamental investigations, a mounting system that allows the flexible arrangement of two separate single hole injectors for diesel and natural gas fuel was designed. The design combines maximum variability for jet arrangement with good optical access. Furthermore, the simultaneous

SG and OH* imaging system is introduced along with the digital test rig control and data acquisition system.

A separate chapter is dedicated to the methods for experimental and numerical data evaluation. In order to gain reliable heat release rates from the pressure and position measurements, a multi-zone thermodynamic model that reflects the specific conditions in the RCEM combustion chamber was developed. The shadowgraph and OH* images are processed and superimposed by an automated routine, and a customized two-dimensional color map is used for representation and physical interpretation of the superimposed images. Valuable complementary information on the combined mixing and reaction progress is obtained from CFD simulations by an analysis of the fuel distribution in the ϕ-T parameter space.

Since a diesel fuel jet acts as the ignition source for the natural gas, the first results chapter is dedicated to diesel micro-pilot ignition and combustion. Apart from the isolated diesel pilot itself, the influence of the natural gas jet on pilot fuel ignition is examined. Based on these results, criteria for successful auto-ignition are formulated.

In conventional HPDF combustion the natural gas jet is ignited by direct interaction with the pilot fuel jet close to the injector orifice and before any of the jets reaches the chamber wall. Natural gas jet ignition, early flame development and combustion characteristics as a result of direct interaction with the pilot jet is investigated in Ch. 6 using a freely propagating jet pair. The results allow to identify the characteristics of heat release, flame propagation and flame luminosity with respect to jet arrangement, injection timing, combustion chamber conditions or injection pressure. A separate section covers the influence of the various parameters on soot luminosity, an indicator for the occurrence of particle matter in the reacting zones. The combined mixing and reaction progress, as well as related pollutant formation processes, are analyzed numerically.

Based on the insights from a freely propagating jet pair, a combustion chamber geometry for wall-bounded natural gas jet combustion is designed and tested in Ch.7. While the combustion chamber wall affects only the mixture-limited combustion and burnout phases in conventional

HPDF, it alters natural gas mixture formation already prior to ignition in partially-premixed HPDF. The wall contour can therefore be used to influence the spatial mixture distribution, ignition location and flame propagation if the natural gas is premixed. A variation of the injection timing with the wall-bounded natural gas jet demonstrates how soot formation is suppressed while peak heat release rates and unburnt CH_4 emissions are limited. At the end of this work, all insights are combined for a phenomenological description of conventional HPDF and wall-bounded partially-premixed HPDF combustion in large-bore engines at diesel-like conditions.

2 Background

This chapter aims to provide the theoretical background relevant for the present work, as well as to discuss the current state in high-pressure direct-injection combustion engine research. The interested reader is referred to standard textbooks for a broader view on combustion [74, 78, 102] or engine technology [43,65,77,110].

One major difference between the considered high-pressure dual-fuel combustion and other combustion strategies is the direct injection of gaseous fuel, which is not very common in state-of-the-art engine technology. However, non-reacting transient gaseous jets have been extensively investigated in the past due to their widespread technical relevance in different fields. They are introduced at the beginning of this chapter. The second part presents widely accepted phenomenological descriptions of conventional and partially premixed diesel combustion, which have been formulated based on a large amount of experimental data. They serve as a reference for diesel micro-pilot combustion, as well as for the mixture-limited combustion of a directly injected fuel jet in general. The chapter concludes with a short literature review on HPDF combustion research and how the present work attempts to generate a more comprehensive and universal understanding.

2.1 High-Pressure Natural Gas Direct-Injection

With HPDF combustion, natural gas is injected when the compression stroke is almost completed close to TDC. Since a short injection duration and fast mixture formation have to be realized, high injection pressures are necessary. This results in a choked nozzle with under-expanded flow, featuring a shock structure close to the orifice. The choked nozzle flow causes the mass flow rate to be independent of the combustion chamber back pressure, only affected by the density of the compressed gaseous fuel.

The injection rate is typically characterized by a fast increase in mass flow, followed by a plateau and a fast ramp-down at the end of injection. The duration of the plateau is usually in the order of the jet's convective timescale within the combustion chamber, causing a distinct jet structure to be formed. Hence the ramp-up and ramp-down can be considered independently, separated by a phase of stationary jet flow. If, in contrast, a close succession of the two ramps causes a strong spatial coupling, the resulting flow structure is referred to as a puff jet in the literature [28–30, 83].

Hereafter, the turbulent under-expanded transient gas jet is introduced by its different phases. The start of an incompressible turbulent jet is described first before separately considering the effect of compressibility and under-expansion. The impact of fast mass flow reduction at the end of injection on the structure and mixture formation is treated last.

2.1.1 The Transient Turbulent Jet

A large number of analytical and experimental studies on the abruptly started turbulent jet are available. The development of the jet structure can be described using the early photographic images by Rizk *et al.* [86], which are presented in Fig. 2.1. They show the formation of a turbulent colored water jet injected into a quiescent water chamber. A tip vortex forms already when the jet has penetrated only one diameter from the nozzle, followed by turbulent disturbances in the shear layer. As a consequence, the ratio of maximum jet diameter D and tip penetration length x_{tip} is initially very high. This relative jet diameter describes the jet's shape and is found to asymptotically approach a constant value of about 0.25 after the tip has penetrated 10-15 nozzle diameters d from the orifice. The value agrees with the cone angle of a steady-state turbulent jet at any position downstream of the transition length [89] and is therefore a strong indicator for self-similarity. The recordings further show a core region stabilizing upstream of approximately $8d$, which is again well in line with the characteristics of a steady-state turbulent jet. While the upstream region transitions towards self-similarity, the tip vortex is pushed further downstream.

The persistent dark color shading of the tip vortex seen in Fig. 2.1 indicates very limited entrainment of the surrounding fluid. This is in line with a model proposed by Turner [101], which was initially developed for transient laminar jets affected by buoyancy and later successfully applied to non-buoyant turbulent jets [105, 106]. As sketched in Fig. 2.2, this model divides the jet into a steady-state turbulent jet region mainly accountable for the entrainment, and a propagating and expanding spherical vortex at the tip. While the vortex moves away from the nozzle, the average concentration of the added mass flow from the steady-state region drops. This is the main cause of progressing mixture formation in the tip region, since the vortex itself shows poor entrainment of the surrounding fluid.

If Turner's model is assumed to be valid, the entrainment after the initial transition to self-similarity can be described by steady-state turbulent jet entrainment correlations. Ricou and Spalding [85] derive the following equation from a dimensional analysis for high Reynolds numbers:

$$\frac{\dot{m}}{x\dot{M}^{1/2}\rho_{\mathrm{a}}^{1/2}} = K. \tag{2.1}$$

In this correlation, $\dot{m}$ is the overall axial mass flow at a downstream position x within the jet, ρ_a the density of the ambient fluid and K a constant. Momentum conservation requires the axial momentum of the steady-state jet to be constant at any of its cross-sections. Therefore, the momentum flow rate $\dot{M}$ can be evaluated directly at the nozzle exit:

$$\dot{M} = \dot{M}_{\mathrm{n}} = \dot{m}_{\mathrm{n}} u_{\mathrm{n}} = \frac{\pi}{4} d^2 \rho_{\mathrm{n}} u_{\mathrm{n}}^2. \tag{2.2}$$

This results in a linear correlation between the entrainment rate $\dot{m}/\dot{m}_{\mathrm{n}}$ of a steady-state turbulent jet and the downstream position x:

$$\begin{aligned} \frac{\dot{m}}{\dot{m}_{\mathrm{n}}} &= K \left(\tfrac{4}{\pi}\right)^{1/2} \frac{x}{d} \left(\frac{\rho_{\mathrm{a}}}{\rho_{\mathrm{n}}}\right)^{1/2} \\ &= K_{\mathrm{s}} \frac{x}{d} \left(\frac{\rho_{\mathrm{a}}}{\rho_{\mathrm{n}}}\right)^{1/2}. \end{aligned} \tag{2.3}$$

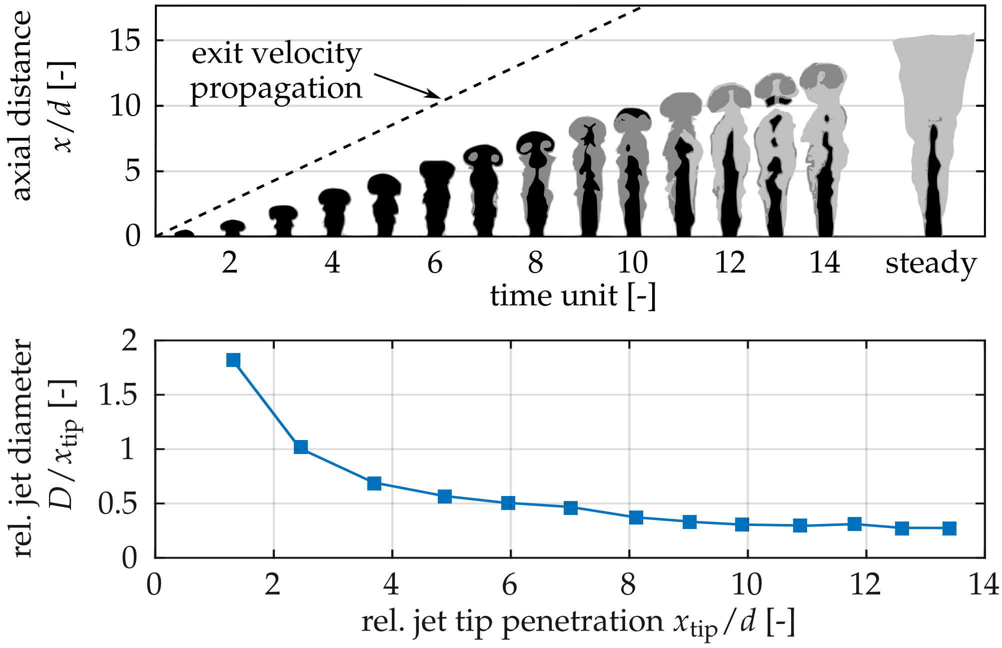

Figure 2.1: Recordings of a transient turbulent water jet by Rizk *et al.* [86] and evaluation of the relative jet diameter over the tip penetration distance.

Using a sophisticated experimental setup, Ricou and Spalding were able to determine the proportionality constant in this equation as $K_\mathrm{s} = 0.32$ by direct measurement of the entrained mass flow for Reynolds numbers in the range of $25,000 < Re < 80,000$.

The penetration of the transient jet after its transition to self-similarity ($x_\mathrm{tip}/d > 10$-15) can be assessed by a dimensional analysis as well. Hill *et al.* [33] argue that the nozzle momentum flow rate $\dot{M}_\mathrm{n}$ is the only property of the nozzle flow affecting jet penetration in the far field. Likewise, the only relevant property of the ambient fluid is its density ρ_a. By incorporating the observation of the relative jet diameter D/x_tip rapidly approaching a constant value (see Fig. 2.1), the correlation

$$\frac{x}{\left(\dot{M}/\rho_\mathrm{a}\right)^{1/4} t^{1/2}} = f\left(\frac{D}{x_\mathrm{tip}}\right) \rightarrow \text{const} \tag{2.4}$$

can be formulated. After rearranging for the jet penetration x_tip, the penetration constant Γ is introduced:

$$x_\mathrm{tip} = \Gamma \left(\frac{\dot{M}}{\rho_\mathrm{a}}\right)^{1/4} t^{1/2}. \tag{2.5}$$

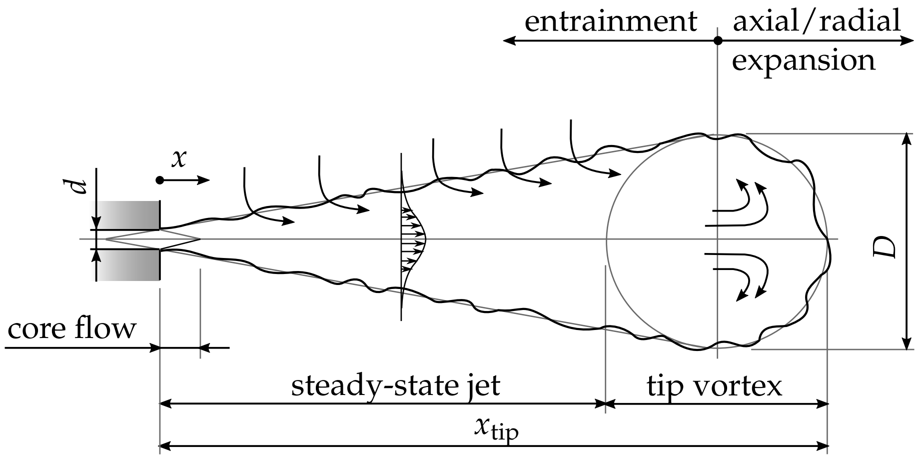

Figure 2.2: Sketch illustrating Turner's model [101] of a transient jet comprised of a steady-state jet region and a leading tip vortex.

By using Turner's model to describe the jet structure, the correlation from Ricou and Spalding for jet entrainment (Eq. 2.3) and the observation of D/x_{tip} asymptotically approaching 0.25-0.3, the penetration constant $\Gamma = 3.0$ can be analytically determined. Hill *et al.* confirmed this value by an evaluation of the jet tip penetration length from different experiments [33]. This shows that transient turbulent jets with high Reynolds numbers exhibit self-similarity once the jet tip penetration length x_{tip} exceeds approximately 10-15d.

2.1.2 Compressibility and Under-Expansion

The dimensional analysis leading to Eq. 2.5 indicates that the conditions at the nozzle exit do not have a direct effect on the later jet structure some diameters downstream the nozzle at a given momentum flow rate. Nevertheless the question arises, whether this still holds true for a compressible fluid being injected at a very high pressure ratio. In order to evaluate the influence of compressibility on the approach presented above, the exit momentum flow rate in Eq. 2.5 may be expressed with variable density:

$$\left(\frac{x}{d\left(\frac{\rho_{\text{n}}}{\rho_{\text{a}}}\right)^{1/2}}\right) = \Gamma\left(\frac{\pi}{4}\right)^{1/4}\left(\frac{u_{\text{n}}t}{d\left(\frac{\rho_{\text{n}}}{\rho_{\text{a}}}\right)^{1/2}}\right)^{1/2} . \tag{2.6}$$

The selected representation of this equation shows that the effect of compressibility can be isolated by the introduction of an equivalent nozzle diameter d_{eq}:

$$d_{\mathrm{eq}} = d \cdot \left(\frac{\rho_{\mathrm{n}}}{\rho_{\mathrm{a}}}\right)^{1/2}. \tag{2.7}$$

This equivalent nozzle diameter is a well-established scaling quantity for steady-state jets with non-uniform density and temperature. Hill *et al.* [33] checked axial velocity and concentration profiles from different authors for scalability with the equivalent diameter scaling assumption. The assumption was found to hold true downstream of $20d$ even for strongly under-expanded jets with a pressure ratio as high as 1:70, when the near-nozzle flow shows a considerable widening of the jet diameter followed by a strong vertical shock. However, this structure disappears after 1-$3d$ and has no persistent effect on the mean flow properties further downstream. In their conclusions Hill *et al.* state that the "jet flow apparently is able in its downstream experience to act as though it had completely forgotten the details of its origin".

It can therefore be expected that Eq. 2.5 applies to highly under-expanded transient jets as well – even with the same value for the penetration constant Γ as the one determined for the uniform density turbulent jet. Figure 2.3 shows that the experimental penetration constant is close to the theoretical value of 3.0 for three different data sets. Miyake *et al.* [67] used two different nozzle diameters to inject natural gas into a mixture of nitrogen and helium at a velocity of 409 m/s. This results in a density ratio of 3.2 and Reynolds numbers larger than 20,000. Only after the end of injection at 4.0 ms (equivalent to 0.063 $\mathrm{s}^{1/2}$ in the square root representation) the measurements start to deviate from the straight correlation line. The other two data-sets were recorded in a pressurized cell with a wall close to the natural gas jets injected into an air charge, similar to the confined jets in an engine environment. Even though the wall seems to slightly retard the penetration for different pressure ratios of 1.5 to 5.4 [72] and 2 to 8 [17], the jet tip location is still well described by the penetration constant $\Gamma = 3.0$.

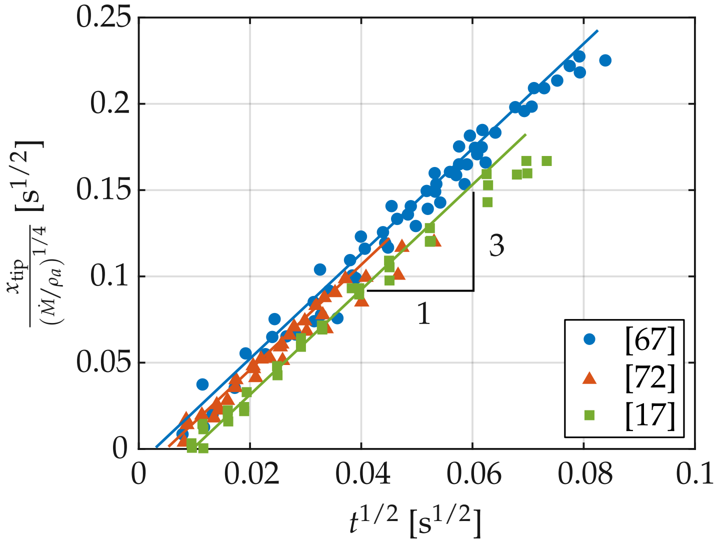

Figure 2.3: Corrected jet tip penetration over the square root of time for a graphical representation of the penetration constant $\Gamma = 3.0$; adapted from [33] with experimental data by Miyake *et al.* [67], Ouellette [72] and Chepakovich [17].

2.1.3 Mass Flow Reduction and End of Injection

The fuel mass flow rate ramp-down at the end of injection governs the late mixture formation process and thus – in the context of HPDF – the burnout or even late flame propagation phases. While an increase of the mass flow rate causes low entrainment due to fuel accumulating in a propagating vortex structure [12, 109](see also Sec. 2.1.1), entrainment is augmented if the mass flow rate is reduced [7, 10, 11]. Based on the cross-sectional velocity measurements and optical recordings by Borée *et al.* [11], the reason for this effect is briefly introduced hereafter. They investigated the response of a stationary turbulent jet to a sudden velocity decrease at the nozzle exit, corresponding to a reduction of the Reynolds number from 12,000 to 6,000.

In the experiment of Borée *et al.*, the sudden mass flow reduction was realized in about 30 ms as shown in Fig. 2.4. For a qualitative understanding of the jet's response to this ramp, the flow was visualized with laser-induced fluorescence (LIF). During the rapid decrease of the nozzle flow velocity, the vorticity in the shear layer at the outlet changes abruptly and the core flow of the jet is strained. The shear layer disturbed this way rolls up to form a vortex structure. This flow structure is carried downstream at the convection speed of the slow jet (u_2), while the

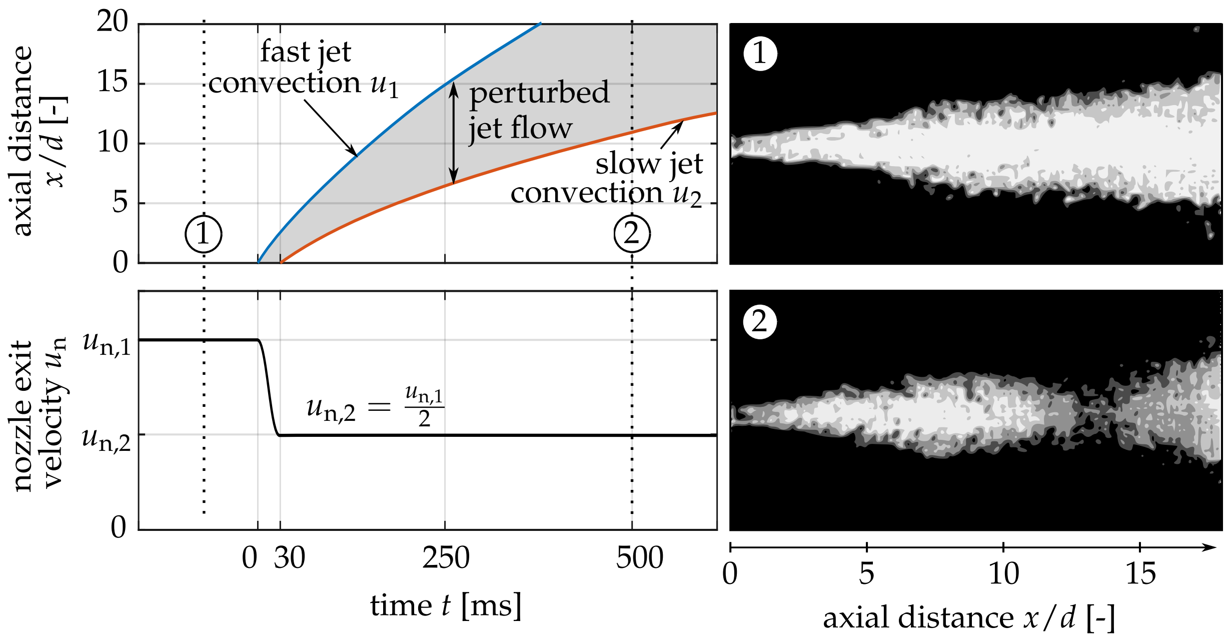

Figure 2.4: Propagation of the jet flow perturbation caused by a sudden nozzle exit velocity decrease (left) and mean LIF images before and 500 ms after the velocity reduction (right) [11].

beginning of the perturbation propagates at the convection speed of the fast jet (u_1). The local extent of the non-stationary, perturbed jet flow region therefore increases continuously due to the difference in propagation speed. This behavior can be clearly observed from the two mean LIF images in the same figure, which were obtained from multiple instantaneous recordings of consecutive measurements. The steady-state jet flow prior to the flow rate reduction is shown in ① and the jet structure 500 ms after the beginning of the ramp-down is presented in ②. While the upstream region has already returned to the new quasi-steady state at this point in time, a considerable reduction of the jet diameter is apparent further downstream.

The mean velocity profiles measured at different positions downstream allow a more detailed analysis. By defining a non-dimensional time t' Borée *et al.* [11] were able to prove that the evolution of the radial profiles of the mean velocity is independent of the downstream position if $x/d > 20$:

$$t' = \frac{t - t_1(x)}{t_2(x)}, \text{ where } \begin{array}{l} t_1(x) = t\left(\frac{u_{ax}(x,t)}{u_{ax}(x,0)} = 0.6\right) \\ t_2(x) = \frac{x}{u_{ax}(x,\infty)} \end{array}. \tag{2.8}$$

The temporal evolution of the mean axial and radial velocity profiles at $x/d = 30$ is presented in Figure 2.5. After the approach of the perturbation, the center-line axial velocity shows a small undershoot, which cannot be detected on larger radii. When comparing the radial profiles of the axial velocity during the passage of the perturbation, they are found to scale very well with the center-line value. Judged by the axial velocity, the jet width is therefore not reduced at any time. Nevertheless, the strain due to rapid axial velocity reduction causes a considerable increase of radial inflow of the surrounding fluid, evident from the temporary dip in radial velocity across the whole cross-section. The dropping jet width observed in Fig. 2.4 at $x/d > 10$ is therefore caused by an enhanced radial entrainment. The radial inflow leads to strong dilution which manifests in a lower fluorescence.

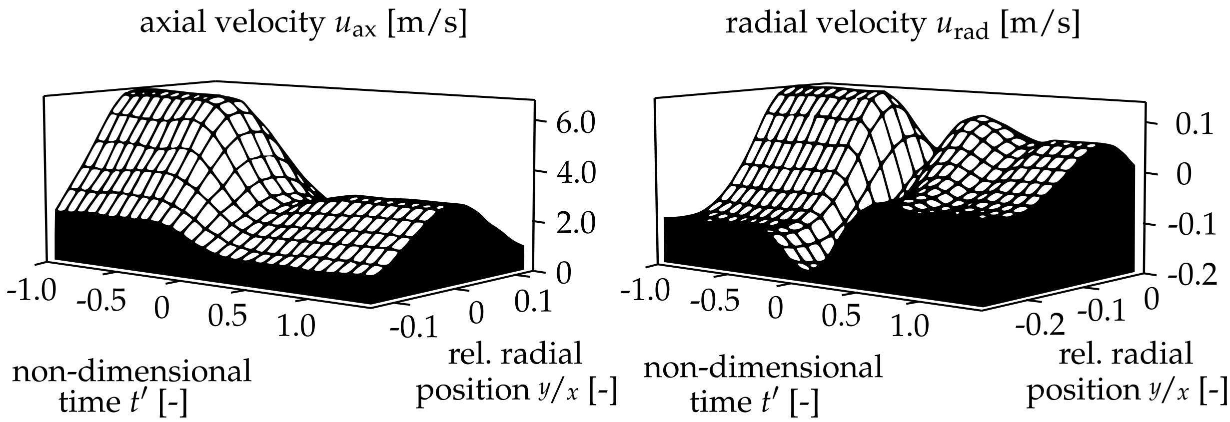

Figure 2.5: Evolution of the radial profiles of the mean axial and radial velocity at $x/d = 30$ in response to a sudden nozzle exit velocity decrease, normalized by the non-dimensional time t' and the relative radial position y/x [11].

2.2 Phenomenological Description of Diesel Combustion

In the last century, diesel combustion has been one of the most important technologies for propulsion and power generation. This is one reason why within this same period considerable research effort has been allocated to understanding the physical and chemical processes involved. Only recently, progress in optical diagnostics has provided ever more detailed insight into the mixing, ignition, combustion and pollutant formation processes. Based on such optical investigations, several phenomenological descriptions have been proposed [13,14,18,37,47,76,99]. These descriptions have proven useful as a foundation of understanding and modeling the processes responsible for diesel engine performance and pollutant emissions. As a consequence, a wide variety of alternative operating strategies to conventional diesel combustion have been developed. In this section a phenomenological description of conventional diesel combustion based on the work by Dec [18] is presented along with an extension to partially-premixed low-temperature diesel combustion by Musculus *et al.* [69].

2.2.1 Conventional Diesel Combustion

Dec introduced a phenomenological description for conventional diesel combustion in 1997 [18], and thereby fundamentally corrected the prevailing understanding of the jet structure and combustion process. Later investigations have confirmed his conclusions, even though they also led to minor corrections and refinements. Hereafter, Dec's description is introduced based on the slightly updated version by Musculus *et al.* [69] without explicitly mentioning the numerous sources that were compiled in their comprehensive review papers. The injector needle lift curve, heat release rate and geometrical scale shown in Fig. 2.6 represent actual measurements from one specific research engine. Therefore, the timings displayed in degrees after start of injection (°ASOI) are not directly applicable in general.

The left column in Fig. 2.6 illustrates a typical heat release rate and accompanying diesel jet evolution up to quasi-stationary diesel combustion in a heavy-duty engine, where the combustion chamber size guarantees a free penetration length of more than $\sim 50\,\mathrm{mm}$. Conventional diesel combustion is characterized by single injection initiated shortly before TDC with no or relatively low EGR. This causes a short ignition delay and therefore most of the fuel to be burned in mixture-limited combustion. Conventional diesel combustion therefore always shows a clearly negative mixture dwell $\Delta t_{\mathrm{dwell}}$, defined as the offset between the end of injection (EOI) and the time of ignition.

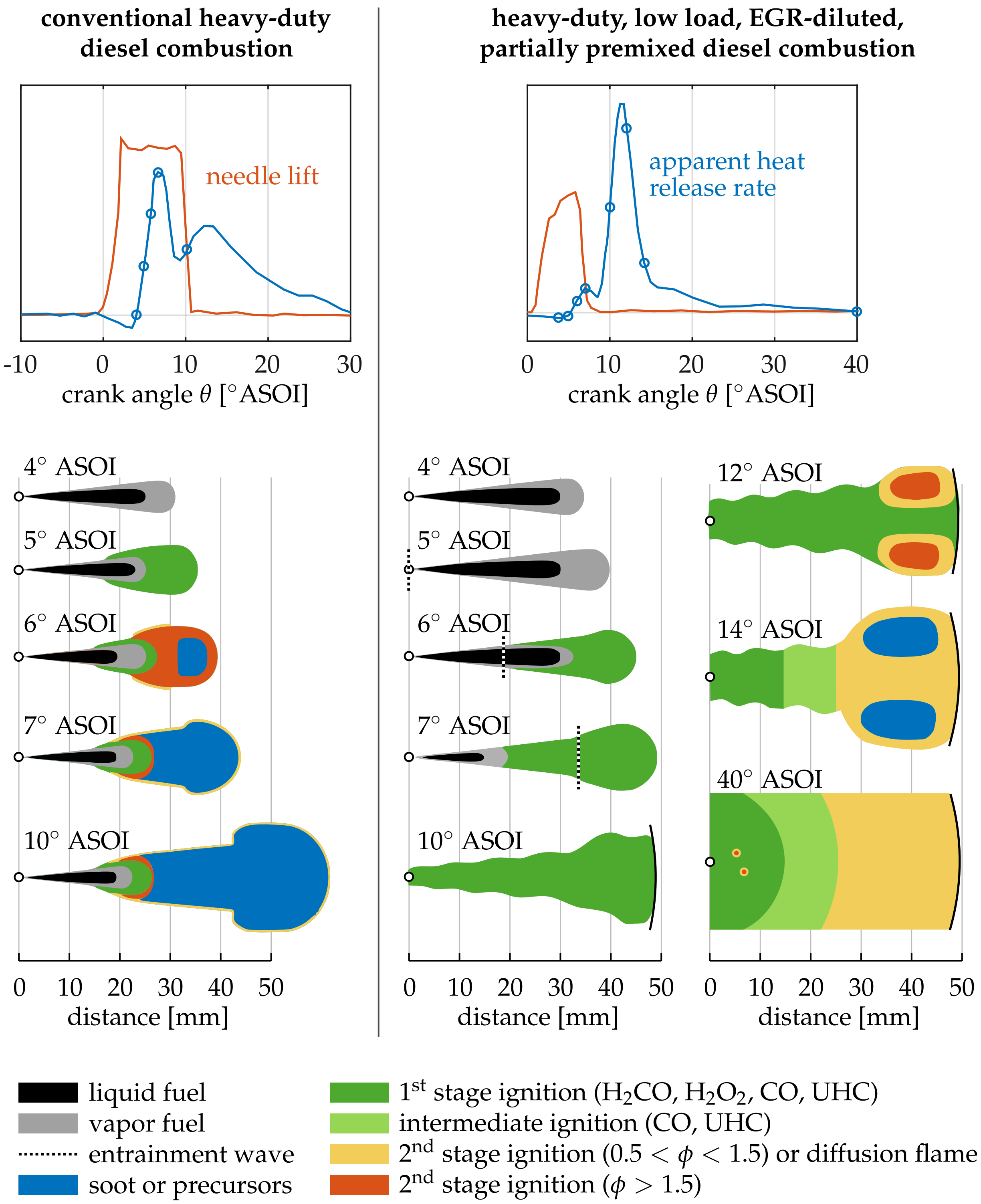

Figure 2.6: Phenomenological description of conventional heavy-duty diesel combustion (left) and of low-load, EGR-diluted, partially-premixed heavy-duty diesel combustion (right) at a speed of 1200 rpm ($1° = 125\mu s$); adapted from [18] and [69].

The liquid diesel fuel is injected into the combustion chamber at high pressures ($> 1000\,\mathrm{bar}$) through small nozzle holes ($100 - 500\mu$m) within only a few degrees of crank angle ($< 20°$). This results in a very fine spray that penetrates while forming a roughly conical jet. Entrainment correlations (like the one presented in Sec. 2.1.1) based on the momentum balance and supported by experimental data show that the equivalence ratio along the jet axis scales inversely with the downstream distance. The high temperature of the entrained ambient gas cause the liquid fuel droplets to evaporate until only gaseous fuel remains downstream of the liquid length. Fuel evaporation under diesel engine conditions is not limited by the spray breakup, but by the entrainment rate for providing the necessary enthalpy of vaporization to the fuel. Therefore, the liquid length can be directly calculated from the momentum correlation, being the downstream distance where the energy supplied by the entrained gas is sufficient to completely evaporate the diesel fuel. At 4°ASOI the constant liquid length of the non-reacting jet is established while further downstream a solely gaseous fuel jet expands into the combustion chamber and becomes leaner.

The temperature rise associated with ongoing dilution initiates the first stage of ignition within the gas phase (5°ASOI). This first stage is characterized by low chemiluminescence of certain intermediate species (e.g. formaldehyde) and accompanied by a very limited net heat release. When the temperature exceeds a certain threshold level, the intermediate species are rapidly decomposed within $100 - 200\mu$s in the second stage of ignition (6°ASOI). As a consequence, the observed heat release increases and forms a distinct peak. Due to the short ignition delay, only fuel-rich regions in a range of $\phi = 2 - 4$ are involved in second stage ignition, and therefore the reaction products from incomplete combustion are of intermediate temperature ($1500 - 2000\,\mathrm{K}$). Since these are the conditions that lead to soot formation, polyzyclic aromatic hydrocarbons (PAH) – being typical soot precursor species – appear subsequently across the whole jet cross-section (7°ASOI). As a consequence of thermal radiation and the entrainment of hot reaction products, the liquid length drops after ignition.

As soon as the rich premixed zones are burnt close to the peak of heat release ($6 - 7°$ASOI), a diffusion flame forms at the outer part of the jet shear layer. Since the stagnation point flow at the jet tip causes a tip vortex to develop, the diffusion flame is found to establish first in the shear layer behind the tip vortex where air entrainment is high. As a consequence of the high temperature in the near-stoichiometric region of the diffusion flame, this thin zone is the main source of NO. The flame does not extend all the way up to the nozzle hole, but stabilizes a certain distance downstream at the lift-off length. Upstream of the lift-off length, air is entrained all the way into the jet core, allowing a stationary, premixed reaction zone to be formed. Since again the fuel-air mixture in this premixed reaction zone is rich, soot is formed and forced towards the jet tip, where it adds up to the soot from the initial premixed combustion following self-ignition. The jet now enters a quasi-stationary phase ($7-10°$ASOI) in which the rate of mixing directly determines the fuel conversion rate and the jet structure does not change. Dec's description does not include information on the jet structure after the end of injection.

The flame lift-off is affected by various factors, starting from injection parameters (pressure, nozzle diameter) and including the conditions in the combustion chamber (temperature, density) as well as the fuel composition itself. Since the lift-off determines the quality of the mixture supplied to the standing reaction zone, it strongly influences soot formation. It is therefore not surprising that an increase in the lift-off length reduces soot formation. If the flame stabilizes downstream of the location where $\phi < 2$ at the center line, soot formation is inhibited at all [75, 93]. However, the flame is found well upstream of this location in conventional diesel engine operation.

2.2.2 Partially-Premixed Low-Temperature Diesel Combustion

Mixture formation after EOI is not considered in Dec's model for conventional diesel combustion, since it is only relevant for the burnout phase. But if partially-premixed combustion is to be realized by shifting the ignition beyond EOI, post-injection mixture formation strongly gains importance. For a theoretical investigation of the entrainment behavior after the injection is ended, a one-dimensional numerical jet model was introduced in [70]. It is based on an analytical entrainment correlation and uses empirical geometrical assumptions (i.e. the cone angle) to reliably predict the transient jet penetration and liquid length even with non-steady injection rates. The entrainment rate $\dot{m}_{\mathrm{ent}}$ – defined as the mass of surounding gas radially entering the diesel jet per downstream axial distance – is expected to increase when the injection rate is reduced, as observed in single-phase jets [7, 10–12, 109] (see also Sec. 2.1.3). Figure 2.7 shows the numerically determined entrainment rate for a top-hat-profile injection (infinitely fast ramp-up and ramp-down) relative to the entrainment rate of a stationary jet at different times after EOI.

The results show that the relative entrainment rate exceeds unity close to the injector orifice after EOI, indicating an improved mixture formation compared to the stationary jet. Based on experimental observations, the model assumes a constant jet cone angle even after EOI, causing an axial mass flux deficit when the fuel admission is terminated. Continuity requires the entrained gas mass flux to increase in order to compensate for the reduced nozzle flow. As a consequence of the momentum exchange between the entrained gas and the fuel, the axial velocity is further reduced and the entrainment is enhanced. This so-called entrainment wave propagates downstream while growing in axial extent and in intensity. If the top-hat profile in the numerical analysis is replaced by a more realistic, finite change in injection rate, the intensity of the entrainment wave is reduced along with the axial mass flux deficit.

After the entrainment wave has passed, the axial velocity is quickly reduced until the jet flow becomes stagnant. As a consequence, the entrainment rate in the wake of the entrainment wave falls below that of a steady jet. But since the fuel mass flux is quickly ramped down to zero at the same time, the local equivalence ratio nevertheless decreases. Therefore the net mixing rate, defined as the entrainment rate relative to the local fuel mass, remains higher than in the case of the steady-state jet after the passage of the entrainment wave. As a result, the axial fuel-air equivalence ratio distribution is rapidly inverted [71]. While the equivalence ratio is high close to the injector and scales inversely with the axial distance during injection, the mixture near the injector quickly becomes more fuel-lean than the downstream mixtures after EOI. This inversion of the mixture distribution before ignition is – along with the overall leaner mixture – one major difference between partially-premixed and conventional diesel combustion.

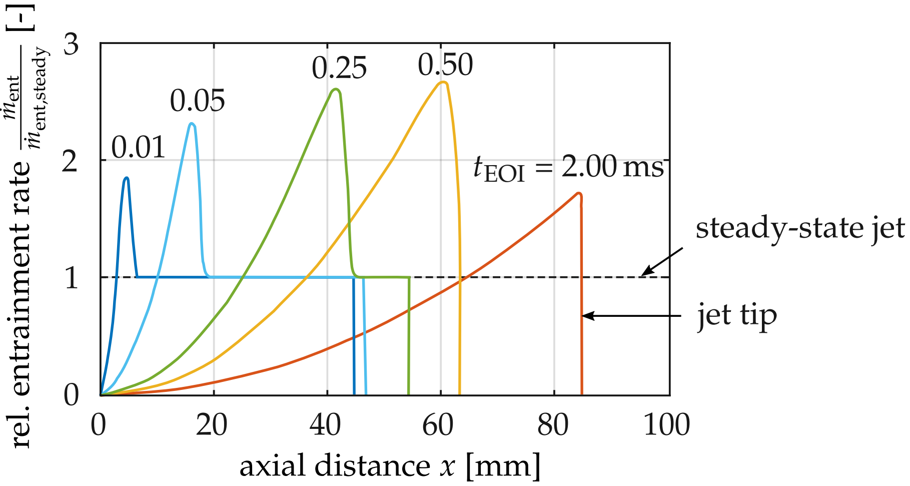

Figure 2.7: Evolution of the axial entrainment rate after EOI relative to a steady-state jet, adapted from [70]; injection at 1200 bar and 0.5 ms duration with top-hat rate profile at diesel-like ambient conditions (900 K, 19.3 kg/m^3).

As previously introduced, low-temperature combustion for limiting NO emissions is commonly realized by a reduction of the oxygen concentration with EGR. Even though this increases the ignition delay, additional measures like early or late injection timing or a reduction of the compression ratio (e.g. by Miller valve timing) are required to realize a positive mixture dwell for partially-premixed combustion. However, the ignition delay is kept sufficiently low to maintain a direct coupling with the injection event. At the time of ignition, the mixture distribution therefore still exhibits fuel-rich zones. The phenomenological description of partially-premixed LTC by Musculus *et al.* [69] is illustrated in Fig. 2.6 on the right hand side. It refers to single injection and is applicable only for reduced load due to the harsh combustion experienced with this operating strategy.

Initially and up to 4° ASOI, the jet structure is very similar to conventional diesel combustion. As a consequence of the reduced charge temperature and density, the jet penetrates faster and shows an increased liquid length. The injection duration is reduced with the load, and the injection rate peaks already at 5° ASOI just shortly after the maximum liquid length has established. As a consequence of the declining injection rate, an entrainment wave starts to form and propagates at about double the velocity of the jet tip. Depending on the duration of the mass flow ramp-down relative to the liquid length convection time, the liquid phase either retreats towards the orifice, lifts off or splits up.

The passage of the entrainment wave alters the structure of the mixture field, and thereby the ignition process as well. As a result of the rapid temperature increase with conventional diesel combustion, the first and second stage of ignition appear in quick succession and in different parts of the jet at the same time. Therefore, the two stages can not be identified from the heat release rate. Partially premixed LTC in contrast shows an isolated slight increase in heat release 7° ASOI, attributable to the first stage ignition. In accordance with kinetic simulations, formaldehyde (H_2CO) – an intermediate tracer species formed during first stage ignition and quickly consumed during second stage ignition – appears within wide regions of the downstream jet independent of stoichiometry.

The peak in heat release rate caused by second stage ignition is accompanied by the appearance of the hydroxyl radical (OH) at 12° ASOI in the downstream region of intermediate stoichiometry. It is possible to distinguish between second stage ignition of rich and intermediate stoichiometry since the rich zones do not accumulate significant OH while formaldehyde is consumed in any case. A little bit later in the cycle, soot and its precursors appear in the rich pockets that still remain near the tip vortex or where the neighboring jets interact after impingement at the piston bowl. As the cycle progresses, the jet contour becomes wavy and vanishes while the soot and its precursors in the rich pockets are oxidized.

The fuel-lean upstream regions do not have sufficient time to reach second stage ignition before the charge is cooled by expansion. Formaldehyde, UHC and CO are not oxidized and therefore the upstream region is responsible for the low combustion efficiency associated with partially-premixed LTC. Carbon monoxide concentrations are highest near the boundary to the regions that have reached second stage ignition (labelled intermediate ignition), since the CO formed in the fuel-rich mixtures is oxidized during late cycle mixing. Large droplets released from the injector holes may further contribute to the UHC and CO emissions.

2.3 Review of High-Pressure Dual-Fuel Combustion

One major prerequisite for the realization of HPDF combustion is the availability of a fuel injection system capable of injecting both fuels into the combustion chamber at high pressure and within short durations. Research on HPDF combustion was therefore essentially promoted when Hodgins *et al.* presented such an injector concept in 1992 [35]. Right from the start, the goal was to achieve combustion characteristics and efficiencies similar to conventional diesel combustion with natural gas as the primary energy source. This is realized by injecting the diesel pilot prior to the natural gas in order to cause a volumetrically distributed region of diesel combustion products for fast NG ignition followed by mainly mixture-limited combustion. The injection of natural gas after the pilot has already ignited is termed conventional HPDF, as it refers to conventional diesel combustion.

Hodgins *et al.* first demonstrated the desired combustion characteristics and high efficiencies along with a benefit in PM, NO_x and CO_2 emissions when compared to diesel combustion. This positive effect on the emissions was mainly assigned to the lower carbon content and the lower flame temperature of the NG fuel [36]. The injector concept was further improved by testing it on a two-stroke engine in the following years [20, 21, 31, 32]. In order to allow for modern emission mitigation strategies, MacTaggart-Cowan *et al.* applied HPDF to a four-stroke research engine with cooled EGR [60]. The close similarity to conventional diesel combustion was again demonstrated, since EGR caused a reduction in NO while it increased CO and UHC emissions [57]. Further investigations covered the influence of fuel composition by blending the natural gas with hydrogen, ethane, propane and nitrogen [63, 64]. While PM emissions increased as expected when the overall carbon content was raised with ethane or propane, they were virtually eliminated when hydrogen or nitrogen were added. Interestingly, CO and UHC were reduced by all of the additives. Another study investigated the influence of injection pressures up to 600 bar The higher pressures were found to allow reduced PM emissions and higher efficiencies if the nozzle diameter is adjusted accordingly [58, 61].

In contrast to diesel combustion, the degree of premixing is determined not solely by the kinetics of auto-ignition but most importantly by the relative timing of the two injections. The combustion characteristics fundamentally change when switching to partially-premixed HPDF by simply starting the natural gas injection prior to pilot fuel ignition. This is assumed to be caused by a shift in combustion regime from mixing-limited reaction to flame propagation, since high EGR rates do not increase PM with partial premixing [62]. However, premixing causes an increase in unburned CH_4 emissions. Faghani *et al.* [22] attributed this effect to over-mixing of some lean regions and managed to maintain the engine-out CH_4 by slightly elevating the global equivalence ratio. In the same work the authors motivate the formulation of a phenomenological description for HPDF, since they observed a direct dependence of some combustion metrics on the relative injection timing.

These investigations cover the effect of various parameters on HPDF combustion and allow to assess the consequences and potential of different design choices. However, this was mainly achieved by analyzing engine performance and emissions following parametric variations rather than by direct observations. Only very recently, Rochussen *et al.* [87] made an attempt to formulate a phenomenological description of HPDF by presenting OH* and natural flame luminosity imaging data. They were able to identify the different combustion phases and described how the combustion regime changes from conventional to partially-premixed HPDF. An in-depth analysis of local phenomena was not possible since the flame luminescence could not be linked to the flow field of the two interacting jets. Furthermore, some important parameters could not be studied independently, like jet arrangement and operating conditions.

Only little is known about the spatial and temporal interaction between the jets, and how this interaction determines the local combustion progress and pollutant formation. An early injector design featured two randomly rotating concentric needles and thereby allowed for variable interaction between the fuel jets [21]. The results suggest a considerable influence of the jet interaction on the overall combustion process, since an unequal number of jets for the two fuels resulted in a lower variance of heat release. Numerical analysis supports this interpretation [52]. Furthermore, the interaction is assumed to directly influence pollutant formation. Apart from a direct correlation of PM emissions and the pilot quantity [59, 62], a strong effect of the diesel pilot on soot formation in the natural gas jet is reported as well [39]. The authors were able to assign the engine-out particles to the two fuel sources by an elaborate experimental approach. They used biologically generated diesel fuel and fossil-sourced natural gas, and then traced back the origin of the carbon in the particles based on the isotope composition.

3 Experimental Setup

All investigations presented in this thesis are carried out on a rapid compression-expansion machine (RCEM) equipped for high-pressure dual-fuel combustion analysis. The components of the experimental setup are shown in Fig. 3.1 and will be described in detail in this chapter. Firstly, the operating principle and testing sequence of the RCEM are explained. Special attention is given to the flexible fuel injection system in the second section. Then, the optical setup for simultaneous shadowgraph (SG) and OH^* high-speed imaging is introduced. The control and data acquisition system records not only the measurement signals from the sensors, but is also used for synchronization and triggering during the single-shot experiments.

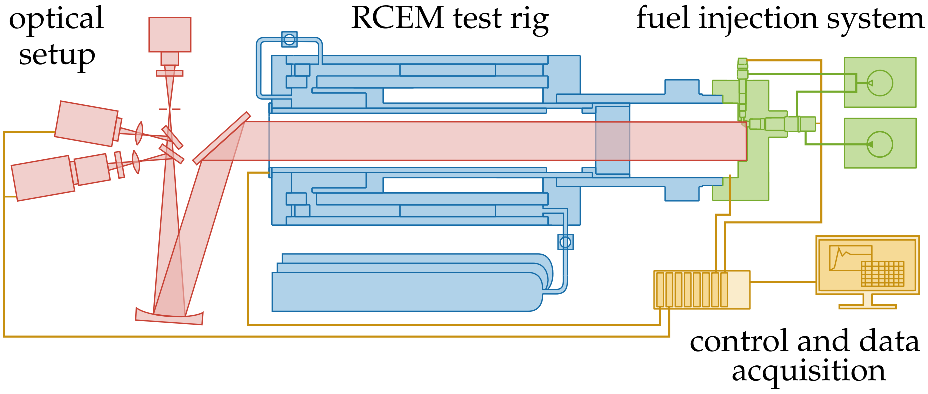

Figure 3.1: Components of the experimental setup.

3.1 Rapid Compression-Expansion Machine

The pneumatically driven single-shot RCEM was originally developed by Prechtl [79] and Dorer [19] for the investigation of compression ignition with hydrogen direct-injection. Later, it has been used to study diesel injection at very high pressures [80] and prechamber-ignited natural gas combustion [66]. The large bore (220 mm) allows for a fundamental analysis of the processes during injection, ignition and combustion since the free penetration length before wall impingement an be maximized. Due to the variable stroke (up to 380 mm) the achievable compression ratios are high and mainly limited by the maximum chamber pressure (200 bar) and the chamber volume design at TDC.

Figure 3.2 shows a schematic of the RCEM. It features two concentrically arranged ring-shaped pistons ③ and ⑦, coupled by hydraulic oil ④. The opposed motion of the driving and working pistons suppresses net inertial forces during acceleration, minimizing vibrations that could harm the quality of the optical measurements. At the start of the experiment the working piston rests in its leftmost position, covering the flow orifice ⑤ and preventing oil flow between the two chambers. Therefore, the pistons remain in their starting position when the system is pressurized by opening the valves ② to the driving air supply ①. Actuation of the bypass valve ⑥ initiates piston motion by connecting the two oil chambers. After the flow orifice is uncovered, the working piston rapidly accelerates. Compression stops at top dead center (TDC) when the forces by the driving

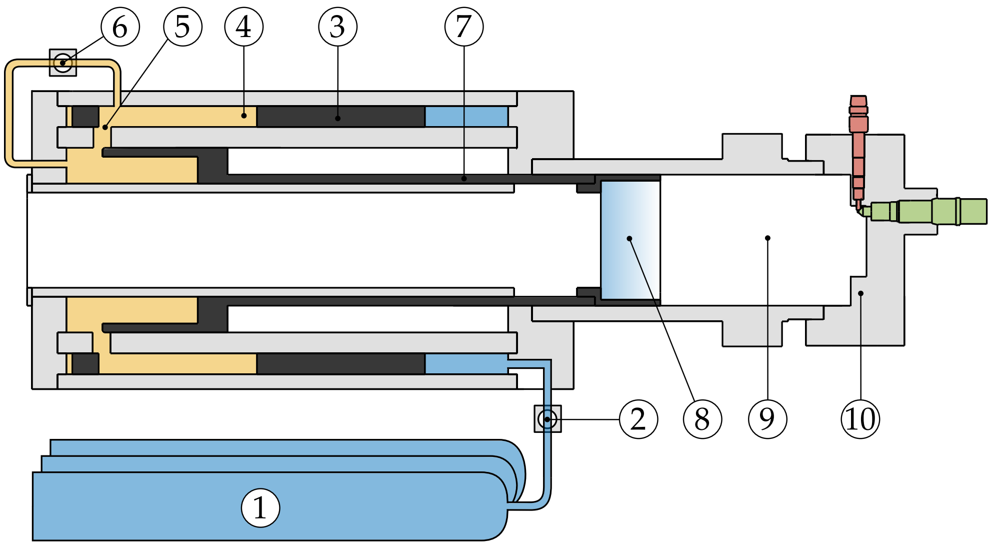

Figure 3.2: Schematic of the RCEM test rig: ① driving air supply, ② supply valve, ③ driving piston, ④ hydraulic oil, ⑤ adjustable orifice, ⑥ bypass valve, ⑦ working piston, ⑧ quartz glass window, ⑨ combustion chamber, ⑩ cylinder head.

pressure, inertia and friction balance the force imposed by the pressure in the combustion chamber. As this is a dynamic equilibrium, it is followed by an expansion. The crank motion of an engine closely matches the piston motion near TDC, where injection and combustion are initiated. Optical investigations of the processes in the combustion chamber ⑨ are made possible by the large quartz glass window ⑧.

Due to the lack of a direct mechanical constraint, the compression ratio can be varied in a wide range by tuning the driving air pressure. Since the RCEM shows significant heat losses especially in the crevice volumes, it is reasonable to define the effective compression ratio ϵ_{eff} for a volume element in the adiabatic core of the combustion chamber via the pressure ratio

$$\epsilon_{\text{eff}} = \frac{v_0}{v} = \left(\frac{p}{p_0}\right)^{1/\kappa(T)}. \tag{3.1}$$

Most of the volume in the combustion chamber can be assumed to follow this adiabatic compression, since no charge motion is applied and the boundary layer is very thin. The temperature in this central part of the combustion chamber can be determined at any time directly from the pressure measurement if the temperature at the start of compression T_0 is known:

$$T = T_0 \cdot \epsilon_{\text{eff}}{}^{\kappa(T)-1}. \tag{3.2}$$

T_0 is measured with a thermocouple. Since the walls are not heated and the test repetition rate is low, T_0 was found to remain constant within a small range of 296±1.5K. Temperature and pressure at TDC can be set independently by adjusting the starting pressure p_0 and the compression ratio ϵ_{eff}. Even though this approach gives full control over the thermodynamic state near TDC, the air mass and therefore the global air-fuel ratio cannot be held constant for different operating conditions. As long as the local interaction between two single fuel jets is investigated, the global air mass has no direct impact on the results. However, the influence of the global air mass can not be neglected in general if conditions with strong premixing are investigated. This is discussed in more detail in Ch. 7 of this work.

3.2 Cylinder Head and Fuel Injection System

For an injection system capable of injecting two fuels separately and directly into the combustion chamber at high pressure, different configurations are conceivable in principle. Depending on the final implementation – e.g. axis-symmetric needle-in-needle concept (e.g. [35]), asymmetric twin-needle injector or symmetrical multi-needle system – a wide variety of geometric interactions between gas and pilot jet can occur. Hence, a flexible adjustment of the jet arrangement is necessary for fundamental investigations and therefore a separate injector is used for each fuel. These injectors are equipped with only one nozzle bore each and the plane of interaction is chosen perpendicular to the piston axis.

In contrast to a full-scale four stroke engine, the RCEM cylinder head can be designed without large valves covering most of the cylinder head surface. Even though this leaves more space for the injector arrangement, a flexible adjustment of the jet interaction is difficult to realize geometrically. As shown in Figure 3.3, the diesel injector ⑦ is therefore installed at a fixed position laterally through the liner wall and its nozzle bore is aligned with the injector axis. As this restricts the maximum stroke and therefore the compression ratio, an exchangeable radial volume reduction ④ is employed. Similar to a conventional piston bowl, the combustion chamber becomes more compact at the cost of a reduced free jet penetration length. An advantage of this arrangement is that the variable clearance resulting from the different compression ratios at different operating conditions does not alter the jet impingement at the chamber walls.

The natural gas injector ⑧ is placed separately in a flexible mount within the cylinder head. This mount consists of an outer ① and an inner eccentric part ②. Since the eccentricity of the inner part with respect to the outer part and the eccentricity of the gas injector within the inner part are both 24 mm, the gas injector can be freely shifted within a circular region of 48 mm diameter by simply rotating the two parts of the mount. The offset of the gas jet origin with respect to the diesel jet is characterized by the downstream shift x and the lateral shift y. As all the investigations presented in this work assume a single integrated dual-fuel injector, the offset between the injectors was minimized and fixed at $x = 8\,\text{mm}$ and

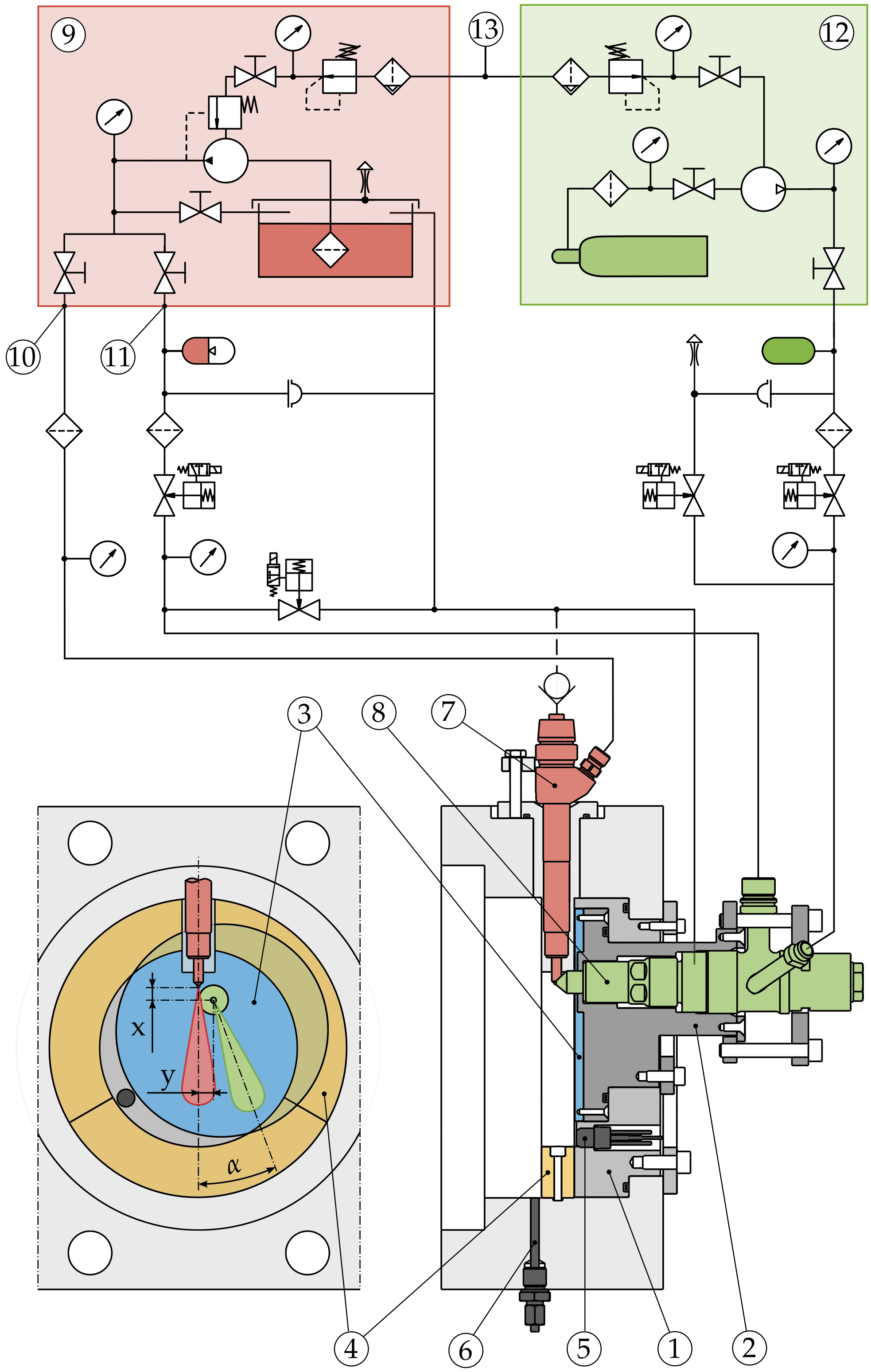

Figure 3.3: Injector arrangement and fuel supply: ① outer mount, ② inner eccentric mount, ③ surface mirror, ④ volume reduction, ⑤ pressure transducer, ⑥ thermocouple, ⑦ diesel pilot injector, ⑧ natural gas injector, ⑨ diesel pump, ⑩ pilot diesel supply, ⑪ actuation diesel supply, ⑫ natural gas compressor, compressed air supply ⑬.

$y = 5\,\text{mm}$. In contrast to the diesel injector, the natural gas injector is equipped with a nozzle bore perpendicular to the injector axis. Therefore, the angle α between the two jets can be adjusted by simply rotating the gas injector.

For the double-pass shadowgraph system described in the next section, the surface of the inner mount is covered by a surface mirror ③ made from polished stainless steel. Furthermore, a piezo-electric pressure transducer (⑤; Kistler 7061C) is installed in the cylinder head for dynamic recording of the chamber pressure and a thermocouple (⑥; Type K) is added for monitoring the chamber temperature at the start of compression.

Fuel is supplied to the injectors by a diesel pump ⑨ and a natural gas compressor ⑫. These units each include a pressure booster fed with compressed air ⑬ and allow diesel injection at up to 2200 bar and gas injection pressures as high as 600 bar. Since the gas injector is actuated hydraulically by the diesel fuel, the diesel pump is equipped with two separate outlet ports for the pilot ⑩ and actuation diesel supply ⑪.

All fuel supply lines include filters (5 micron) and pressure transducers. While the diesel pilot injector is directly connected to the pump outlet port, both the actuation diesel and gas supply line are additionally equipped with pneumatically actuated pressurization and relief valves. These valves allow for automated pressurization schemes during the experiment, since the gas pressure must not be lower than the actuation fluid pressure at any time. To protect the gas injector and other components from overpressure, its two fuel lines are equipped with burst discs. In general, different pressure levels are required at the two diesel pump ports. In order to provide these two levels with only one pump, a bladder accumulator is included in the actuation diesel supply line. The accumulator is pressurized, then cut from the diesel pump and provides the actuation fluid supply to the gas injector during the test run. The gas line is also equipped with an accumulator that reduces pressure fluctuations in the system.

The standard fuel injection parameters are listed in Tab. 3.1. If values other than the standard ones are used as well, they are stated in brackets along with the corresponding section. Since not only the injected fuel mass, but

Table 3.1: Standard fuel injection parameters and values used for parameter variations (stated in brackets).

parameter	diesel pilot injection	natural gas injection
nozzle bore diameter d	0.1 mm	0.9 mm (0.7 mm/1.1 mm)[1]
fuel mass m_{fuel}	3 mg (1.5 mg)[2]	80 mg (56 mg/40 mg)[3]
injection pressure p_{inj}	2000 bar (1000 bar)[2]	330 bar (490 bar/235 bar)[1]
injection duration t_{inj}	0.85 ms	2.7 ms (2.0 ms/1.55 ms)[3]

[1] natural gas injection pressure variation in Sec. 6.2.2.
[2] micro-pilot ignition without natural gas in Sec. 5.1.
[3] load variation by reduced NG injection duration in Sec. 7.2.4.

also the injection rates are required for accurate injection timing, both injectors were calibrated. A commercial IAV Injection Analyzer was used to quantify the pilot injection. Natural gas injection was analyzed with a newly developed rate meter capable of handling compressible fuel [88]. A set of different injection pressures and injection durations was tested with 100 consecutive injections each. This allowed the calculation of average injection rate curves and the determination of the minimum amount of fuel that can be injected while still maintaining a low variance.

The measured injection rate curves were then approximated and parametrized to allow for an interpolation between the tested combinations of injection pressure and duration. This was done by conservation of the injected fuel mass and determination of SOI and EOI using threshold values. Due to the slower opening ramp of the natural gas injector, the end of this ramp is additionally determined using a trapezoidal approximation. For any combination in between the tested ones, these characteristic times and the injected mass can be interpolated and used to reconstruct an approximated mass flow curve. Figure 3.4 shows the good agreement between the parametrized and the actual injection rates for NG and diesel injection.

Initially, the threshold value for identification of natural gas SOI from the injection rate measurements was set very low. The hydraulic delay was then used to calculate injector trigger timings for the RCEM experiments. Later optical verification of jet penetration for validation of the CFD

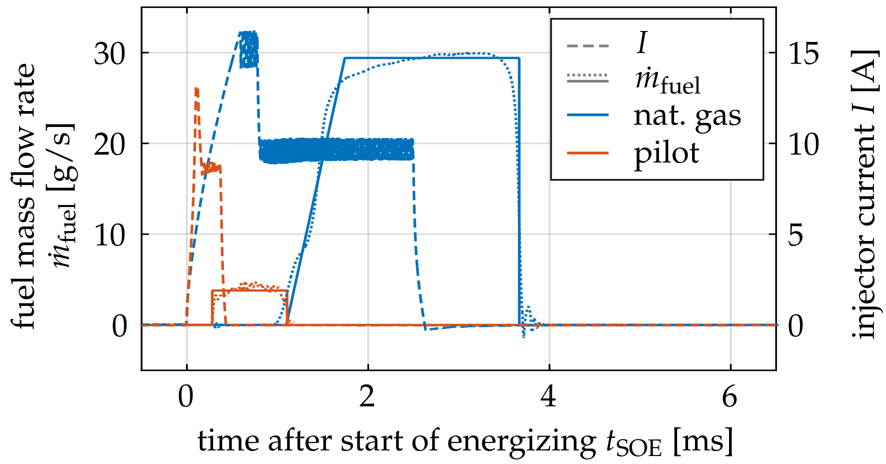

Figure 3.4: Injector current (dashed), measured fuel injection rate (dotted) and parametrized approximation (solid) for pilot and natural gas injection.

model showed that natural gas exits the injector about 0.12 ms later than determined from the injection rate measurement. The threshold value was therefore increased and the corrected SOI used for the approximated injection rates and the numerical analysis. However, the initial value for natural gas SOI still persists in the experimental data and causes a slight error in relative timing Δt_{SOI} between the two injections (for definition see Sec. 4.1.4). The effect of this error is low and has no impact on the results presented in this work.

3.3 Optical Measurement Setup

The optical setup combines a shadowgraph and an OH^* imaging system via only one optical access for simultaneous recording. These two techniques were selected as they complement each other very well. While shadowgraphy is well suited for visualizing flows involving density gradients or even different phases, flame propagation can be observed by recording the chemiluminescence of the OH^* radical formed during oxidation of hydrocarbons. Since the shadowgraph system records the broadband visible light spectrum, it detects regions with sooting combustion as well while soot radiation is blocked from the OH^* camera by a narrow UV bandpass filter. Figure 3.5 displays the general configuration of the optical system at the RCEM. Hereafter, the two measurement

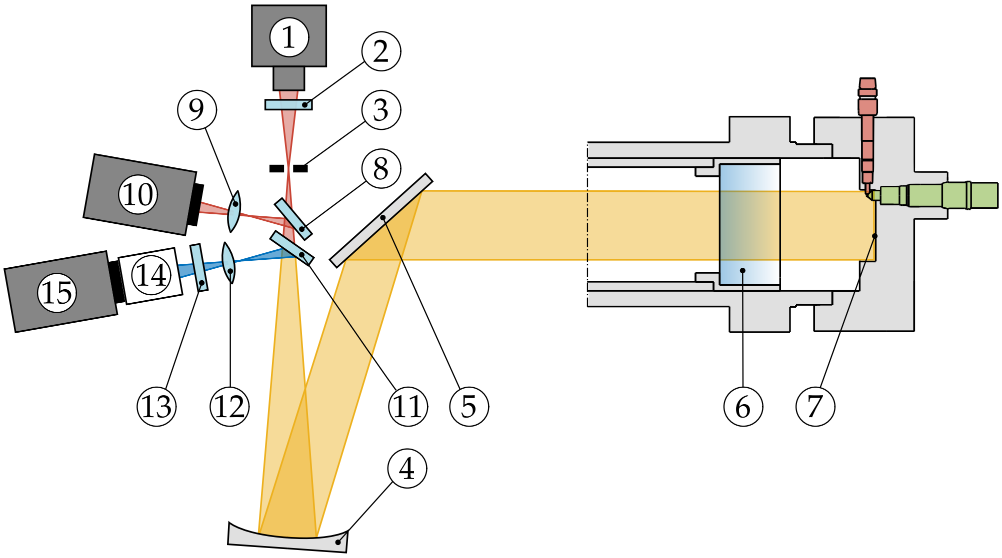

Figure 3.5: Optical setup for simultaneous SG and OH* imaging: ① Xe arc lamp, ② UV filter, ③ pinhole, (④ parabolic mirror, ⑤ planar mirror, ⑥ quartz glass piston, ⑦ surface mirror, ⑧ 50/50 beam splitter, ⑨ achromatic focusing lens, ⑩ SG camera, ⑪ UV beam splitter, ⑫ UV focusing lens, ⑬ OH* filter, ⑭ image intensifier, ⑮ OH* camera.

techniques are described individually, and Fig. 3.5 is referred to for the explanation of the specific implementation.

3.3.1 Shadowgraph Imaging

The shadowgraph and schlieren measurement techniques are very similar and often mixed up. They are both introduced here in order to outline why shadowgraphy is used. The underlying measurement principle was first described by Toepler [100]. It is based on the deflection of a light beam when passing through a transverse density gradient. Figure 3.6 shows a simplified representation of the measurement setup of the two methods. Since both techniques are widely used and can be regarded as standard, they are only briefly discussed here and the reader is referred to other sources for in-depth information, e.g. [92].

The light from a source is parallelized by guiding it through a pinhole placed at the focus of the collimating lens. Spatial density gradients within the measurement volume lead to a deflection due to the associated gradient

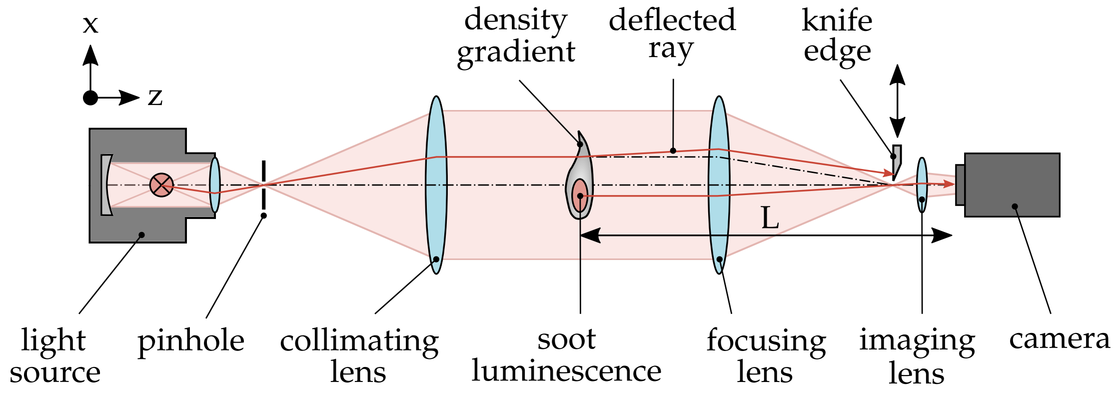

Figure 3.6: Schematic principle of schlieren (with knife edge) and shadowgraph (without knife edge) imaging.

in refractive index. When focusing the image onto a camera, these regions of non-uniform density gradients show a reduced intensity with respect to the background illumination. While the deflected rays are blocked by a knife edge in a schlieren arrangement, removing the knife edge for shadowgraph imaging leads to increased intensity close to the density gradient. This results in schlieren representing the first spatial derivative of the refractive index integrated along the line of sight, while shadowgraphy visualizes the second derivative.

With shadowgraphy the sensitivity depends on the angular deflection δ, proportional to the density gradient normal to the light rays according to the relation

$$\delta_x \propto \int \frac{1}{n} \frac{\partial n}{\partial x} dz, \tag{3.3}$$

for a gradient in x-direction. The sensitivity of the schlieren system additionally depends on the position of the knife edge and the beam displacement Δx. This displacement is proportional to the distance between the schlieren object and the imaging plane L according to

$$\Delta x \propto L \int \frac{1}{n} \frac{\partial n}{\partial x} dz. \tag{3.4}$$

Due to the optical constraints of the RCEM and the required focal length of the collimating element, the distance L becomes very long (> 7m). Along with the very strong density gradient between the directly injected cold fluid and the hot charge gas a schlieren knife edge would render most of the regions dark. Therefore a shadowgraph setup is used, which allows to investigate a wide range of density gradients. The gradient between the charge gas and the liquid phase of the injected diesel droplets is large enough to block the light completely.

Any volumetric emission of light in the observed region adds up to the light source illumination and is represented as a bright area within the image. While the intensity of light emitted by radical species in the flame is low compared to the illumination intensity, broadband black-body radiation from hot soot particles is strong enough to be detected by the shadowgraph camera.

The implemented shadowgraph setup shown in Fig. 3.5 differs from the principle sketch in Fig. 3.6. By replacing the collimating and focusing lenses with a single parabolic mirror ④ slightly tilted from the optical axis, a large observation area is realized. Furthermore, chromatic aberrations that could harm the optical quality with the broadband illumination from the xenon arc lamp ① are avoided this way. Since the RCEM has only one optical access, a surface mirror at the cylinder head ⑦ is used to redirect the incoming light back the same way. The measurement volume is thus illuminated twice, which leads to a double image of the density gradients. However, this effect can be neglected since the distance between the object and the surface mirror is very small. To separate the reflected beam from the incoming beam, a 50/50 beam splitter ⑧ is used. This reduces the intensity of the incident beam before it is directed through the measurement volume, causing only 25 percent of the lamp's intensity to be exploited. However, the light source is bright enough to realize the short exposure time required for sharp images.

3.3.2 OH* Chemiluminescence Imaging

The light emitted by hydrocarbon flames can be attributed to two different phenomena that contribute to the overall wavelength spectrum, as shown in Fig. 3.7. On the one hand, solid soot particles – as they are formed especially in oxygen-deficient combustion – emit a broadband black-body radiation with a temperature-dependent maximum in the infrared range. On the other hand, the spontaneous transition of electrochemically

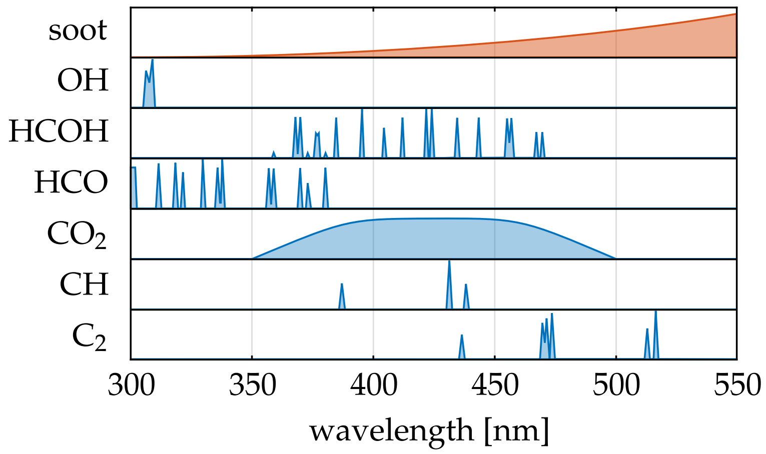

Figure 3.7: Specific emission bands from soot luminescence (red) and from electrochemically excited reaction species (blue), adapted from [27].

excited species (denoted with an asterisk) back to ground state results in distinct emission bands, which are presented in blue color for the most important species in hydrocarbon flames. Chemiluminescence from the excited hydroxyl radical (OH^*) is particularly suitable for localizing the flame front. OH is a key molecule in the oxidation process, formed and consumed directly in the primary reaction zone [45]. Its excited state has a short lifetime of only about 700ns before transition to ground state [8]. Furthermore, it exhibits the strongest emission bands in the ultraviolet (UV) range, which allows to minimize the contribution of broadband emitting molecules (e.g. CO_2) and strong soot radiation to the measurement signal by means of narrow-band filtering.

The physical principle of OH* chemiluminescence is only briefly outlined here based on [23, 27, 53]: The left chart in Fig. 3.8 shows the energy potential of the OH molecule, determined by the electron configuration at the ground state $X^2\Pi$ and at the excited state $A^2\Sigma^+$. Within an electronic state, the nucleus can occupy various discrete vibratory states ν. This corresponds to an oscillation in the internuclear distance within the horizontal line of a state ν for a bi-atomic molecule like OH. Depending on the cause of the electronic excitation, a distinction is made between photoluminescence (absorption of a photon), chemiluminescence (energy from chemical reaction) and thermal excitation (energy from collision). For OH molecules formed during the combustion process, chemical excitation dominates over thermal excitation below 2700K [24].

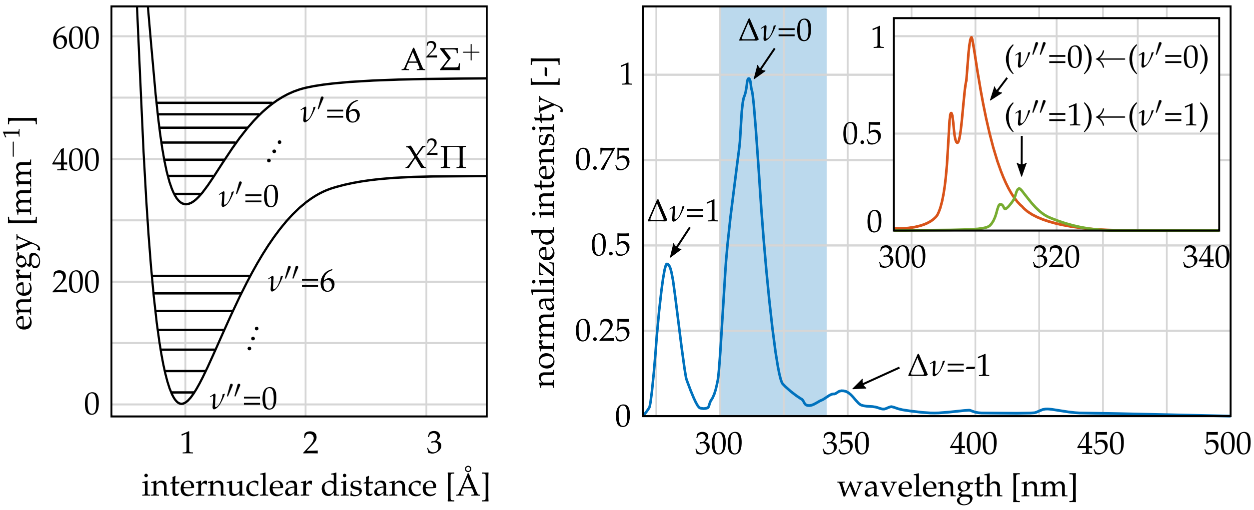

Figure 3.8: Left: OH energy potential at electronic ground state ($X^2\Pi$) and excited state ($A^2\Sigma^+$) [53]; Right: spectral intensity of the OH* chemiluminescence at 2200K, attributable to different changes in vibrational state [48].

The OH* emission spectrum presented in Fig. 3.8 on the right is dominated by transitions with $-1<\Delta\nu<1$ since states above ν=1 are very unlikely to occur at the prevailing temperatures [48]. The lines in the spectrum are additionally broadened by the rotational states superimposed to the vibratory energy level. Transitions with $\Delta\nu$=0 are most likely to occur and hence form the strongest emission band. Therefore, the corresponding frequency range – stretching from approximately 300nm to 320nm – is usually chosen for OH* chemiluminescence imaging.

If the OH* chemiluminescence is to be recorded simultaneously with SG imaging via the single optical access at the RCEM, flame radiation has to follow the same optical path. Hence, the two mirrors ④ and ⑤ in Fig. 3.5 are coated for high reflectance in the UV range. A bandpass mirror reflecting light between 270 − 370nm acts as UV beam splitter ⑪ that extracts the ultraviolet flame luminescence from the joint optical path. The isolated UV-light is then filtered near the maximum of the OH* emission spectrum within a narrow band of 307±10nm ⑬. In order to avoid any UV radiation emitted by the xenon arc lamp from interfering with the OH* measurement signal, it is removed by a UV longpass filter ② directly at the lamp output.

3.4 Controls and Data Acquisition

The controls and data acquisition are based on a CompactRIO™ system from National Instruments, which features a time-deterministic processor and a field-programmable gate array (FPGA). Thus not only demanding measurement and monitoring tasks can be accomplished, but also complex and fast calculation and control operations may be executed directly during the experiment. One advantage of the system is the availability of a large number of individualized I/O cards. In particular, a special module is available that provides the fast current and voltage profiles required for directly driving the solenoid valves in the injectors (NI 9751).

Table 3.2 provides an overview of the recorded signals along with the sensors and acquisition module details. The analog voltage signals from chamber pressure, needle lift and injector current are digitized with 16 bit resolution for accurate sampling. Chamber temperature and fuel supply pressure measurements are less demanding and only resolved with 12 bit. In order to capture the fast piston speeds with the high resolution of the incremental encoder, a digital input module with high sampling rate is used. The counter logic is implemented on the FPGA, so that the piston position is known at any time for triggering various events. The same digital input module records the camera trigger signals.

Figure 3.9 shows an example of the recorded pressure and piston position for a single unfired test sequence. As already described in section 3.1, compression is followed by expansion since the pistons pass beyond the position of static force equilibrium during compression. The resulting oscillatory motion is attenuated until equilibrium is reached. Only a limited region close to TDC of the first compression spike is of interest, where the pressure and position curves closely match the ones generated by an engine crank drive.

In engine applications, the injector actuation relative to the piston stroke is triggered via the crank angle. Since the RCEM does not have a crank drive, the piston position is measured directly using an inductive linear incremental encoder. This signal is not well suited for triggering events close to TDC, since the slow piston velocity as well as a slight deviation in maximum position from experiment to experiment would

Table 3.2: Overview of recorded signals, applied sensors, acquisition rate and resolution.

signal	**sensor**			**acquisition**		
	type	max.	accuracy	module	rate	resolution
chamber pressure	Kistler 6061B (incl. 5018A)	250 bar	<0.05 bar	NI9215	10µs	10 V/16 bit
needle lift	Micro Epsilon ES04/180	0.4 mm	<0.02µm	NI9215	10µs	10 V/16 bit
injector current	Pico TA009	60 A 20 kHz	<0.1 mA	NI9215	10µs	10 V/16 bit
chamber start temperature*	Thermocouple Type K	200 K	<1 K	NI9201	10µs	10 V/12 bit
fuel supply pressures	ADZ Nagano SML600	600 bar	<0.3 bar	NI9201	10µs	10 V/12 bit
piston stroke	Incremental Encoder	10 m/s	0.05 mm	NI9401	100 ns	5 V/TTL
camera I/O				NI9401	100 ns	5 V/TTL

*The fast change in chamber temperature during the experiment cannot be resolved with a thermocouple. Nevertheless temperature is recorded using the available fast module NI9201.

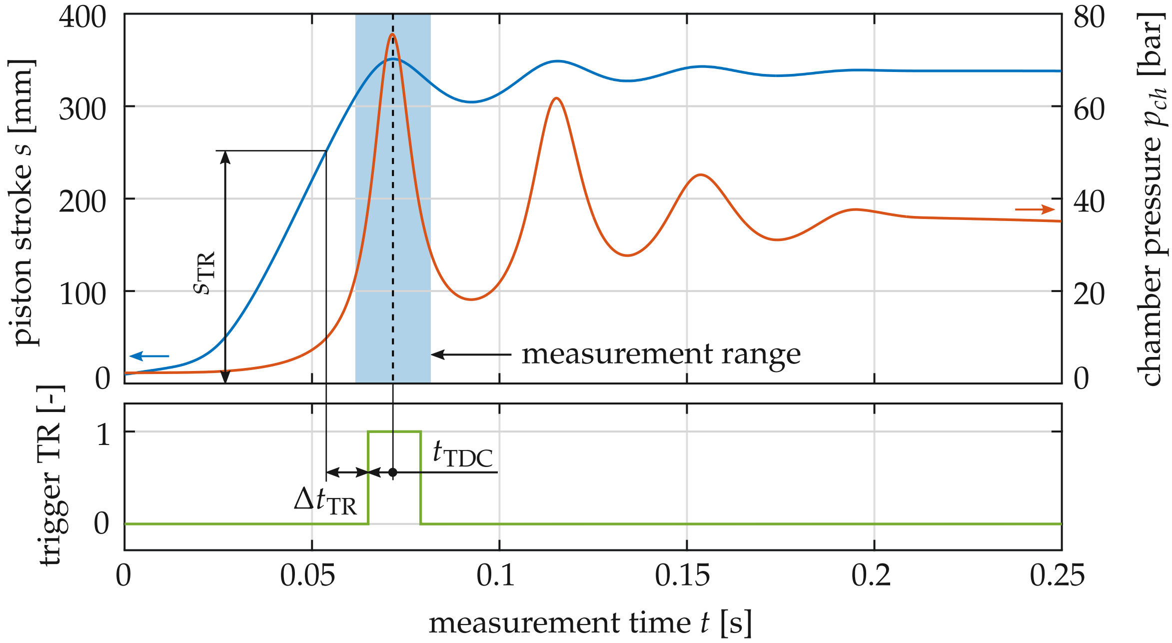

Figure 3.9: Unfired test sequence showing the measurement range during the first compression/expansion cycle and the trigger signal generation scheme.

lead to inaccurate trigger timing. Also, direct time-delayed actuation is not advisable because the piston moves relatively slowly at the start of compression. The reproducibility of this slow initial motion is not sufficiently high for accurate triggering during the fast compression and expansion. The camera acquisition trigger signal as well as those for actuating the injectors are therefore generated using a combined position and delay criterion, as shown in Fig. 3.9. As soon as the piston reaches a certain stroke position s_{TR} in the late region of fast compression between 250mm and 300mm, a counter starts and the trigger is further delayed by Δt_{TR}. The time it takes for the piston to move from s_{TR} to TDC at a certain compression ratio must be determined for calibration of the timing t_{TDC} relative to TDC.

Figure 3.10 shows the synchronization scheme of SG and OH* camera exposure along with the triggering procedure at 40kFps. While the low intensity of the OH* signal requires long exposure times of 23µs, sharp SG images can be achieved by a short shutter time of only 1.25µs. The exposure timings of both cameras are centered relative to each other using the camera's internal synchronization, which is also used to synchronize the image intensifier gating to the OH* camera exposure. The record signals from both cameras need to be detected along with the exposure signals for an exact temporal allocation of the images, since the acquisition is delayed relative to the camera trigger by about 100µs. As this delay is not strictly constant, an offset between the first OH* and SG image can occur as shown in Fig. 3.10. The exact synchronization is reconstructed from these camera signals in the data evaluation procedure.

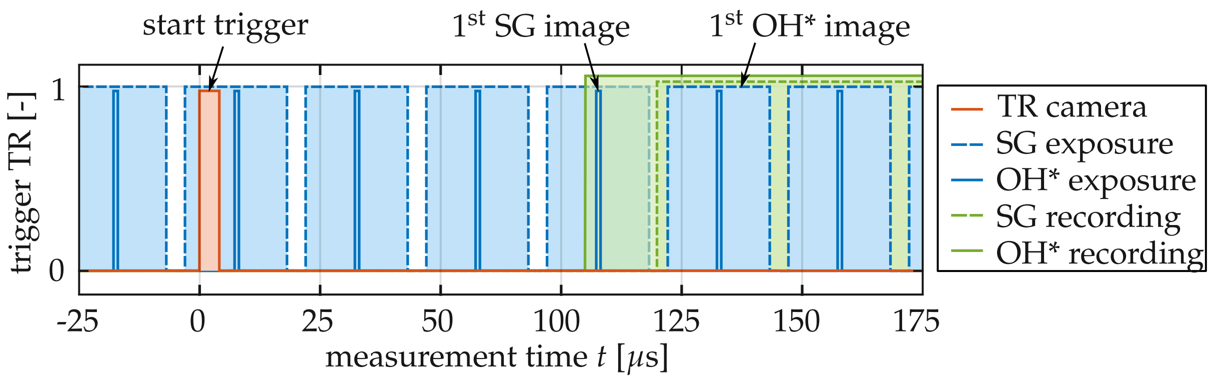

Figure 3.10: Camera triggers, record and exposure signals of the simultaneous SG/OH* imaging system at 40kFps.

4 Methods

This chapter describes the data evaluation and analysis methods for the assessment of injection, ignition, combustion and pollutant formation. Along with the methods as such, specific quantities and means of graphical representation are introduced and the physical interpretation of the results is discussed.

In the first section, a thermodynamic multi-zone model of the combustion chamber is introduced. It was developed to capture the specific conditions present within the RCEM and serves to calculate the heat release rate from pressure and piston position measurements. Then, the image processing technique is described along with an explanation of how to interpret the superimposed image data. Since the simultaneous progress of mixture formation and reaction is difficult to observe experimentally, numerical simulations are used to supplement the experiments. The applied RANS-CFD model employs detailed chemistry calculations and is only briefly introduced since its development and validation is not part of the present work.

4.1 Thermodynamic Model

Thermodynamic models of the combustion chamber are frequently used in combustion diagnostics to calculate the enthalpy released by reaction from the measurement of chamber pressure and piston position (i.e. chamber volume). In its simplest form, such a model consists of a single homogeneous volume for which the conservation equations are solved for the heat release required to meet the recorded pressure. More accurate models include multiple zones for a better representation of mixture and temperature inhomogeneities in the combustion chamber, e.g. an additional zone for the hot combustion products or a fuel-air mixture zone to represent direct-injection. However, each additional zone requires the specification of another boundary condition or model assumption to solve the growing system of equations.

This section describes the multi-zone model developed to reflect the specific conditions present with fuel direct-injection into the combustion chamber of the RCEM. The accurate representation of heat losses at the cold walls is particularly important, since they have the same order of magnitude as the small amount of energy released by the single pair of fuel jets.

4.1.1 Multi-Zone Model Approach

Figure 4.1 shows a schematic of the multi-zone model. An analysis of the heat losses at the RCEM has shown that they are mainly caused by the cold crevices (C) [25]. The basis of this analysis, the heat loss model and its validity are discussed in detail in section 4.1.2. Since the RCEM does not exhibit any charge motion, the mixing zone (M) and burnt zone (B) are embedded in an adiabatic core zone (I) that follows isentropic compression. During injection, the fuel is mixed with air in the mixing zone, and mass from this mixing zone is transferred to the burnt zone as combustion progresses. This part of the model is described in section 4.1.3. In order to preserve the isentropic zone even when cold flow is discharged from the crevices during expansion, an additional zone (G) is introduced in the gap between piston and cylinder head. Mass exchange between I and G is suppressed.

Each of the zones and their mutual interaction are described by a set of conservation equations. Since in the present context only temporal derivatives are dealt with, a reduced notation is chosen. Neglecting potential and kinetic energy terms, the change in internal energy dU for each zone can be formulated according to the first law of thermodynamics as

$$dU = \sum_i dH_i + \sum_j dQ_j - p \cdot dV, \tag{4.1}$$

where $p{\cdot}dV$ is the pressure-volume work performed by the zone and dQ_j any heat added to or removed from the zone by e.g. heat losses. If mass is exchanged across the system boundaries, this is reflected by a change in enthalpy dH_i. In this case, the zone becomes an open system and the partial derivative for the internal energy has to be considered:

$$dU = d(mu) = m{\cdot}du + u{\cdot}dm = mc_v{\cdot}dT + u{\cdot}dm. \tag{4.2}$$

Using this formulation, the energy balance for a single zone can be represented as

$$mc_v{\cdot}dT = \sum_i (h_i - u){\cdot}dm_i + \sum_j dQ_j - p{\cdot}dV. \tag{4.3}$$

If a mass flux dm_i enters the zone, it contributes to the energy balance with the specific enthalpy h_i of the originating zone. For a negative mass flux leaving the zone the corresponding enthalpy is the one of the zone itself $h_i = h$.

In order to describe the thermal state within each zone, the ideal gas law is applied. In accordance with the previously defined notation, the differential form with the specific gas constant R_s is chosen:

$$V{\cdot}dp + p{\cdot}dV = R_s \left(T \sum_i dm_i + m{\cdot}dT \right). \tag{4.4}$$

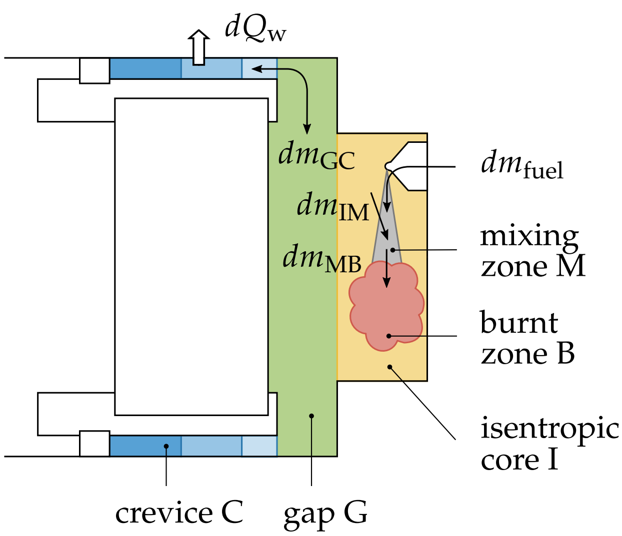

Figure 4.1: Multi-zone thermodynamic model of the combustion chamber.

Furthermore, the overall system of zones has to satisfy the global conservation equations. Including all zones n, the volume conservation can be formulated as

$$\sum_{i}^{n} dV_i = dV_g, \tag{4.5}$$

where the global change in volume dV_g is known at any time from the piston position measurements. Since leakage losses at the RCEM are negligible, the change in mass in the overall system corresponds to the injected fuel mass:

$$\sum_{i}^{n} dm_i = dm_{\text{fuel}}. \tag{4.6}$$

Additionally, mass conservation also implies that the mass flow between two arbitrary adjacent zones X and Y follows the simple correlation

$$dm_{\text{XY}} = -dm_{\text{YX}}, \tag{4.7}$$

meaning that any mass flow entering zone Y from zone X has to be equal to the mass flow leaving zone X for zone Y. X an Y are place holders for the different zones shown in Fig. 4.1. When put together for all the zones in the system, these equations allow the formulation of a system of linear differential equations for each time step, which can be solved for the burnt fuel-air mass flow dm_{MB} that leaves the mixing zone M and enters the burnt zone B.

4.1.2 Heat Loss Model

Heat loss models based on quasi-steady state heat transfer assumptions have been known for a while and are still most commonly used in internal combustion engine analysis due to their simplicity [5, 107]. They rely on the premise that heat transfer during compression and expansion can be described similarly to heat transfer in fully developed, steady channel flow. This implies that the Nußelt assumption is valid and that the Nußelt number can be expressed as a function of Reynolds and Prandtl number. Several authors have shown that the complex heat transfer phenomena involved within a charge compressed and expanded by a piston are highly transient, and therefore have proposed corrections to the quasi-steady state heat transfer models [6, 38, 50].

Besides the fact that they often include application-dependent model constants, none of these models is applicable to the RCEM with its crevices contributing about 10-15% to the volume at TDC. The largest contributors are a deep annular crevice at the piston, the gaps at the injector mounts and volume reductions, and the inlet and outlet channels (see Fig. 3.3). These crevices substantially enhance the transient behavior, especially when comparing experiments with a different center of combustion relative to TDC and therefore a different pressure history. Another argument for a customized heat loss model is that rapid compression of a quiescent charge in the RCEM causes an initially laminar boundary layer, which is preserved during the compression phase [51].

Starting from the heat loss model for a rapid compression machine by Lee and Hochgreb [51] the heat losses at the RCEM have been investigated in detail [25, 26]. Their model consists of a laminar boundary layer and a very thin cold piston crevice volume, which is assumed to remain isothermal at wall temperature due to its high surface-to-volume ratio. The laminar boundary layer follows the compression and expansion of the isentropic core and is resolved numerically. It could be shown that for the RCEM the heat losses caused by the boundary layer are small and can therefore be neglected [25].

The multi-zone model described in Sec. 4.1.1 can be solved for the actual heat losses dQ_w instead of for the burnt mass flow dm_{MB} if no mixing zone and burnt zone are present in an unfired experiment. Such unfired experiments are therefore used to assess and validate different heat loss model assumptions, as shown in Fig. 4.2. If assumed isothermal, the crevice directly responds to the negative pressure gradient after TDC, resulting in negative losses. However, a comparison with the actual losses shows that the isothermal assumption is not justified because it does not allow for the thermal inertia observed in the experiment. The reason for this lies in the geometry of the crevices, which show a surface-to-volume ratio too low for instant temperature equalization with the chamber wall.

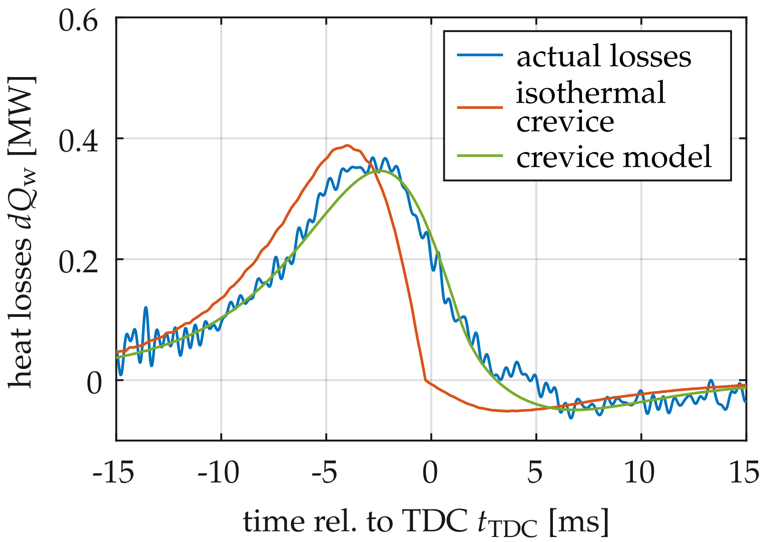

Figure 4.2: Comparison of isothermal crevice and laminar heat transfer model assumptions to actual losses calculated from an unfired experiment with 75 bar / 780 K at TDC.

If the isothermal crevice assumption is rejected, not only the crevice volume but also the geometry has to be considered. The various crevices in the RCEM combustion chamber have different geometries and it would be very difficult to resolve them all. However, all of them have a very low width compared to the depth. Heat transfer therefore results in a strong longitudinal temperature difference within the crevices, which needs to be resolved for a better representation of the transient behavior. This is achieved by modeling only a single substitute crevice.

Figure 4.3 shows the discretization of the substitute crevice into n zones of constant volume. The volume discretization is logarithmically spaced with the smallest elements close to the inlet of the crevice, where the strongest temperature gradients occur. Since the crevice is modeled with a constant width, the surface area of each element is proportional to its volume. For

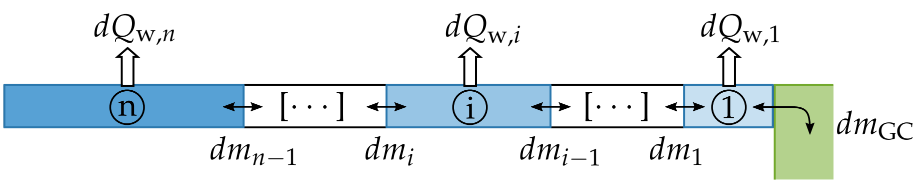

Figure 4.3: Discretization of the crevice volume with n volume elements.

each element i in the crevice the conservation equations (4.3), (4.4) and (4.7) apply, where dV is set to zero.

In order to keep the model simple, the transversal temperature profile is not resolved and the temperature gradient at the wall cannot be determined directly. Strongly simplified, the boundary layer thickness is assumed to be constant, meaning that the temperature gradient at the wall scales with the difference between the temperature T_i of element i and the wall temperature T_w. Furthermore, the temperature dependence of the thermal conductivity $\lambda(T_i)$ needs to be considered. This results in a formulation of the wall heat loss $dQ_{\mathrm{w},i}$ proportional to

$$dQ_{\mathrm{w},i} \propto \lambda(T_i) \cdot V_i \cdot (T_i - T_\mathrm{w})\,. \tag{4.8}$$

The overall wall heat loss in the crevice is the sum over all n crevice elements:

$$dQ_\mathrm{w} = \sum_{i=1}^{n} dQ_{\mathrm{w},i}. \tag{4.9}$$

The proportionality constant in equation 4.8 is determined for the substitute crevice by model calibration. Figure 4.2 shows that good agreement with the actual losses can be achieved by the proposed crevice heat loss model.

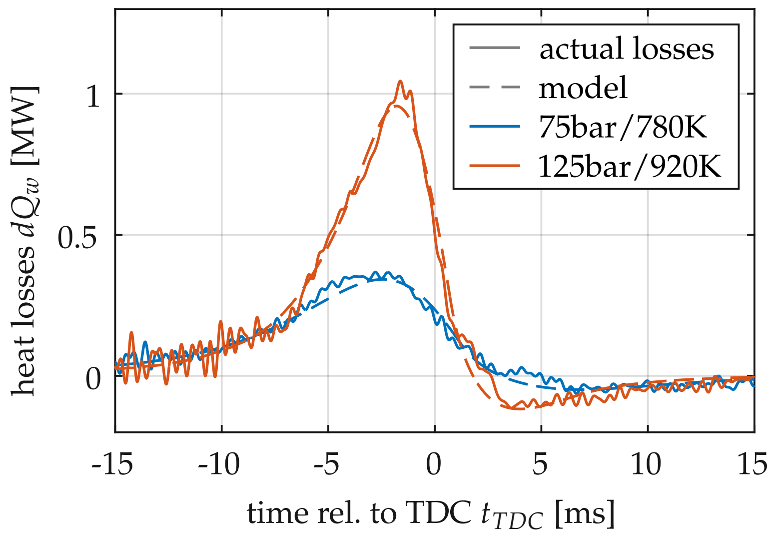

Figure 4.4: Performance of the heat loss model for two unfired experiments at different operating points.

To demonstrate the performance of this model, it is applied to another unfired experiment at a strongly increased compression ratio and therefore higher temperature and pressure at TDC in Fig. 4.4, using the same model constant. The strong overshoot in heat losses prior to TDC as well as the faster drop during expansion are captured very well. The corresponding longitudinal temperature profiles in the crevice at +3 ms and -3 ms after TDC are presented in Fig. 4.5 for a crevice discretized wit $n = 8$ elements. The hot gas fed to the crevice during compression leads to high temperatures close to the inlet, resulting in an enhanced heat transfer and the observed steep rise in heat losses. When expanding, the temperature in the crevice drops slightly below wall temperature, causing a small reversed heat flux.

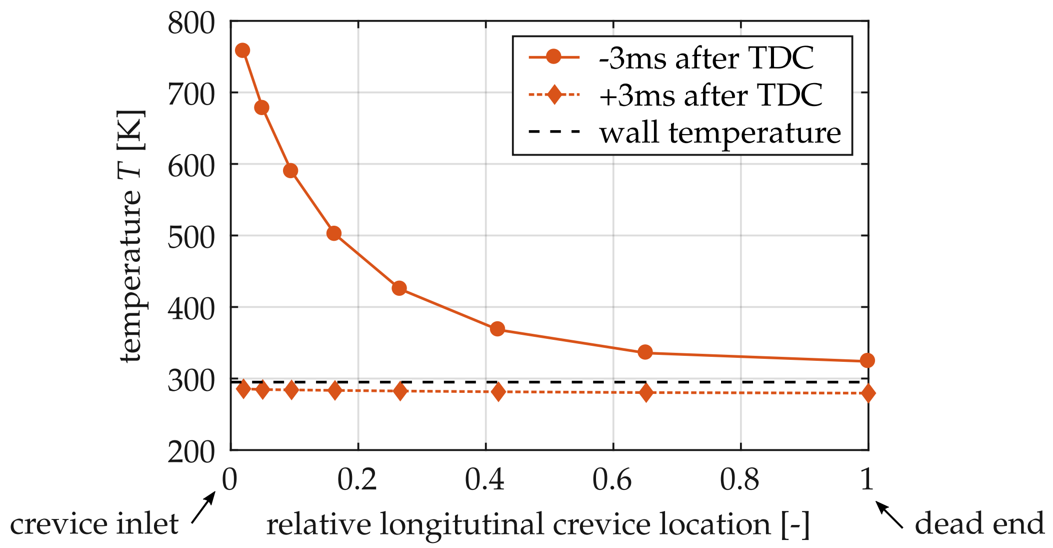

Figure 4.5: Longitudinal temperature distribution in the crevice (n=8) during compression and expansion (125bar/920K at TDC).

4.1.3 Mixture and Combustion Model

The purpose of the introduction of a separate mixing and combustion zone is to represent the spatially confined heat release from combustion of a single pair of jets in the relatively large combustion chamber, without the ambition to formulate accurate predictions about the type of combustion or even pollutant formation. Therefore, a very simple model of the mixture formation is applied by fixing the entrained air mass dm_{air} to be directly proportional to the fuel mass flow dm_{fuel}. Advantageously, this causes the mixture fraction to be constant in time at a specific fuel-air equivalence ratio ϕ. The air mass dm_{IM} supplied to the mixing zone (M) from the isentropic core zone (I) can thus be calculated from the injected fuel mass dm_{fuel} via

$$dm_{\mathrm{IM}} = dm_{\mathrm{air}} = \frac{1}{(m_{\mathrm{fuel}}/m_{\mathrm{air}})_{\mathrm{st}}} \cdot \frac{1}{\phi} \cdot dm_{\mathrm{fuel}}. \tag{4.10}$$

The ratio between fuel and air mass at stoichiometry contained in this equation is obtained from the molar oxygen demand at stoichiometry $n_{\mathrm{O_2,st}}$ and the molar mass ratio $M_{\mathrm{fuel}}/M_{\mathrm{air}}$ for methane as the main constituent of natural gas by

$$\left(\frac{m_{\mathrm{fuel}}}{m_{\mathrm{air}}}\right)_{\mathrm{st}} = \frac{1}{n_{\mathrm{O_2,st}}\,(1+0.79/0.21)} \cdot \frac{M_{\mathrm{fuel}}}{M_{\mathrm{air}}} \tag{4.11}$$

$$= \frac{1}{2\,(1+0.79/0.21)} \cdot \frac{16.04}{28.95} = 0.0582\,\frac{\mathrm{kg_{fuel}}}{\mathrm{kg_{air}}}. \tag{4.12}$$

To avoid the need for considering two different fuel species, the energy equivalent mass of methane is added to the mixing zone instead of diesel pilot fuel.

During combustion, part of the fuel/air mixture dm_{MB} is transferred to the burnt zone (B). By restricting the fuel-air equivalence ratio to $\phi \leq 1$, partial oxidation of fuel-rich mixtures that would require for post-oxidation in the burnt zone is avoided. Combustion is then assumed to occur in an idealized single-step reaction with complete conversion. Thus, also the burned zone shows a temporally constant species distribution and the physical properties (R_{s}, $c_v(T)$) and state variables ($u(T)$, $h(T)$) can be calculated as a function of temperature only using the NASA-polynomials [56].

If the enthalpy of formation is contained in the specific enthalpy h of the substances in M and B, this total enthalpy remains constant during combustion. The difference in enthalpy of formation Δh_f is directly converted into sensible heat of the products, as shown in Fig. 4.6. This allows the calculation of the heat release rate dH_{HR} describing the combustion progress via:

$$dH_{\mathrm{HR}} = -\Delta h_f \cdot dm_{\mathrm{MB}} = \left(h_{\mathrm{M}}\left(T_{\mathrm{M}}\right) - h_{\mathrm{B}}\left(T_{\mathrm{M}}\right)\right) \cdot dm_{\mathrm{MB}}. \tag{4.13}$$

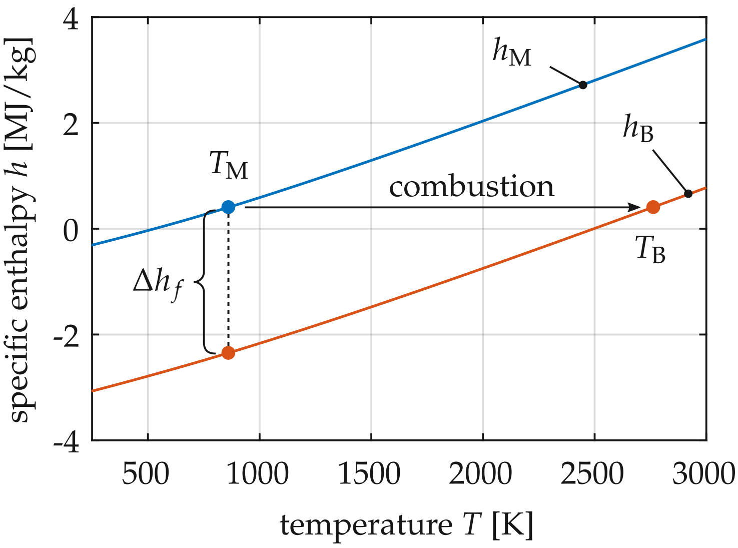

Figure 4.6: Specific enthalpy of a stoichiometric NG/air-mixture (M) and its burnt products (B); difference in enthalpy of formation Δh_f is released during combustion.

4.1.4 Thermodynamic Analysis

Based on a set of parameters derived from the heat release rates the ignition and reaction progress are described. The definition of these parameters is illustrated in 4.7. Since the low amount of pilot fuel results in only minor heat release, pilot ignition is difficult to be captured accurately by a heat release rate threshold. The time of pilot ignition is therefore determined by the first signal detected with the OH* camera system instead. This is feasible since the pilot acts as ignition source independent of the experimental configuration. The following parameters characterize the process up to successful ignition of the natural gas jet:

- The **pilot ignition delay** $\tau_{\mathrm{ign,P}}$ describes the delay between start of injection and auto-ignition of the diesel pilot fuel. It is governed by fuel evaporation, mixture formation and chemical decomposition

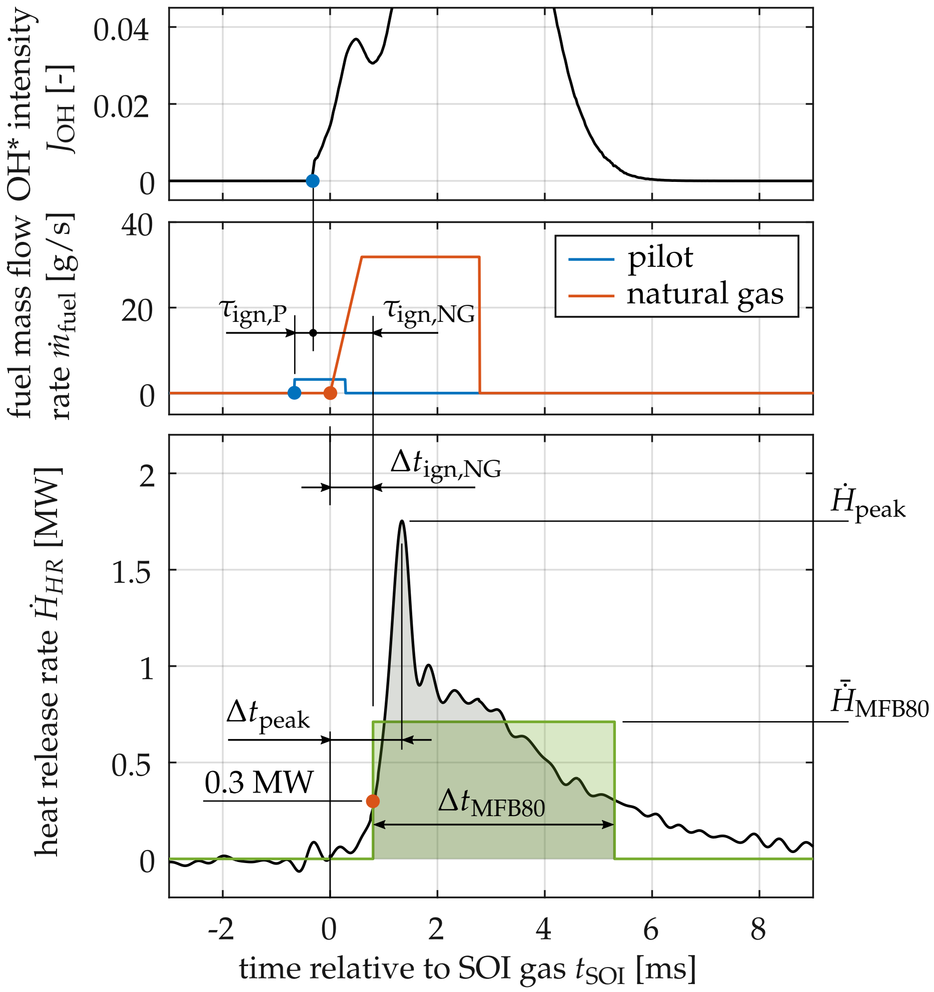

Figure 4.7: Determination of characteristic parameters from heat release rate, fuel mass injection rates and OH* chemiluminescence intensity.

processes and is therefore strongly dependent on chamber pressure and temperature.

- Since the gas jet is ignited not by auto-ignition but by interaction with the pilot, the **natural gas ignition delay** $\tau_{ign,NG}$ is defined as the time between pilot ignition and natural gas ignition. Natural gas ignition is assumed successful when the heat release exceeds a threshold of 0.3 MW for the first time.[1] The natural gas ignition delay allows to assess the interaction between the two jets.

[1]Depending on the degree of premixing, pilot combustion was found to result in a peak of up to 0.25 MW in heat release. The selected threshold value therefore allows to reliably identify the gas jet ignition even if it occurs in close succession to pilot ignition.

- Analogous to the pilot ignition delay, the time between start of injection and ignition of the natural gas can be calculated. This **natural gas ignition offset** $\Delta t_{\mathbf{ign,NG}}$ allows to characterize the extent to which the gas jet has already propagated at the time of ignition. $\Delta t_{\mathrm{ign,NG}}$ is thus an easy to determine quantity describing the degree of premixing at the onset of natural gas combustion.

The main heat release occurs due to the combustion of natural gas after ignition by the pilot. In order to provide a simplified description of its evolution, the following pairs of parameters are defined:

- The maximum rate of fuel conversion as a characteristic point in the heat release is described by the **peak heat release rate** $\dot{H}_{\mathbf{peak}}$, and its position relative to the start of injection by means of the **peak offset** $\Delta t_{\mathbf{peak}}$ relative to the start of injection.
- The **combustion duration** $\Delta t_{\mathbf{MFB80}}$ for consumption of 80% of the fuel (mass fraction burned) and the resulting **mean heat release rate** $\bar{\dot{H}}_{\mathbf{MFB80}}$ within this period are integral parameters describing the evolution of heat release.

4.2 Simultaneous SG/OH* Imaging

The raw image pairs from the SG and OH* systems are processed to assure direct comparability between different test runs and to optimize the dynamic range for better visual interpretation. Following an image registration procedure, the processed images are then superimposed using a two-dimensional colormap. Thereby the information obtained by the SG and OH* systems can be displayed and interpreted within one single frame.

4.2.1 Image Enhancement

The intensity distribution of the high-speed images is adjusted in two steps. At first, the intensity range is scaled by normalization in order to utilize the whole dynamic range, remove systematic measurement errors and assure comparability between different measurements. The linearly normalized intensity J_{N} of a raw pixel intensity value J is calculated by:

$$J_{\mathrm{N}} = (J - J_{\mathrm{low}}) \cdot \left(\frac{J_{\mathrm{N,high}} - J_{\mathrm{N,low}}}{J_{\mathrm{high}} - J_{\mathrm{low}}} \right) + J_{\mathrm{N,low}}. \tag{4.14}$$

This normalization is specified by the transformation of two selected points in the image intensity spectrum (J_{low}, J_{high}) to the desired normalized levels ($J_{\mathrm{N,low}}$, $J_{\mathrm{N,high}}$), as shown in Fig. 4.8 on the left.

The lower intensity value J_{low} corrects the black level, which is distorted by systematic measurement errors that add up to the image intensity. For the SG system this error is mainly caused by a small share of the incident illumination being reflected by the glass piston surface and detected by the SG camera without having passed through the measurement volume. In a similar manner the imperfect UV-bandpass filter causes some of the SG illumination to be detected by the OH* camera. J_{low} is directly obtained from the images for each measurement individually.

For a direct comparison of SG images from different test runs with slightly different background illumination intensity (~0.75-0.85), the illumination intensity is normalized to a value of 0.8 using J_{high}. Possible reasons for this scatter are deposits on the mirrored chamber wall or a slightly altered iris aperture diameter at the pinhole. In contrast, the upper

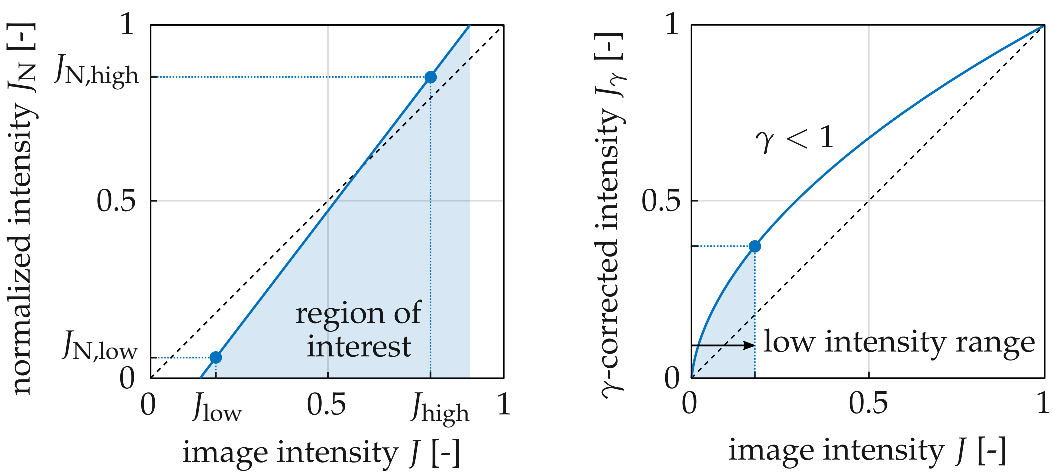

Figure 4.8: Effect of normalization (left) and gamma correction (right) on the image intensity distribution.

brightness value of the OH* images is not changed. The intensity levels for image normalization stated in Tab. 4.1 represent typical values and are determined individually for each set of images.

Table 4.1: Intensity levels for image normalization.

	J_{low}	$J_{\mathrm{N,low}}$	J_{high}	$J_{\mathrm{N,high}}$
SG	∼0.09	0	∼0.75-0.85	0.8
OH*	∼0.04	0	1	1

Even though scaled to cover the desired intensity range after normalization, both the SG and OH* recordings contain most of the information in the low intensity range. Since the SG system is highly sensitive, the strong density gradients present with direct-injection cause the jet region of interest to appear very dark. On the other hand, OH* chemiluminescence covers a wide range of intensities. While stoichiometric methane flames or diffusive diesel oxidation show strong OH* chemiluminescence, the emission intensity is low for lean or rich mixtures [69]. As overexposure would destroy the image intensifier, saturation has to be avoided at any time by selecting a low intensifier gain. To improve the resolution in the low intensity range, all normalized SG and OH* images are therefore γ-corrected with the following power-law expression:

$$J_\gamma = J_{\mathrm{N}}^{\gamma}, \quad \text{where } J_{\mathrm{N}} \in [0,1]. \tag{4.15}$$

Selecting $\gamma < 1$ as shown in Fig. 4.8 on the right results in a non-linear stretch of the dark image regions over a wider intensity range. One major advantage of the gamma transformation is the preservation of the image's dynamic range without any clipping in the bright regions of the image. For both SG and OH* image processing, a value of $\gamma = 0.6$ was selected.

4.2.2 Image Registration

Since the imaged area, the resolution and the orientation of the SG and OH* images do not match exactly, it is necessary to identify the spatial transformation matrix for the direct mapping between both types of

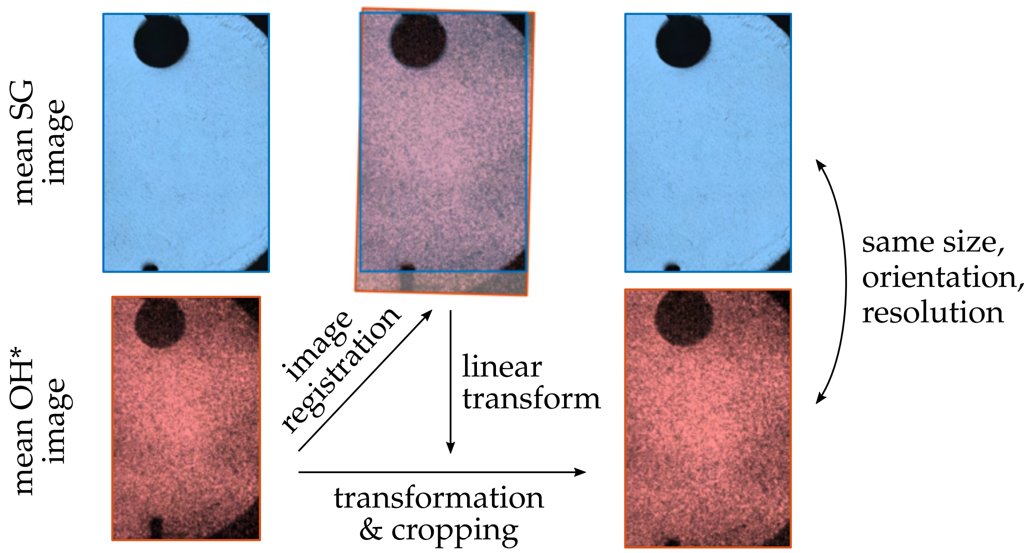

Figure 4.9: Image registration and transformation procedure for mapping between SG and OH* images. Image registration performed with mean images from prior to injection.

images. This transformation matrix is obtained by image registration individually for every test run using the first few image pairs before injection starts, as illustrated in Figure 4.9.

An existing optimizer in MATLAB may be used to search for the best match between two images if these images show the same structures. As the OH*-filter transmits a very small share of the light from the SG background illumination, the structures from the SG image representing the surface mirror geometry are contained in the OH* images as well. However, the structures become visible only after averaging the first 50 images prior to injection since the low intensity images are superimposed by intensifier noise. The linear transform representing the best match is then applied to all subsequent OH* images. After cropping the transformed OH* image, an image pair with same size, orientation and resolution is obtained. Observations made in both images can thus be spatially correlated.

4.2.3 Jet Penetration and Flame Position Measurements

An automated image processing routine is used to locate image information, such as the jet penetration or flame position. After the imaging system is set up, the image resolution in pixels per millimeter is determined with a target image. The target is a transparent foil with a grid of known spacing printed on it, which is placed in front of the cylinder head mirror. From this target image, the distance between the grid lines is then determined by auto-correlation. Depending on the focal length of the focusing lens selected, the image resolution is about 0.12-0.2 mm/pixel.

In a second step, the position of the injectors on the image is localized. Since the gas injector is represented by a circular dark shadow in the SG image, it can be localized using a circular Hough transform. Starting from the center of the gas injector, the position of the pilot injector orifice can then be determined by means of the known injector offset x and y. If, for example, the jet tip or the flame are detected from the SG or OH* image, the position relative to the injectors can be calculated via the Euclidean distance and the image resolution. Since the orientation of the two jet axes is known as well (α), the assumption of a jet cone angle allows to apply a virtual jet cone, and thus to restrict e.g. the flame position measurement to one of the fuel jet domains.

4.2.4 Superposition and Physical Interpretation

For direct spatial correlation of the information contained in a pair of simultaneously recorded SG and OH* images, it is useful to display them superimposed in one single image. However, any loss of information due to the superposition must be avoided. For this purpose, every possible combination of SG and OH* intensity is assigned a unique color by the application of a two-dimensional colormap. The colormap and the process used to create combined SG/OH* images in this work are shown in Fig. 4.10.

The colormap is designed to show a monochrome scale if only a SG image (blue) or only a OH* image (red) is available or to be considered. The individual images in Fig. 4.10 are therefore colored according to the respective axis in the colormap. If two associated images are superimposed, every pixel color value is looked up in the colormap according to the respective SG and OH* intensity values. The colormap entails a wide variety of colors that indicate the relation between both individual intensities. Yellow is chosen for similar SG and OH* intensity values, while green is assigned to a dominating SG intensity and orange to a dominating OH* intensity. Furthermore, the brightness is an indicator for the overall intensity from both images and therefore increases radially from the origin at $I_{\mathrm{SG}} = 0$ and $I_{\mathrm{OH}^*} = 0$. The image pair shown in Fig. 4.10 was recorded at a time when the flame propagates within the gas jet after ignition by the pilot. This example is used hereafter to describe the information visible in the combined SG/OH* images. At first, the effects that contribute to the SG and OH* intensity values will be explained individually before the 2D-colormap is applied for a combined analysis.

As a result of the bright and constant SG background illumination and the limitation of any OH* chemiluminescence to the fuel-containing regions in the jets, the background of the combined SG/OH* image appears always blue. It can be seen from the tip of the NG jet that very low SG intensity is obtained even in regions with a high degree of mixing and no visible reaction. Regions with high I_{SG} within a jet region are therefore attributable to light emitted by the reacting zones in the visible range. Furthermore, flow structures in the SG images caused by fuel-air mixing differ in their appearance from structures caused by volumetric luminescence. Due to the collimated SG illumination fine turbulent mixing scales become visible, whereas the reacting structures cause homogeneous light emission and therefore may only be resolved if an image aperture was used. Although chemiluminescence contributes to the visible wavelength spectrum of a flame as shown in Fig. 3.7, the black-body radiation of the hot particle matter clearly dominates at the prevailing temperatures. Since the optical system can be regarded as a telephoto lens with strong light gathering capability (approx. 800mm, f:2), the bright soot radiation partly leads to overexposure in the SG image despite the very short exposure time.

Sufficient filtering of the wavelength spectrum to remove all parts not attributable to the OH* radical is important for an evaluation of the images recorded by the OH* camera, especially with respect to the intense radiation from soot. A very low cross-sensitivity of the OH* system for soot luminescence can be directly proven by the shown SG/OH* image. The strongly sooting region at the tip of the pilot jet ① extends to the interaction zone between the jets ②. But while strong OH* chemiluminescence is detected on the diesel side (yellow), this is not the case in the interaction

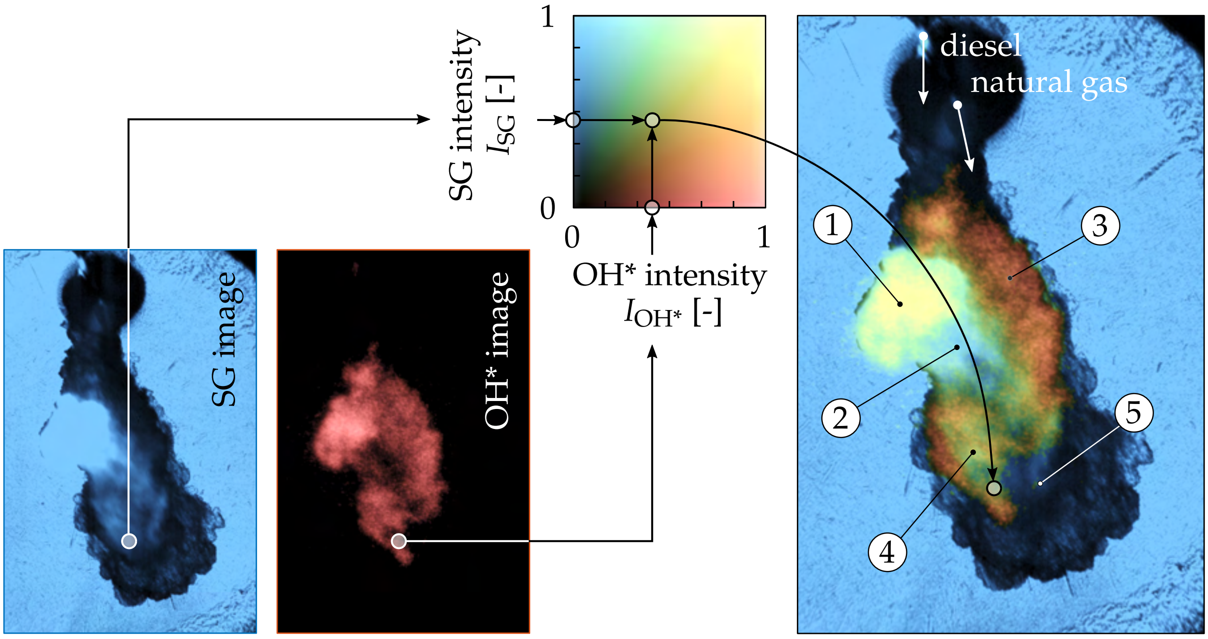

Figure 4.10: Application of a customized 2D-colormap to the SG and OH* images for superposition.

region (blue). Such a differentiation is only possible if the sensitivity of the OH* camera system for soot-luminescence is sufficiently low.

Basically, both measurement techniques record a line-of-sight integrated signal. But since zones heavily contaminated with soot particles are optically dense, most of the radiation from hot soot particles that reaches the SG camera stems from the outer regions of the respective zone. This furthermore implies that light from OH* chemiluminescence only reaches the camera detector undisturbed if it originates from zones not masked by particle matter. Taking all these considerations into account, the following observations from Fig. 4.10 can be made:

① The tip of the pilot jet shows overexposure in the SG image due to strong soot luminescence, combined with intense OH* chemiluminescence (yellow). Since both signals are observed across the entire diesel jet tip region, they must both originate from the outermost part of the jet. In accordance with the findings by Dec [18], this thin region in the outer jet shear layer is where the partially oxidized fuel from the jet core is subject to diffusive burnout.

② When the two jets interact, the products from diesel fuel combustion are entrained into the gas jet. The resulting soot-contaminated zones without detectable oxidation (no OH* chemiluminescence) appear in light blue color.

③ In the wake of the diesel jet, as well as in the gas jet opposite to the diesel pilot, only OH* chemiluminescence is observed (red). This means that reaction occurs without soot being involved during either the late burnout phase of rich mixtures or the combustion of sufficiently premixed zones.

④ Downstream of the interaction zone between the jets, the gas jet shows structures that appear red at the edge via orange to green in the center. This characteristic pattern is caused by the three-dimensional structure of partially-premixed reaction zones. In the fuel-rich inner regions of these structures soot is formed while the leaner regions at the outside exhibit only OH* chemiluminescence.

⑤ Hot combustion products and soot are transported to the tip of the gas jet by the high velocities in the core. However, oxidation of the resulting mixture must be low, as no OH* chemiluminescence is observed.

The single image pair in Fig. 4.10 was only selected to explain how the superimposed SG/OH* recordings can be interpreted. A comprehensive analysis of the HPDF combustion process can be found in the results, e.g. Sec. 6.2 and 7.2.

4.3 CFD Analysis

In order to provide further information complementing the experimental results, a CFD model for natural gas HPDF combustion was developed in the framework of the same research project by Jud *et al.* [40–42]. Apart from combustion analysis, the model is applied to the design of a combustion chamber geometry for a wall-bounded gas jet in Sec. 7.1.

4.3.1 Model Description and Performance

The CFD analysis is based on the CONVERGE [84] solver for Reynolds-Averaged Navier-Stokes (RANS) equations, and combustion is solved by detailed chemistry. Each cell is considered a perfectly stirred reactor, and clustering of similar cells is applied to limit the computational effort while adaptive mesh refinement (AMR) adjusts the cell size to the local gradients. For turbulence modeling the renormalization group (RNG) k-ϵ model [108] is applied. Diesel injection is modeled with a Lagrangian-Eulerian approach, injection and breakup are treated with the blob injection model by Reitz and Diwakar [82] and the KH/RT model [81]. To account for droplet collision, the model of Schmidt and Rutland [91] is used. Detailed chemistry calculations are performed using the SAGE solver, which is included in CONVERGE and based on SUNDIALS (suite of nonlinear and differential/algebraic equation solver) [34] CVODES solver for stiff and nonstiff ODE systems.

By considering all species, this modeling approach has the advantage of pollutant formation calculations being inherently conducted. Performing detailed chemistry calculations on the grid is particularly suitable for HPDF combustion, as premixed and diffusive combustion including auto-ignition can occur at the same time at different locations in the combustion chamber. Furthermore, the two different fuels diesel and natural gas are directly represented if a suitable reaction mechanism is selected, which is often very difficult with conventional combustion models.

Thus, the quality of the results significantly depends on the availability and selection of an appropriate reaction mechanism for the relevant temperature, pressure and mixture range. Existing mechanisms have therefore been extensively investigated and validated for a combination of diesel and natural gas at engine conditions. It was concluded that a mechanism developed at Chalmers University [98] provides the best results and is therefore used in this work.

Figure 4.11 compares the numerically and experimentally determined heat release rates of conventional and partially-premixed HPDF. The characteristic shape of heat release, consisting of a fast peak during premixed combustion followed by a slow mixture-limited burnout, is

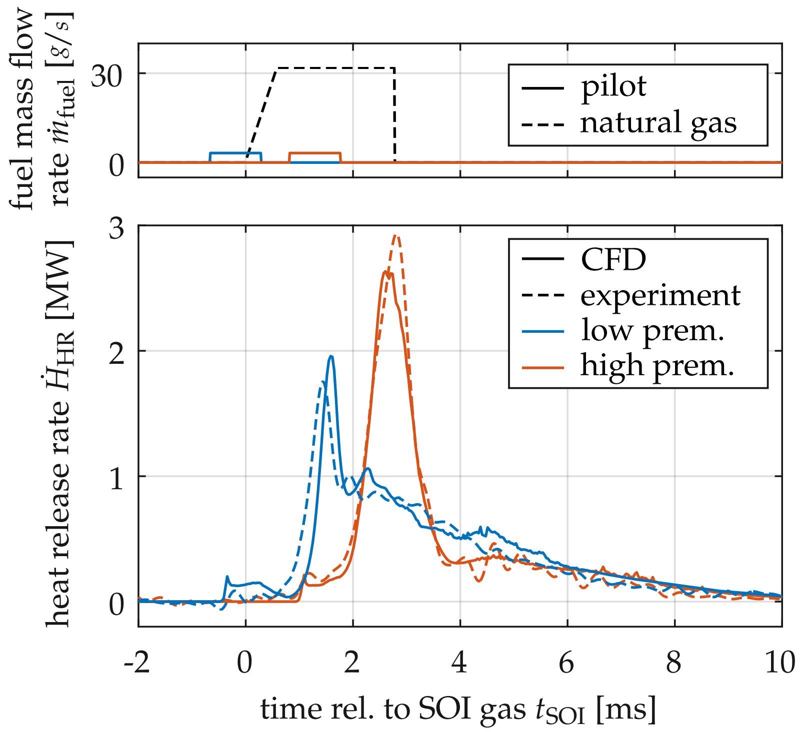

Figure 4.11: Comparison of heat release rates from the experiment and from CFD calculations for conventional and partially-premixed HPDF combustion ($p_{\mathrm{TDC}} = 125\,\mathrm{bar}$, $T_{\mathrm{TDC}} = 920\,\mathrm{K}$).

reproduced very well. This good agreement justifies the use of the numerical results for analyzing the mixture distribution and pollutant formation during combustion. The interested reader is referred to [40–42] for more details on the model and the validation procedure.

4.3.2 Combined Mixture and Combustion Progress: the ϕ-T Plot

With direct fuel injection, mixture formation and combustion take place simultaneously within the combustion chamber at similar timescales. It is reasonable to include them in a joint analysis, as the combined mixture and reaction progress strongly governs pollutant formation. Since the experiment is not able to provide appropriate quantitative results, CFD calculations are used to assess the evolution of fuel distribution in the ϕ-T parameter space. The resulting ϕ-T plots have proven to be a useful tool for illustrating pollutant formation mechanisms in diesel engine combustion [2, 9, 46, 68].

Figure 4.12 shows a representative ϕ-T plot (right) and the burnt/unburnt mixture distribution (left). In order to ensure the fuel allocation in both plots to be unaffected by the reaction path and the intermediate species involved, the equivalence ratio of each computational cell is determined by means of the atomic ratio of carbon, hydrogen and oxygen in its mixture. The fuel mass in each cell is then calculated from the cell mass, the equivalence ratio and the known fuel composition. The ϕ-T parameter space is discretized into bins of $\Delta T = 20\,\mathrm{K}$ and $\Delta\phi = 0.05$, and the fuel mass of all cells in the ϕ and T range of each bin is summarized. The fuel mass distribution obtained this way is then normalized by an arbitrary but constant value.

Since reacting mixtures very quickly exceed the charge temperature T_{ch}, this temperature can be used as a simple threshold for a robust classification into burnt and unburnt mixture, independent of the equivalence ratio. This way, the mixture distribution for unburnt and burnt fuel shown in Fig. 4.12 on the left is obtained directly from the ϕ-T plot on the right. Both plots in the figure refer to the same point in time when the diesel pilot fuel has already been injected, is completely burned and its products are continuously becoming leaner. Natural gas injection has been started but the gas jet is not yet ignited. A wide range of equivalence ratios is computed for the natural gas jet mixture, with the largest fuel share below $\phi = 3$.

When fuel is injected, it mixes with the charge gas and the mixture temperature T_{mix} directly correlates with the equivalence ratio prior to the onset of reaction. Unburnt fuel is therefore found on a clearly defined mixing line. Reaction is accompanied by an increase in temperature, hence any reacting fuel will detach from the mixing line towards the adiabatic flame temperature line T_{ad}. The adiabatic flame temperature, which is calculated from the state at the mixing line, allows to assess the deviation from chemical equilibrium. After ignition, the predominantly rich mixture of the natural gas jet will react at first by fast partially-premixed combustion. Subsequently the reaction progress is limited by mixture formation and fuel burnout is only achieved via the diffusion flame at the jet shear layer.

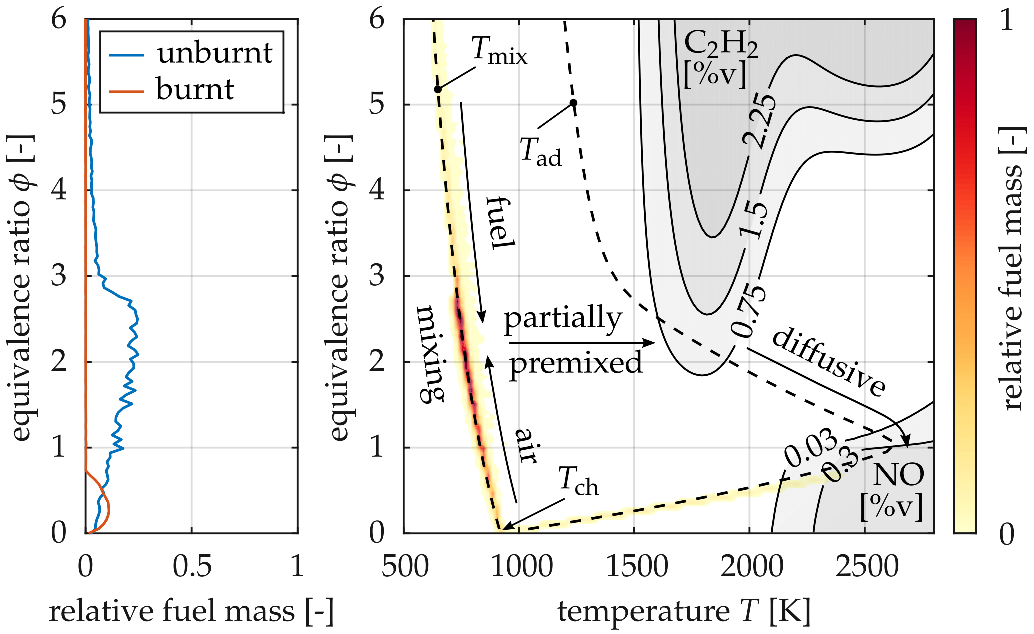

Figure 4.12: ϕ-T map showing the mixture and combustion progress (right), and burnt/unburnt mixture distribution (left) at a single time step prior to NG ignition with p_{ch}=125 bar/T_{ch}=920 K; contour lines indicate species concentrations based PSR calculation with 2 ms residence time at constant p and T.

The figure also includes characteristic regions for formation of the soot precursor acetylene (C_2H_2) and of nitrogen monoxide (NO), marked by gray contour levels. While the NO concentration can be calculated directly with the reaction mechanism, an additional soot model would be required to predict soot particle inception, growth, agglomeration and oxidation. However, a detailed study for different hydrocarbon fuels has shown that both the soot occurrence and yield are dominated and thus well represented by the concentration of acetylene [44].

Following the approach of Kitamura *et.al.* [44], the depicted volume fractions are determined by perfectly stirred reactor (PSR) calculations at constant pressure and temperature and a residence time of 2 ms. This is a representative time scale for the combustion duration in a reciprocating engine, corresponding to 24 degrees of crank angle at 2,000 rotations per minute. The PSR calculations are done using the GRI3.0 mechanism [94] with pure methane as fuel. Due to this simplified approach, where an initially unburned mixture with a certain equivalence ratio is kept at constant temperature for an engine-relevant time scale, the resulting contours only indicate regions where the species are expected to be formed. However, the stated values cannot be used to quantify emission concentrations at highly transient in-cylinder conditions.

The ϕ-T diagram has originally been introduced to show how the mixture and reaction progress in diesel combustion contributes to pollutant formation. Rich zones close to the lift-off length react partially-premixed (up to about $\phi = 6 - 8$ [75, 93], see also Sec. 2.2.1). As a consequence of the lack of oxygen, soot particles are formed in these zones. The partially oxidized, rich mixture only burns out when becoming stoichiometric in the shear layer at the jet periphery, where a mixture-limited turbulent diffusion flame is formed. As the temperature is high and excess oxygen becomes available at stoichiometry, the shear layer is also where NO is formed. However, these conditions favor the oxidation of a large share of the soot particles as well (not shown in the figure). Common measures for emission reduction and their effects can be demonstrated with this diagram, such as the reduction of oxygen concentration and combustion temperature by EGR, or the improved mixture formation by higher injection pressures or by longer ignition delays for partially-premixed LTC [2, 9, 46, 68].

5 Diesel Pilot Ignition Source

In HPDF combustion, diesel pilot fuel auto-ignition is responsible for the onset of reaction and the location of the initial reaction zone. It is followed by the spatial evolution of the pilot fuel flame zone and by the onset of natural gas combustion due to the interaction of both jets. Hence it is essential to understand the pilot ignition behavior in detail before considering combustion of the main fuel. In this chapter, ignition timing, ignition location and burnout of a very small amount of diesel pilot fuel (micro-pilot) are investigated first for different chamber conditions and without gas injection present. These investigations provide the framework for specification of the operating conditions in the dual-fuel experiments. In the last section of this chapter, the influence of the natural gas jet on pilot ignition is analyzed. A wide range of spatial and temporal interaction between the fuel jets is investigated for this purpose by altering the injection timing and the angle between both jets. The results serve as the basis for the experiments on natural gas combustion in Chapters 6 and 7.

5.1 Micro-Pilot Combustion Characteristics

The phenomenological description of diesel combustion in Sec. 2.2 reveals a strong dependence of the diesel ignition delay on the pressure and temperature in the combustion chamber. Furthermore, it explains how the mixture distribution at the time of ignition affects the combustion characteristics. The pilot mixture dwell $\Delta t_{\mathrm{dwell}}$, defined as the offset between EOI and ignition, serves as an indicator for the degree of premixing by correlating injection and ignition timing. Due to the small amount of fuel and the associated short injection duration of micro-pilot jets, ignition may occur after the end of injection even at relatively high compression ratios. Depending on the combustion strategy, pilot fuel injection may be initiated early during the compression stroke, resulting in delayed ignition even if the engine's compression ratio is not altered.

In order to investigate the ignition behavior of a micro-pilot jet under different conditions, experiments with the RCEM operated in a wide range of compression ratio and initial charge pressure prior to compression were conducted. As mentioned when introducing the RCEM test rig (see Sec. 3.1), temperature and pressure at TDC are thereby adjusted independently. Figure 5.1 shows the diesel micro-pilot ignition delay determined by optical image analysis for a pilot fuel mass of $m_\mathrm{P} = 1.5\,\mathrm{mg}$, an injection pressure of $p_\mathrm{P} = 1000\,\mathrm{bar}$ and an injection duration of $t_\mathrm{inj,P} = 0.75\,\mathrm{ms}$. Injection is started about 1.5 ms before TDC in order to allow for quasi-steady combustion chamber conditions during ignition delays of up to 3 ms. Tested combinations are marked with black dots and the ignition delay contour levels are linearly interpolated between them. As expected, the ignition delay increases when charge pressure and temperature are reduced. The diagram also includes the limit for the transition from a negative mixture dwell at high charge temperature or pressure to a positive mixture dwell at lower charge temperature and pressure. As illustrated by two image sequences in Fig. 5.2, this transition has a strong influence on the ignition and combustion progress.

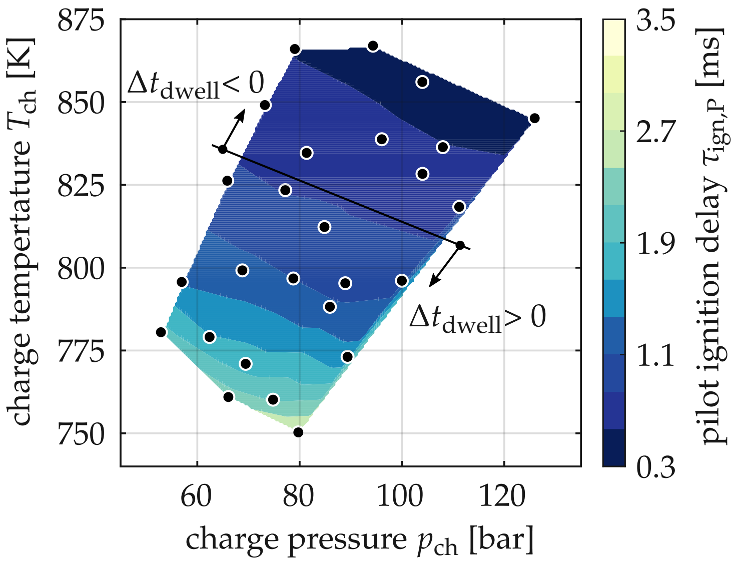

Figure 5.1: Pilot ignition delay for a variation in chamber air pressure and temperature, averaged between SOI and ignition (p_P=1000 bar, m_P=1.5 mg, $t_\mathrm{inj,P}$=0.75 ms).

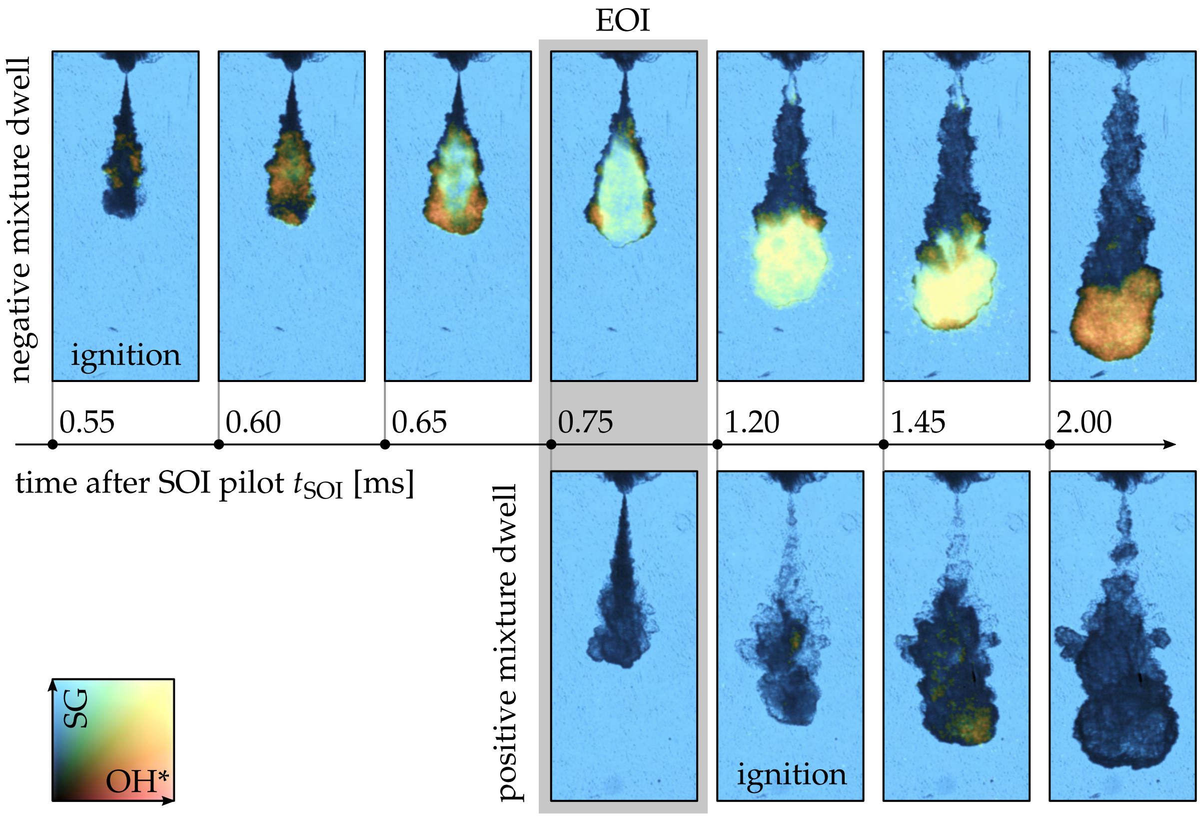

Figure 5.2: Image sequences showing micro-pilot auto-ignition and combustion with negative mixture dwell (p_{ch}=102 bar/T_{ch}=860 K) and positive mixture dwell (p_{ch}=85 bar/T_{ch}=785 K).

If ignition sets in before the end of injection, a negative mixture dwell is obtained. In this case, the mixture field at the time of ignition corresponds to the one present in conventional diesel combustion. Ignition is first observed in the shear layer, where the entrainment of hot charge air is the strongest. The leading vortex at the tip of the jet ignites a little later, when the first soot particles already are detected within the jet core. Soot formed in this central part of the jet can only be oxidized when it reaches the diffusion flame that forms at the outer shear layer. Soot luminescence detected by the SG camera therefore subsequently extends outwards towards the visible boundary of the jet. Strong OH* chemiluminescence can be detected in this same region as well, since the OH radical is strongly involved in the diffusive oxidation process. After the end of injection (EOI), termination of fuel supply and the entrainment wave caused by the sudden momentum deficit lead to a rapid change in spatial mixture distribution. Starting from the nozzle orifice, the mixture becomes leaner first in the upstream region of the jet. The mixture-limited oxidation process of the tip vortex is slow and completed only about 1.5 ms after the end of injection. Soot luminescence disappears first, before the decrease in UV emissions from the OH radical indicates the end of the reaction process.

Pilot fuel ignition and combustion change significantly if the ignition delay exceeds the injection duration ($\tau_{\mathrm{dwell}} > 0$) below about $810 - 830\,\mathrm{K}$. Due to the upstream region of the jet becoming lean very fast, ignition occurs further downstream close to the jet tip. The slight local variations in mixture quality caused by the turbulent structures are sufficient to cause staged ignition. As a result of the strong premixing, no soot formation can be observed at any time. OH* chemiluminescence is significantly lower than with a negative mixture dwell and cannot be detected in all the reacting regions of the jet. Not only the combustion duration is shorter with a positive mixture dwell, but the reaction seems to be completed earlier relative to SOI as well.

5.2 Operating Conditions for Dual-Fuel Experiments

The observed differences in intensity of reaction and in pollutant formation between conventional ($\Delta t_{\mathrm{dwell}} < 0$) and partially-premixed ($\Delta t_{\mathrm{dwell}} > 0$) micro-pilot jet combustion directly affect the overall HPDF combustion process. Consider the intensity of pilot reaction first: Despite an unaltered pilot fuel quantity and thus constant ignition energy, the range of mixture qualities that is able to auto-ignite in the available time is greatly reduced at a positive mixture dwell. This is because build-up of a sufficient pool of radicals is restricted in rich zones by the low temperatures and in lean zones by the low fuel concentration. As a result, any small disturbance of the temperature and mixture field by e.g. the natural gas jet may cause ignition to fail.

Overall soot emissions from HPDF are strongly affected by the diesel pilot, although the pilot fuel share is typically low. Fig. 5.2 shows that soot formed in conventional diesel combustion can only be oxidized very late via the diffusion flame. Interaction with the natural gas jet may inhibit this soot oxidation phase, meaning that soot emissions from the pilot fuel can only be mitigated if their formation is avoided. As introduced in Sec.

2.2.2, partially-premixed diesel combustion is an effective way to do so by excluding rich zones from reaction. Furthermore, partially oxidized pilot fuel containing soot is entrained by the gas jet during natural gas ignition – a process that potentially increases soot formation in the natural gas jet [39]. This influence of the pilot injection on soot formation in the gas jet is discussed in detail in Section 6.2.3.

The conditions in the combustion chamber for all dual-fuel experiments in the present work are set to capture the effect of the diesel pilot mixture dwell on the overall combustion process. One simple way to do so is by a variation of the the injection timing during the compression stroke at a fixed high compression ratio. However, this would result in strongly transient conditions in the combustion chamber that make an interpretation of the results very difficult. It was therefore decided to specify separate operating points with different conditions at TDC, as shown in Tab. 5.1. By fixing the pilot SOI at 1.5 ms before TDC, the conditions for pilot ignition are independent of the relative fuel injection timing between pilot fuel and natural gas injection.

In order to assure reliable ignition in the dual-fuel experiments, the amount of pilot fuel is doubled to $m_\mathrm{P} = 3\,\mathrm{mg}$ (corresponding to an energetic share of 3.75% at the standard load point). This is achieved by doubling the injection pressure as well to $p_\mathrm{inj,P} = 2000\,\mathrm{bar}$, so that the injection duration is only slightly increased by 0.1 ms to $t_\mathrm{inj,P} = 0.85\,\mathrm{ms}$. The increase in injection pressure was found to show no noticeable effect on the ignition

Table 5.1: RCEM operating points and corresponding conditions at TDC; diesel pilot mixture dwell at these operation points for $m_\mathrm{P} = 3\,\mathrm{mg}$, $p_\mathrm{inj,P} = 2000\,\mathrm{bar}$ and $t_\mathrm{inj,P} = 0.85\,\mathrm{ms}$.

OP number	p_0 [bar(a)]	T_0 [K]	p_TDC [bar(a)]	T_TDC [K]	ϵ_eff [-]	Δt_dwell [ms]
OP1	2.2	296 ± 1.5	75 ± 1	780 ± 3	12.9	$+0.25$
OP2	2.2	296 ± 1.5	88 ± 1	820 ± 4	14.6	-0.1
OP3	2.0	296 ± 1.5	100 ± 1.5	865 ± 6	17.2	-0.35
OP4	2.0	296 ± 1.5	125 ± 1.5	920 ± 7	20.5	-0.5

delay if the mixture dwell is negative. In case of a positive mixture dwell, a slight reduction of the ignition delay and thus also the mixture dwell was observed when doubling the injection pressure and the amount of pilot fuel.

The diesel pilot mixture dwell in the dual-fuel experiments is listed in the last column of Tab. 5.1. While the operating point with the lowest compression ratio (OP1) shows a positive mixture dwell, it is reduced slightly below zero at OP2. A clearly negative mixture dwell is obtained at OP3. The fourth operating point (OP4) is set to the maximum compression ratio achievable with the combustion chamber geometry designed for these experiments. It represents the conditions in modern diesel engines with a high compression ratio.

5.3 Influence of Gas Injection on Pilot Fuel Ignition

The influence of the interaction between the pilot and the natural gas jet on pilot ignition is investigated at the four operating points introduced in the preceding section. The spatial interaction is governed by the geometric arrangement of the jets relative to each other. In internal combustion engines, the arrangement options are severely restricted by the available space. The injector is usually located centrally between the valves in a four-stroke engine with two inlet and two outlet valves. Furthermore, design considerations support the use of a single injector for both fuels. Such an integrated injector placed centrally in the combustion chamber implies two closely located sets of nozzle bores, and the geometric arrangement of the fuel jets can therefore mainly be altered by changing the angle α between the jet axes. At the RCEM, the plane of closest interaction between the jets is designed perpendicular to the optical access, and the angle α is adjusted by rotating the natural gas injector (cf. Fig. 3.3). A positive angle is defined to correspond to pair of jets with diverging axes.

Since the jets propagate over time, the interaction depends not only on the geometric arrangement but also on the relative injection timing between the two injections. In this work, the relative injection timing is characterized by the time shift Δt_{SOI} of the natural gas SOI relative to the fixed pilot SOI.

In the case of a positive Δt_{SOI}, the diesel jet can freely penetrate or even ignite since the natural gas injection is started after the pilot injection. In contrast, the gas jet can premix to a certain degree before it is ignited by the pilot if a negative Δt_{SOI} is selected. The interaction between the propagating jets can therefore not be studied independent from the degree of natural gas premixing.

Two-dimensional contour plots of the α-Δt_{SOI} parameter space are repeatedly shown in this work and referenced as interaction maps. They are used to show how a selected quantity is affected by the jet interaction. An example of this plot type of can be found in Fig. 5.3.

5.3.1 Ignition Limits and Ignition Delay

Figure 5.3 shows the jet interaction maps for OP1 and OP4 with the color code representing the pilot ignition delay $\tau_{\mathrm{ign,P}}$. All the tested combinations were repeated tree times and the ones with successful ignition are marked by black dots. Even though this low number of repetitions for a single configuration is not sufficient to identify an exact statistical average, the significance of the results can be shown to be high. This is proven by a low variance in the region with undisturbed pilot ignition (dark blue contour with lowest $\tau_{\mathrm{ign,P}}$), which includes more than 70 measurements at OP1 and more than 100 measurements at OP4. Furthermore, the low variance of pressure and temperature at TDC (p_{TDC}, T_{TDC}) listed in Tab. 5.1 indicates the high repeatability of the combustion chamber conditions in the RCEM. Figure 5.1 can be used to show that the low variance in experimental conditions translates into a high repeatability with respect to the pilot ignition delay.

The low compression ratio at OP1 leads to failed ignition when combining negative angles with negative gas injection timings. In this region of maximum interference in the interaction map, both injections overlap in time and converging jets axes cause the pilot mixture formation to be strongly affected by the gas jet before ignition can take place. On the other hand, any combination of α and Δt_{SOI} with only low interaction either due to early pilot injection ($\Delta t_{\mathrm{SOI}} > 0$) or due to a strongly diverging jet arrangement ($\alpha > 20°$) shows the short ignition delays of undisturbed pilot

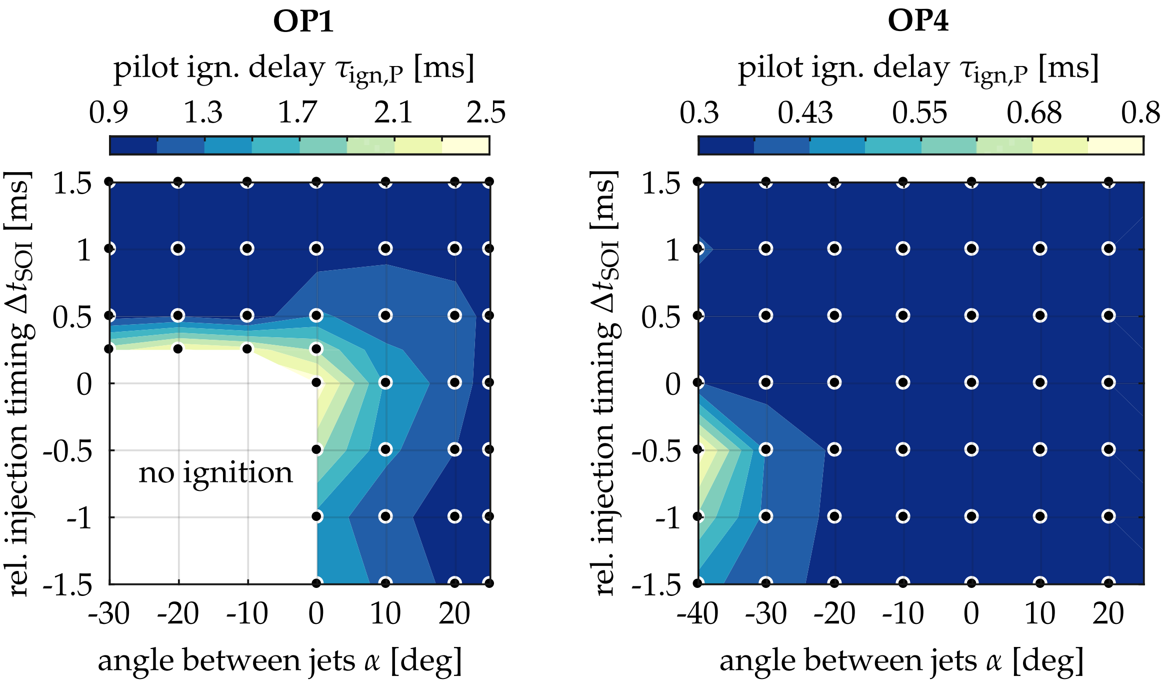

Figure 5.3: Jet interaction map showing the pilot ignition delay $\tau_{ign,P}$ at OP1 (785 K/75 bar) and OP4 (920 K/125 bar).

ignition[1]. When approaching the region of failing ignition, the pilot mixture formation is increasingly affected by the natural gas jet. This leads to a steep increase in ignition delay before misfiring is observed. The circular shape of the contour lines around the point of simultaneous injection and parallel arrangement can be explained by the mixture distribution of the natural gas jet during the injector opening phase, when the jet cone angle is large and the quasi-stationary air entrainment not yet established (see also Sec. 2.1.1 and Fig. 2.1). If the pilot jet interacts with the natural gas jet during early jet propagation, increased spatial interference and richer natural gas mixtures cause a stronger delay of ignition.

At the higher compression ratio of OP4 the pilot ignition delay is considerably lower than at OP1 (note the different scaling of the two plots) and the region with failed ignition disappears. The pilot can ignite rather undisturbed at most combinations of α and Δt_{SOI} shown in the interaction map. However, a small region of longer ignition delay is still present at $\alpha < -20°$. Compared to OP1 this region is of similar shape but displaced to lower angular values.

[1] Angles α of more than approx. 30° show very unstable and late natural gas ignition due to weak jet interaction and are therefore not considered.

5.3.2 Pilot Lift-Off Criterion

If the cause of the increase in ignition delay with more intense interaction can be identified, a criterion to avoid misfiring may be formulated. The effect can be observed in more detail with the left plot in Fig. 5.4, where the pilot ignition delay is plotted against the angle between the jets at a fixed relative injection timing of $\Delta t_{SOI}=-0.5\,\text{ms}$ for all four operating points. Starting from large angles at $\alpha=+30°$ and turning the jet axes towards each other, the ignition delay increases and stability is reduced before pilot auto-ignition fails. In general, ignition is found to be more stable for a negative pilot mixture dwell, when the ignition delay is shorter than the injection duration.

The reason for this behavior is analyzed by taking a closer look at the flame position. The images in Fig. 5.4 were recorded at the time of pilot ignition, and each operating point is represented by the minimum angle at which ignition is sustained. By including the virtual jet cones of the pilot (18°) and natural gas jet (24°), two parameters can be obtained: the lift-off lenght of the pilot flame $x_{\mathrm{lift,P}}$ as the minimum distance between pilot injector tip and flame within the diesel fuel jet cone, and the maximum free path length $x_{\mathrm{max,P}}$ as the maximum distance the diesel jet can penetrate before intersecting with the gas cone. Both parameters are plotted in the diagram on the right.

In the case of undisturbed and fast ignition at large angles α the pilot ignites closest to the injector. When the jet axes are tilted towards each other, the strong gas jet entrainment increasingly influences the diesel pilot mixture field. This shifts the point of ignition further downstream and increases the ignition delay. The longer the ignition delay at a certain operating point in general, the further the pilot penetrates prior to ignition. Therefore, the gas entrainment acts on the pilot over a longer distance and time at OP2 and especially OP1. At the time of ignition, the pilot injector is already closed for those two operating points, and the pilot spray is almost completely entrained into the gas jet.

Ignition never occurs in the gas jet downstream of the region of interaction with the pilot jet, where a mixture of both fuels and air is present. For the shown cases close to misfiring auto-ignition is found to happen in close

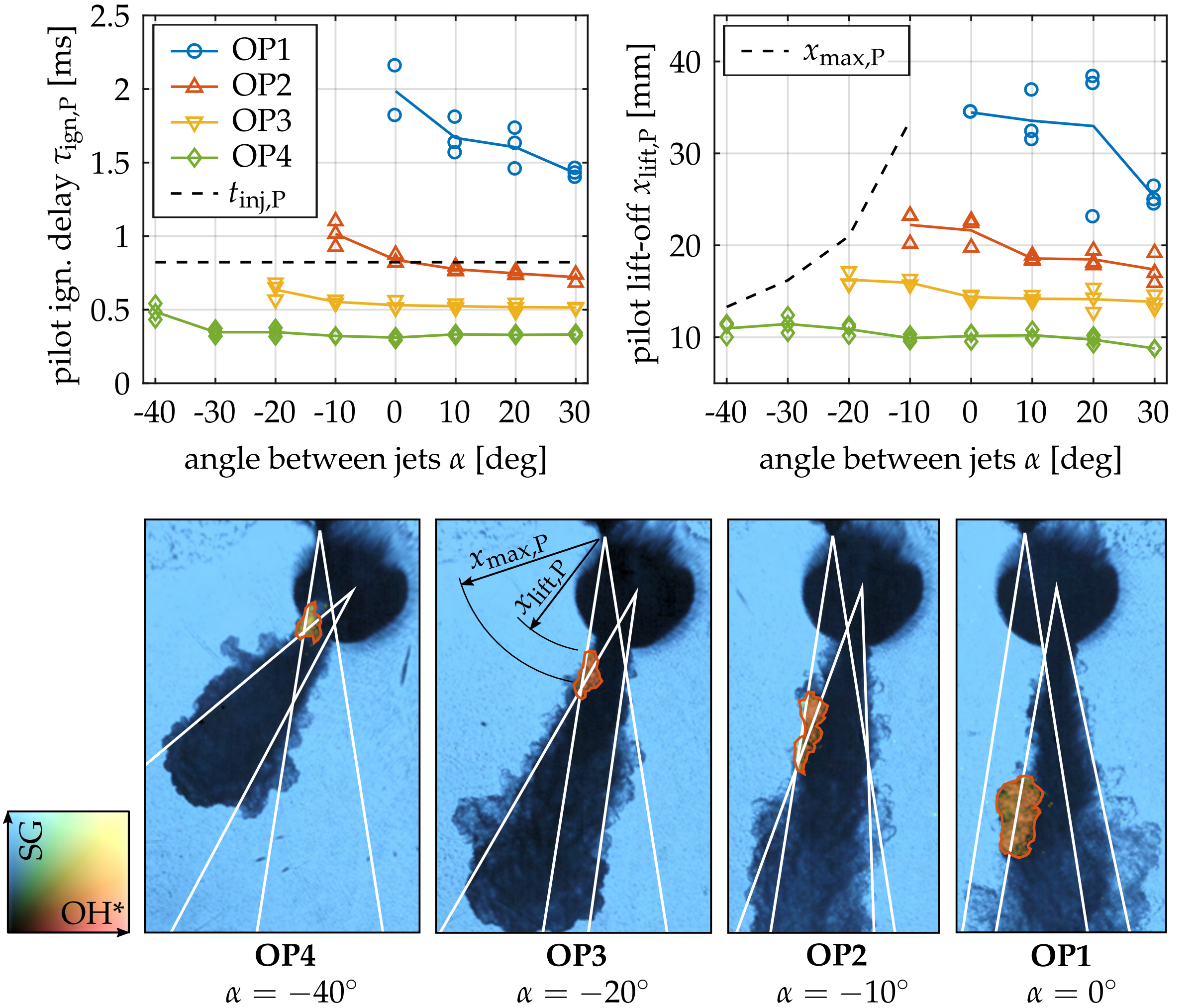

Figure 5.4: Pilot ignition delay (top left) and pilot lift-off (top right) at different interaction angles with relative gas injection timing of $\Delta t_{SOI} = -0.5\,\text{ms}$; bottom: images recorded at the time of pilot ignition for the minimum angle at each operating point.

proximity to the maximum free path length of the pilot $x_{max,P}$, as shown in the images in Fig. 5.4. When the jets are gradually turned towards each other at any single operating point, $x_{lift,P}$ slightly increases while $x_{max,P}$ drops. Ignition is inhibited as soon as the free path length falls below the pilot lift-off length.

Strong jet interaction prior to diesel fuel ignition is summarized to negatively influence auto-ignition if the pilot fuel is disturbed by the gas jet before it can propagate to the ignition lift off length. This behavior can be attributed to various effects occurring simultaneously. The gas jet violently influences diesel mixture formation by rapid dilution with natural gas and isolation from air entrainment. Furthermore, the temperature is locally reduced by the cold gas jet which slows down the ignition kinetics. Several authors additionally refer to a direct kinetic impact by altered reaction paths [1, 90]. Choosing the free path length to be considerably larger than the pilot lift-off is found to be a good criterion for stable pilot ignition within the investigated range.

6 Freely Propagating Natural Gas Jet

This chapter is focused on the characterization of a pilot-ignited, freely propagating natural gas jet. In a chronological manner, natural gas jet ignition and flame development are investigated first before the overall fuel oxidation process is examined in detail. By combining the analysis of heat release rates, simultaneous SG/OH* images and numerical modeling results, an in-depth understanding is generated.

6.1 Gas Jet Ignition by the Diesel Pilot

The process of natural gas jet ignition by the entrained diesel pilot combustion products is treated in this section.[1] At first the influence of jet interaction on the delay between pilot fuel ignition and onset of natural gas combustion is investigated. Then, the ignition location of the gas jet is analyzed based on the findings on pilot ignition described in Sec. 5.3. The section concludes with an evaluation of the pilot fuel jet's influence on the initial flame propagation in the natural gas jet.

6.1.1 Natural Gas Ignition Delay

The natural gas ignition delay $\tau_{ign,NG}$ was introduced in Sec. 4.1.4 as the time delay between successful pilot ignition and natural gas jet ignition. This ignition delay should not be confused with the chemical combustion induction time of the fuel. Since the natural gas jet does not auto-ignite,

[1]As shown in Ch. 5, the diesel pilot was found to ignite either unaffected by the gas jet or in the outermost part of the gas jet shear layer. Even though the jets may interact to form a ternary mixture in the gas jet prior to ignition, it is the products from the auto-ignited pilot fuel that establish the initial reaction zone in the gas jet.

$\tau_{ign,NG}$ is used to assess the quality of natural gas jet ignition by the diesel pilot instead.

The two interaction maps for OP1 and OP4 in Fig. 6.1 show contours of the natural gas ignition delay. It is reasonable to distinguish between regions with positive and negative relative injection timings. If Δt_{SOI} is positive, the pilot fuel injection is started before the natural gas injection. An increase of the relative injection timing therefore directly causes $\tau_{ign,NG}$ to increase as well. The arc-shaped contour lines in this region show the shortest natural gas ignition delay at an angle α of about -10°. At this angle the natural gas jet is directed towards the diesel combustion products and natural gas jet ignition is therefore the fastest.

At negative relative injection timings Δt_{SOI}, the shape of the contour lines at both operating conditions is very similar to the ones of the pilot ignition delay at OP1 (cf. Fig. 5.3). But in contrast to pilot ignition, a strong interaction between the jets is found to result in a faster natural gas ignition. There even seems to be a direct trade-off between stable pilot ignition and fast natural gas ignition at OP1. Since the region suffering from misfiring vanishes when increasing the compression ratio, a wide region with constantly low $\tau_{ign,NG}$ exists at OP4. Thus the trade-off observed at OP1 disappears and undisturbed pilot ignition combined with fast natural gas ignition is possible between $-20° < \alpha < 0°$.

Surprisingly, $\tau_{ign,NG}$ turns out to be longer at OP4 compared to OP1, despite the higher pressure and temperature in the combustion chamber and independent of the interaction (note the same scaling of the contour levels in both plots). At $\Delta t_{SOI} > 0$, this is a direct consequence of the faster pilot ignition and therefore longer offset until the NG injection is started. The reason for slower NG ignition at negative relative injection timings at OP4 becomes clear from the image sequences in Fig. 6.1, which illustrate injection at $\alpha = 10°$ and $\Delta t_{SOI} = -0.5\,\mathrm{ms}$ (marked with ☆ in the contour plots). The diesel pilot ignites already 0.35 ms after SOI at OP4. Natural gas ignition is detected by the first significant heat release about 0.7 ms later and the optical recordings confirm that the reaction zone has reached part of the natural gas jet at that time. At the same time relative to SOI the diesel spray at OP1 has not yet ignited and forms a combined mixture zone with the natural gas jet. This results in a very short natural gas ignition delay of

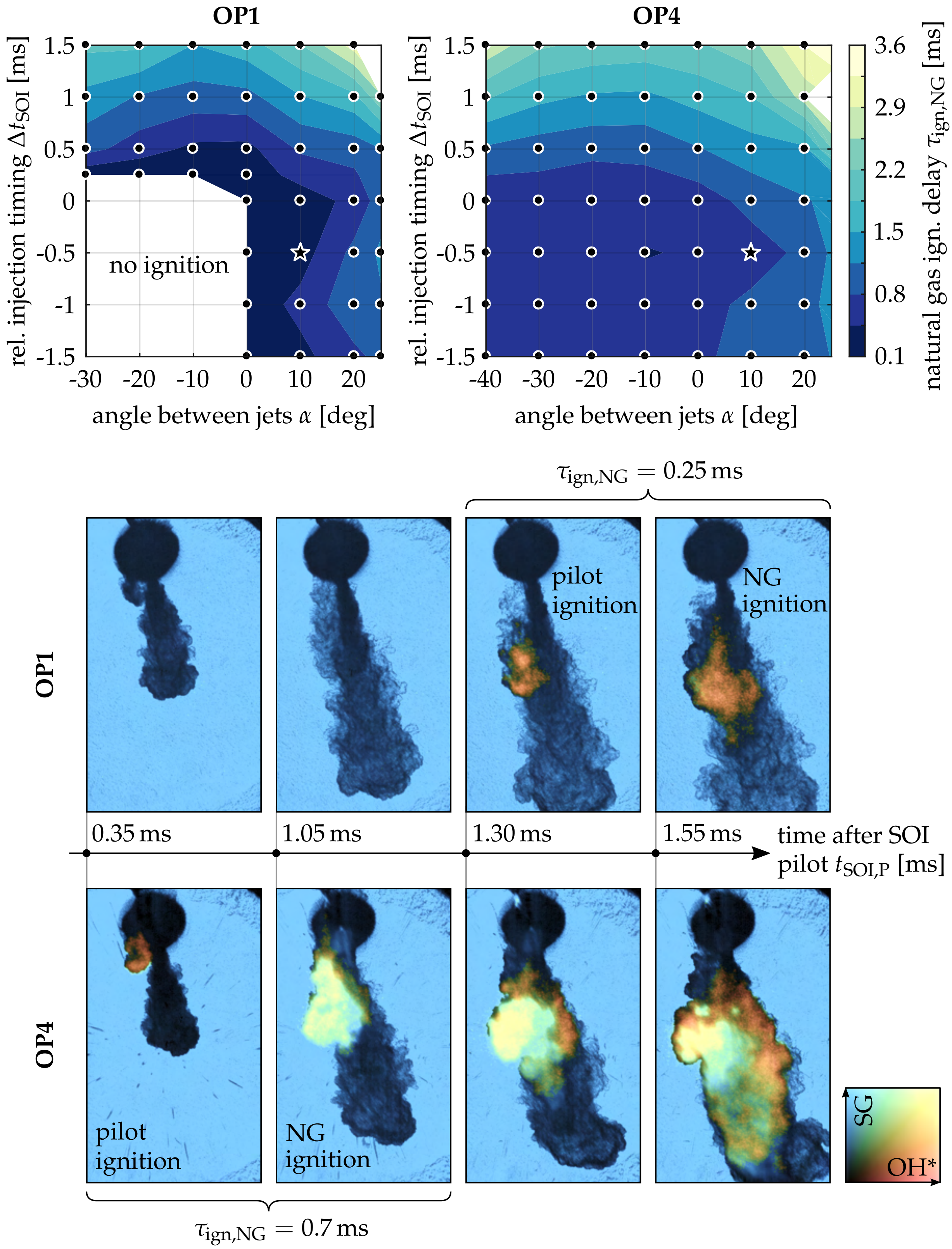

Figure 6.1: Top: interaction maps showing the natural gas ignition delay $\tau_{ign,NG}$ at OP1 and OP4; Bottom: image sequences corresponding to the point marked by (☆) in the interaction maps.

only 0.25 ms at OP1 once the pilot ignites at $t_{\mathrm{SOI,P}} = 1.3\,\mathrm{ms}$. Even though the pilot jet interacts with the natural gas jet directly after ignition close to the NG nozzle exit at OP4, it needs to be entrained a certain distance downstream before NG jet ignition occurs. The downstream extent of the burning region in the gas jet at the time of natural gas ignition is therefore surprisingly similar for both operating points, while the lift-off is shorter at OP4.

6.1.2 Ignition Location

The image sequences in Fig. 6.1 show that the ignition location may directly influence initial flame development. This raises the question whether, when using an integrated central HPDF injector, the natural gas jet ignition location itself can be changed by adjusting the jet interaction. Since the more premixed zones can be found at the jet tip while injection is still ongoing, ignition further downstream may be desirable. Avoiding ignition close to the injector orifice potentially reduces soot formation since the amount of air entrained in this part of the jet governs the equivalence ratio of the reaction zone at the lift-off position.

In the previous chapter, pilot ignition was found to occur in those parts of the diesel jet that are not or only slightly affected by the natural gas injection. This finding can be used to identify a theoretical range for the natural gas jet ignition location. The SG/OH* image in Figure 6.2 shows the region for free pilot ignition, limited by the two jet cones and the pilot lift-off length $x_{\mathrm{lift,P}}$. The gas jet interacts with the ignited pilot in between the downstream distances $x_{\mathrm{min,NG}}$ and $x_{\mathrm{max,NG}}$. This theoretical range for the natural gas jet ignition location is shaded in the left diagram in Fig. 6.2 according to the respective operating conditions.

The flame position indicated by OH* chemiluminescence is highlighted in the SG/OH* image in Fig. 6.2 with a red line. Since the tip of the flame propagates rapidly, the downstream extent at the time of NG ignition cannot be evaluated in a meaningful manner. However, the lift-off length $x_{\mathrm{lift,NG}}$ within the NG jet cone is suitable to describe the downstream position of the flame at that time.

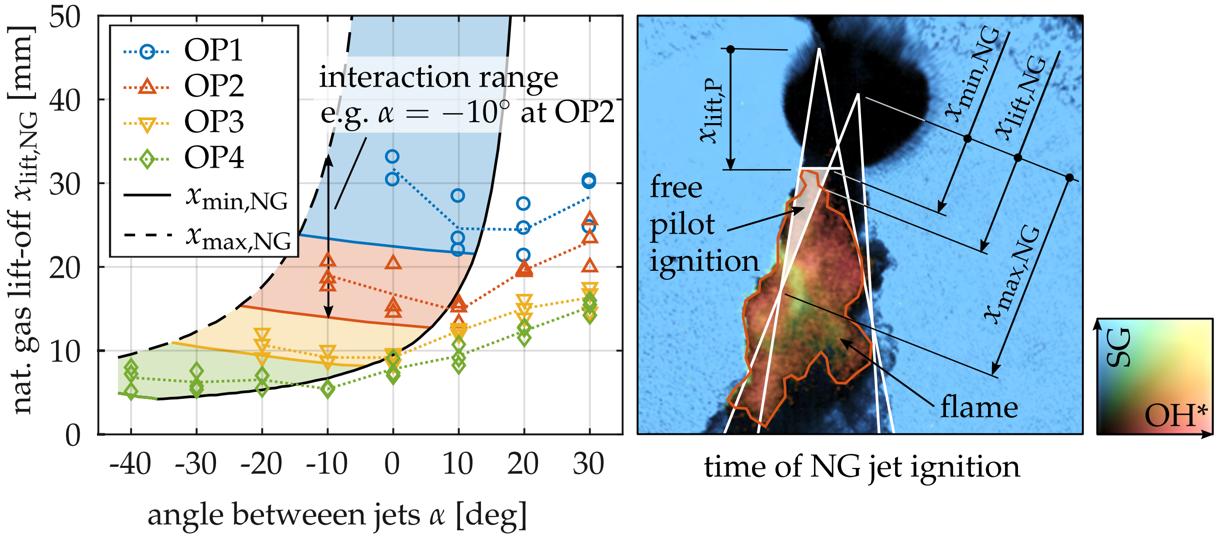

Figure 6.2: Right: region of free pilot ignition limited by the virtual jet cones and the pilot liftoff $x_{lift,P}$, theoretical range of interaction with the natural gas jet ($x_{min,NG}$, $x_{max,NG}$) and actual natural gas lift-off $x_{lift,NG}$; Left: comparison of the natural gas lift-off with the range of interaction between the region of free pilot ignition and the gas jet cone for all operating points at $\Delta t_{SOI} = -0.5$ ms.

The diagram in Fig. 6.2 on the left compares this actual natural gas lift-off length $x_{lift,NG}$ to the range of interaction with the region of free pilot ignition for all operating points at $\Delta t_{SOI} = -0.5$ ms. Since the pilot lift-off length $x_{lift,P}$ depends on the operating conditions, $x_{min,NG}$ does as well. For a strong geometrical overlap (small α) natural gas ignition is found to occur close to the individual $x_{min,NG}$. A reduction of the angle α slightly increases the lift-off before misfiring is observed.

Increasing the angle α between the jets causes the point of first interaction $x_{min,NG}$ to rapidly shift downstream. Beyond approximately 20° the natural gas and diesel pilot jet cones do not intersect any more. However, $x_{lift,NG}$ is found to only slightly increase and ignition is observed far upstream of the theoretically determined point of first interaction with the region of free pilot ignition. As a consequence, natural gas ignition is successful up to $\alpha = 30°$ at any operating point. This stable gas jet ignition with diverging jet axes is caused by the strong entrainment of the natural gas jet, as the upper image sequence in Fig. 6.3 proves. The sequence illustrates natural gas jet ignition at $\alpha = 30°$ and $\Delta t_{SOI} = -0.5$ ms at OP4 (cf. Fig. 6.2). Prior to natural gas jet ignition the strong entrainment causes a bulge in the pilot jet contour on the side facing the gas jet. This results in a weak interaction sufficient to ignite the gas jet close to the pilot lift-off location even though there is a considerable gap between the jet cones.

All these considerations do not address any possible influence of the injection timing on the ignition location, since all presented data was obtained at a fixed timing of $\Delta t_{SOI} = -0.5\,\mathrm{ms}$. When injected very early, the pilot jet can penetrate far into the combustion chamber before gas injection is started. This may allow to ignite the gas jet at its tip in a location further downstream. The course of natural gas jet ignition with $\Delta t_{SOI} = +1.5\,\mathrm{ms}$ is shown in the lower image sequence in Fig. 6.3 for $\alpha = -10^\circ$ at OP4. Since penetration of the non-reacting natural gas jet is hard to observe, the natural gas jet tip is additionally marked by a green line.

At the start of NG injection, the pilot jet extends far into the combustion chamber. Soot luminescence has already vanished and burnout is about to be completed. Nevertheless, interaction of the gas jet with the diesel

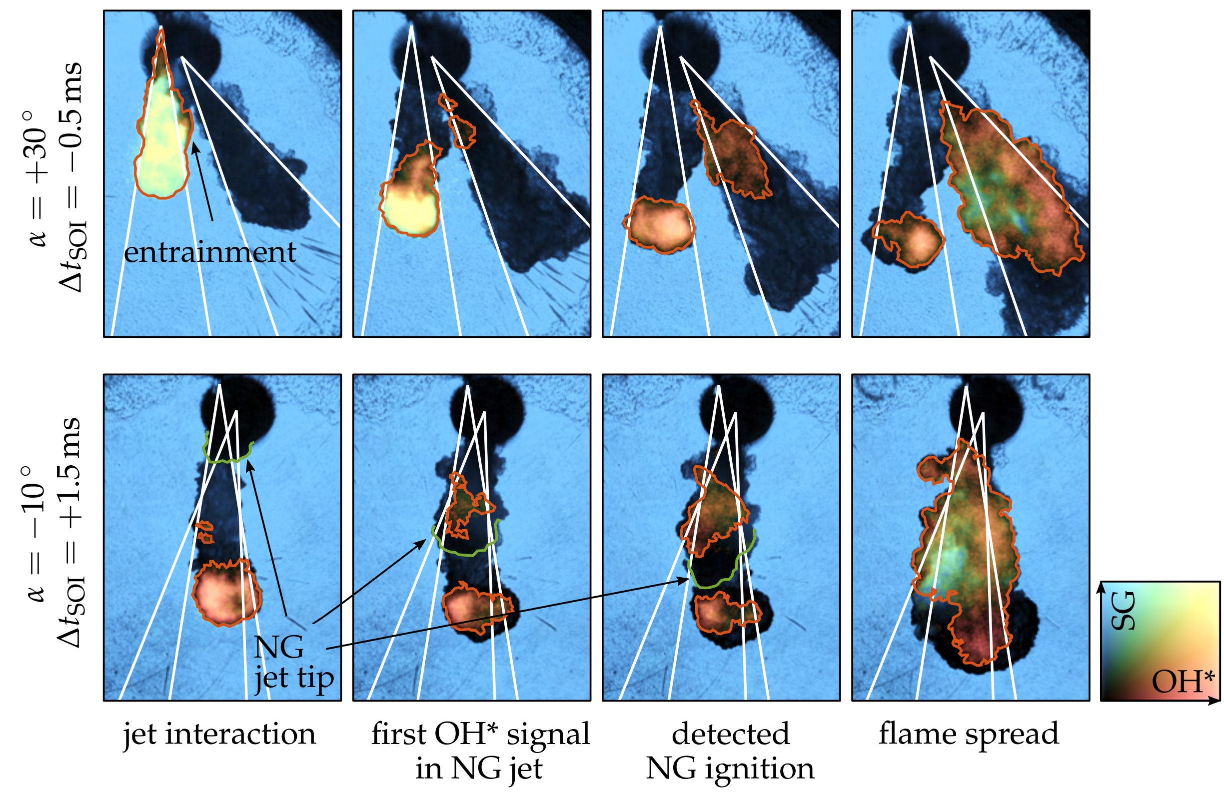

Figure 6.3: Image sequences showing NG ignition with strongly diverging arrangement of the jet axes (top) and with very early pilot injection (bottom) at OP4.

products in the upstream region is sufficient to ignite the gas jet at an early stage close to its tip. Initially, the natural gas lift-off length is slightly increased. Later at the time when natural gas ignition is detected, the extent of the flame is very similar for the two sequences shown in Fig. 6.3 – even though injection timing and jet arrangement are very different. These observations show that the ignition location cannot be significantly influenced by the relative injection timing either.

It is therefore concluded that the jet interaction has only minor influence on the natural gas jet ignition location when using an integrated HPDF injector with very closely located nozzles for both fuels. The jet entrainment causes natural gas ignition to occur very close to the pilot lift off location, even with strongly diverging orientation of the jet axes. Very early pilot injection can not shift the ignition location downstream either, since interaction with the burnt diesel products close to the injector is sufficient to ignite the natural gas jet.

6.1.3 Initial Flame Development

After natural gas jet ignition, the flame propagates to the partially-premixed zones and is simultaneously carried towards the jet tip by the high flow velocity. This phase of the combustion process is accompanied by a steep increase in reaction rate and is not attributable to the ignition phase any more. However, the initial flame development may be affected by the interaction of the two fuel jets prior to or during the ignition phase.

In addition to the natural gas lift-off $x_{\mathrm{lift,NG}}$, the jet penetration $x_{\mathrm{pen,NG}}$ and the position of the leading flame tip $x_{\mathrm{tip,NG}}$ are evaluated in Fig. 6.4 for a case with strong geometrical overlap ($\alpha = -30°$) and one with diverging arrangement of the jet axes ($\alpha = +20°$). The shown curves were averaged from three repeated measurements. Again the gas injection starts shortly before the pilot injection ($\Delta t_{\mathrm{SOI}} = -0.5\,\mathrm{ms}$), meaning that there is a strong temporal overlap. The presented images show the first interaction of the gas jet cone with the pilot flame, natural gas ignition and the time when the flame covers the whole jet.

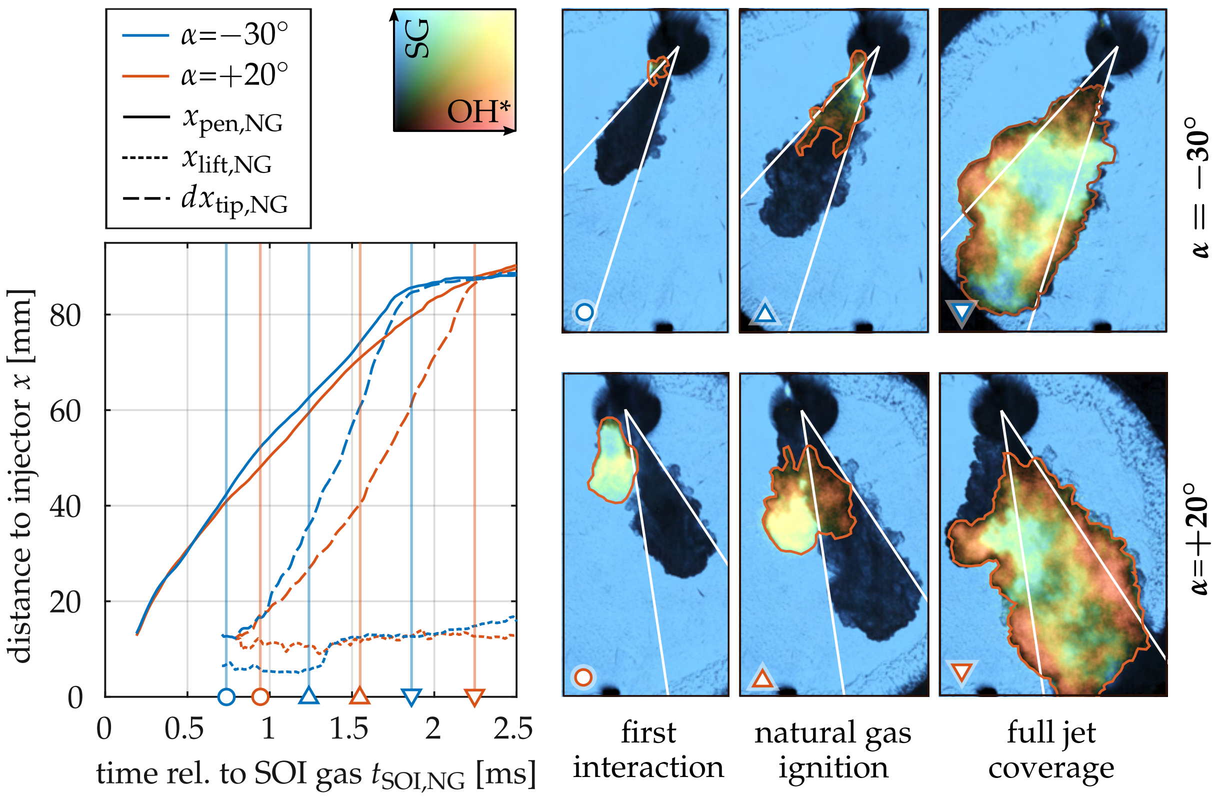

Figure 6.4: Left: Temporal evolution of the natural gas jet tip penetration $x_{\mathrm{pen,NG}}$, natural gas lift-off $x_{\mathrm{lift,NG}}$ and position of the leading flame tip $x_{\mathrm{tip,NG}}$ for strong geometrical overlap ($\alpha = -30°$) and for strongly diverging jet axes ($\alpha = +20°$) with $\Delta t_{\mathrm{SOI}} = -0.5$ ms at OP4; Right: image sequences showing first interaction with the pilot flame, natural gas ignition and the time of full NG jet coverage.

Even though the pilot jet interacts very early with the gas jet at an angle of $\alpha = -30°$, it takes some time until the flame starts to propagate downstream. If the jet axes diverge at $\alpha = +20°$ on the other hand, interaction is weaker, occurs later and is observed slightly further downstream. As a consequence, the location of the leading flame tip $x_{\mathrm{tip,NG}}$ is identical at about 0.9 ms after SOI. After this point the flame spreads notably faster with a stronger geometrical overlap and the faster flame propagation is preserved until full jet coverage. Since the combustion chamber conditions are the same in both cases, the faster flame propagation must be caused by the high reactivity of the unburned pilot fuel entrained by the NG jet. In total, the time difference until the whole jet is covered by the flame is about 0.4 ms. But since the start of natural gas combustion is only detected when $x_{\mathrm{tip,NG}} \approx 40$ mm, most of the difference in initial flame propagation is observed during the ignition phase. The remaining offset between natural gas ignition and full jet coverage caused by jet arrangement is therefore only about 0.1 ms.

Since the natural gas flame is anchored at the pilot flame, strong geometrical overlap of the jets at $\alpha = -30°$ causes an initially reduced natural gas lift-off length $x_{\mathrm{lift,NG}}$. After the end of pilot injection ($t_{\mathrm{SOI,NG}} =$ 1.35 ms) the lift-off increases sharply. Since both cases show the same lift-off length after pilot injection is over, this value is considered the lift-off length of the stationary natural gas jet.

6.2 Combustion Characterization

The combustion process of the natural gas jet is first characterized based on the heat release rates. This characterization includes the influence of the combustion chamber conditions as well as the influence of NG injection pressure. The combined SG/OH* images allow to attribute the observed heat release rate characteristics to local phenomena and to assess the soot formation process. In the last section, the experimental observations are complemented by an analysis of the transient mixture formation and combustion progress using results from numerical simulations. The characterization is the basis for a generalized phenomenological description of diesel-piloted natural gas jet combustion with closely located nozzle orifices in Ch. 8.

6.2.1 Heat Release Rate Similarity

The reaction progress of the pilot-ignited natural gas jets is strongly governed by the degree of premixing. Since this degree of premixing itself directly correlates with the time available for mixing, it is evident to assume a direct influence of the offset between the natural gas SOI and ignition on the temporal evolution of heat release. The definition of this natural gas ignition offset $\Delta t_{\mathrm{ign,NG}}$ was already introduced in section 4.1.4.

The findings on pilot and natural gas ignition support such a direct correlation between the degree of premixing and the resulting heat release.

Two natural jets with the same degree of premixing can only show a different heat release if the evolution of the reaction zone is different. This in turn implies that either the jets have to be ignited at different locations or that flame propagation from the same ignition location has to be affected by the interaction with the pilot. As soon as the flame covers the entire jet, a quasi-steady state is reached in any case, where the heat release correlates directly with the injection-driven mixing rate. The investigation of the natural gas ignition process in Sec. 6.1 has shown that both the ignition location as well as the flame propagation after natural gas jet ignition are only marginally affected by the jet interaction. Therefore, the interaction with the pilot jet is expected to have a minor influence on the evolution of heat release.

In order to verify a direct scalability with the degree of premixing, the correlation between specific properties of the heat release rate and the natural gas ignition offset $\Delta t_{\mathrm{ign,NG}}$ is examined first. Figure 6.5 shows the peak and mean heat release rates as well as the corresponding time scales plotted against $\Delta t_{\mathrm{ign,NG}}$ for all tested points at OP1, independent of jet orientation and relative injection timing. Ignoring the color grouping at first, a distinct correlation is visible for all four parameters. The clearest correlation can be found for the peak offset Δt_{peak}. At very low $\Delta t_{\mathrm{ign,NG}}$ some measurement points seem to disobey the correlation. The reason for this deviation is that the sharp peak attributable to premixed combustion disappears when the natural gas jet is ignited very early. When the peak heat release is delayed by late NG ignition, it increases in magnitude. If the peak offset is longer than the injection duration (2.7 ms at $\Delta t_{\mathrm{ign,NG}} > 1.9$ ms, further premixing causes the overall mixture to become lean very fast and the maximum heat release rate drops again. Since the combustion duration is reduced by late natural gas ignition, the mean heat release rate increases monotonically. For very late onset of combustion the scatter in mean heat release becomes larger due to a stronger sensitivity to small variations in combustion duration. If the natural gas jet is ignited after EOI at $\Delta t_{\mathrm{ign,NG}} > 2.7$ ms, the combustion duration is not reduced further. This is most probably caused by the fast decay of jet flow velocity and therefore a lower flame propagation after EOI.

Now the heat release rates can be grouped by the NG ignition offset as the proposed similarity parameter, which is indicated by the colors in Fig. 6.5

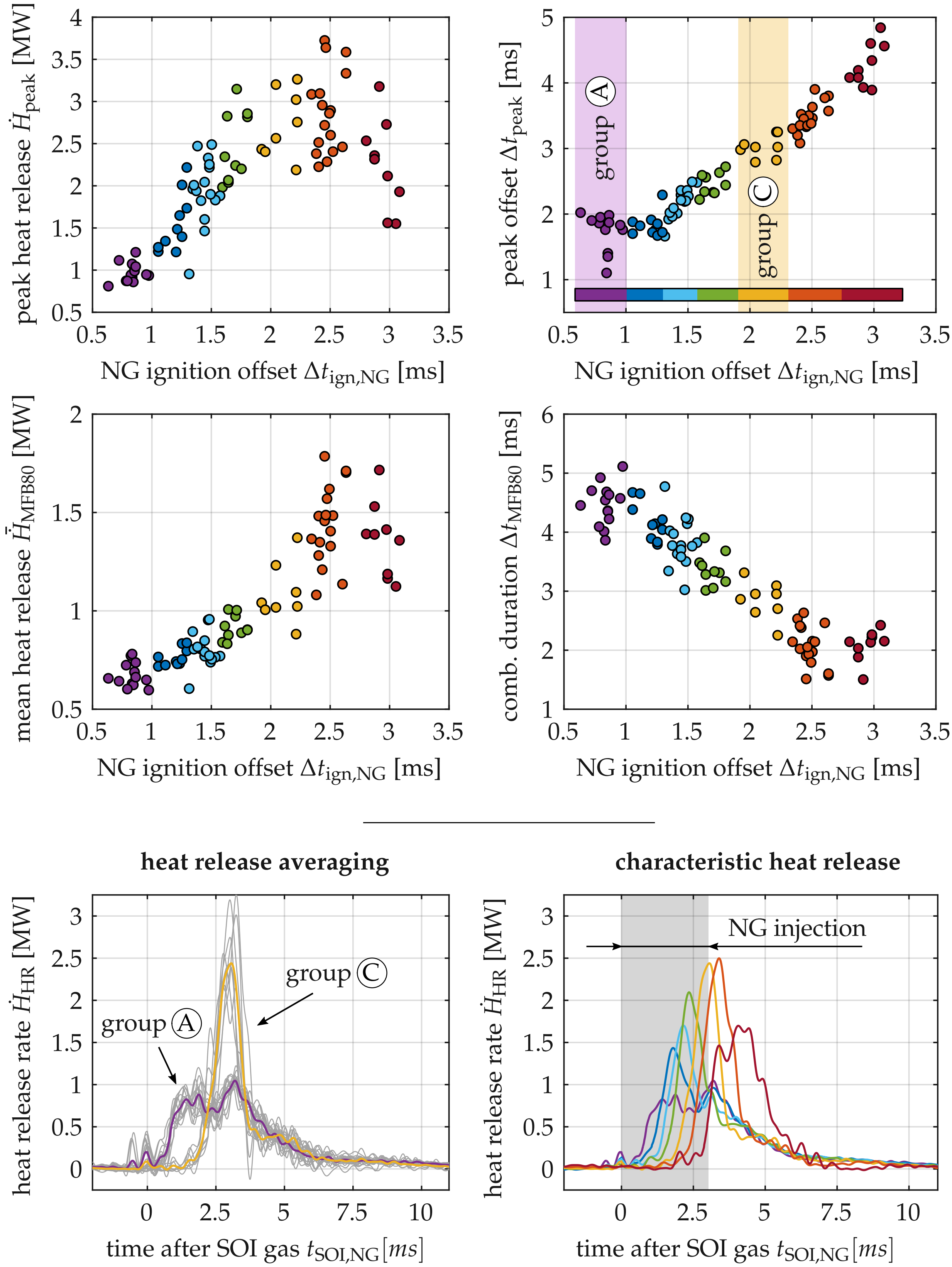

Figure 6.5: Characterization of the heat release at OP1 by the natural gas ignition offset $\Delta t_{ign,NG}$ using four specific properties of the heat release (top); average heat release rates from all measurements grouped by $\Delta t_{ign,NG}$ (bottom).

for seven groups across the whole range. The bottom left diagram displays all measurements with the fastest ignition in group Ⓐ and those with a strong premixing in group Ⓒ in light gray, along with the average from both groups. The good agreement independent of spatial and temporal interaction once more confirms the scaling assumption. The bottom right plot shows how the heat release rate changes when altering the time of gas jet ignition only. These curves were obtained by calculating the average within each group as shown and explained for the groups Ⓐ and Ⓒ.

Although the heat release scales with $\Delta t_{\text{ign,NG}}$ independent of the interaction, only a very specific shape of heat release can be achieved with a certain geometrical arrangement α and associated injection timing Δt_{SOI}. The interaction maps in Fig. 6.6 show contours of the natural gas ignition offset. The left diagram for OP1 indicates that only low degrees of premixing can be achieved with crossing jet axes due to the region with failing ignition. Since an angle of $\alpha = 0°$ close to misfiring is to be avoided, the jets must be able to freely propagate at a positive angle between their axes to allow for stronger premixing. However, this arrangement in turn implies that fast NG ignition for minimum premixing is not possible. Since the misfiring region disappears at higher compression ratios, the heat release rates associated with stronger premixing can also be achieved with crossing jet axes at OP4.

To proof the shape of heat release to be only governed by $\Delta t_{\text{ign,NG}}$ independent of jet interaction at OP4 as well, the same heat release rate characterization performed for OP1 in Fig. 6.5 may be repeated. Due to corrupted pressure measurement data at OP4, the data base is not large enough to perform the same characterization for this operating point.[2] However, the arguments presented at the beginning of this section justify the assumption that self-similarity independent of the jet interaction can be expected at OP4 as well.

Even if self-similarity is presumed at OP4 as well, two points with the same $\Delta t_{\text{ign,NG}}$ at OP1 and OP4 do not have to show the same heat release since

[2]After changing the volume reduction for the high compression ratio at OP4, the pressure transducer ended up partially covered (cf. Fig. 3.3). This caused oscillations on the pressure signal that did not allow for an accurate heat release rate calculation. Only a fraction of the parameter variation was repeated with a correctly mounted sensor. A comparison showed that accurate detection of the natural gas ignition was not affected.

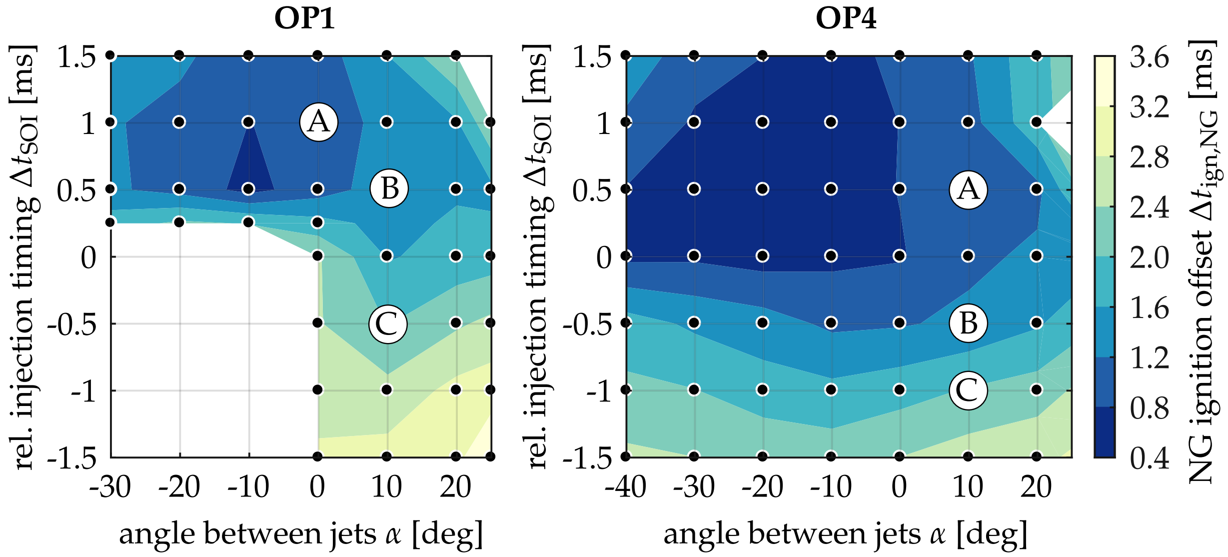

Figure 6.6: Interaction maps showing the natural gas ignition offset $\Delta t_{ign,NG}$ for OP1 and OP4; the labelling of the marked cases refers to the grouping in Fig. 6.5 while the colormap and levels are different.

temperature and pressure in the combustion chamber influence e.g. flame velocity, burning limits or burnout chemistry. To show the effect of altered operating conditions on the heat release rates, only the measurements with $\alpha = 10°$ at OP4 were repeated. The heat release rates of the points marked in Fig. 6.6 are presented in Fig. 6.7 and were selected to cover low Ⓐ, medium Ⓑ and high Ⓒ degree of premixing. Furthermore, the natural gas ignition offset of those three points lies within the corresponding groups in Fig. 6.5. Again, the shown curves are the average from three repeated measurements. For a better understanding of the differences in combustion progress, Fig. 6.7 includes the combined SG/OH* image sequences for medium premixing Ⓑ at selected times. The sequences are synchronized relative to the natural gas SOI.

Independent of the degree of premixing, the heat release rates in Fig. 6.7 show a stronger peak at OP4 during premixed combustion. This behavior may be explained by a higher flame speed. However, the images reveal that the peak in heat release rate always occurs as soon as the flame covers the whole gas jet. Due to the fact that at this time the injected gas mass is equal for both operating points and the overall fuel consumed is higher at OP4, the consumption of the rich parts within the center of the jet must be

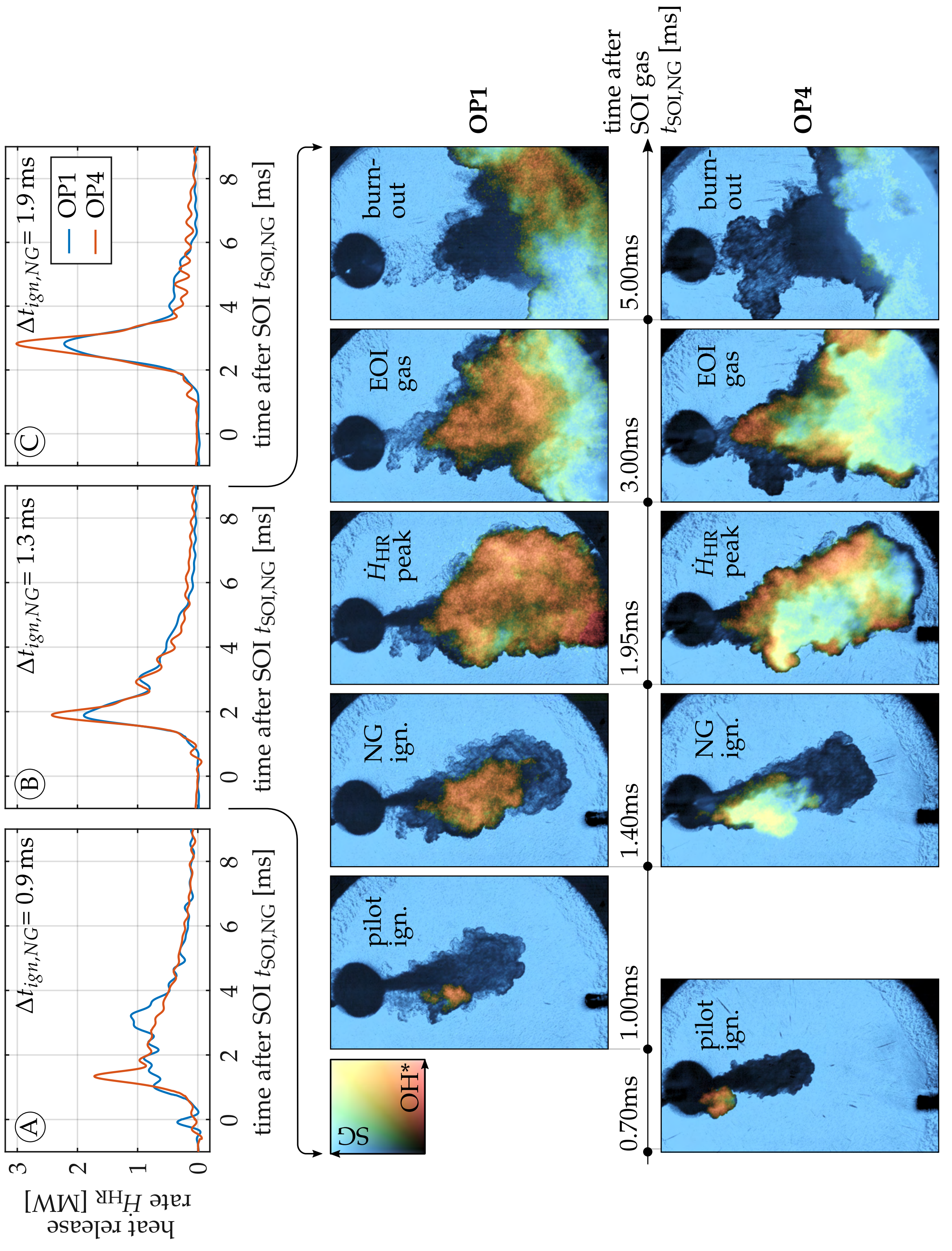

Figure 6.7: Comparison of heat release rates for low Ⓐ, medium Ⓑ and strong premixing Ⓒ at OP1 and OP4, jet arrangement and injection timing according to Fig. 6.6; image sequences for medium premixing Ⓑ at selected times relative to NG SOI (bottom).

the reason for the stronger peak. Wider burning limits are also indicated by the lift-off length, which is considerably shorter at OP4.

It is noticeable that after end of injection ($t_{SOI,NG} > 2.7\,\mathrm{ms}$) the heat release rates are higher at OP1. During this phase of combustion, strong entrainment rapidly reduces the equivalence ratio and increases fuel conversion. Since the more narrow burning limits have caused lower fuel consumption prior to EOI at OP1, the reaction rates during burnout are higher than at OP4. In particular, low premixing at OP1 shows a very high heat release rate after EOI. Here, a case with $\alpha = 0°$ and simultaneous injection had to be selected to achieve early ignition (see label A in Fig. 6.6). In this configuration the natural gas jet is directed towards the pilot fuel reaction zone (similar to the lower sequence in Fig. 6.3). As a consequence, the missing lateral entrainment of burnt diesel products increases the flame lift-off and results in a lower fuel consumption during injection.

Already at first glance, the two cases exhibit very different soot luminosity. Both the diesel and natural gas combustion indicate stronger and earlier soot formation at the higher compression ratio of OP4. This will be discussed in detail in Sec. 6.2.3 along with the other factors that influence soot formation.

6.2.2 Injection Pressure Variation

In general, high natural gas injection pressures are necessary to inject the required amount of fuel into the compressed charge within the short time available, and thereby to achieve a short combustion duration and high engine efficiency. Enhanced mixture formation by a high injection pressure further reduces the combustion duration and improves burnout. Since a variation of the injection pressure affects the fuel injection rate and injection duration when the amount of fuel is kept constant, the injector orifice diameter has to be included into this discussion as well.

McTaggart-Cowan *et.al.* [61] varied the natural gas injection pressure in a single-cylinder conventional HPDF experiment between 210 and 300 bar. Combustion phasing – the mid-point of the integrated heat release relative to TDC – was kept constant by shifting both injections with respect to TDC without adjusting the relative timing between the injections. The injector equipment was not altered, causing the injection duration at a certain load to be affected by the injection pressure. Increasing the injection pressure at high load resulted in a substantial reduction of CO and PM emissions while engine-out NO_x was found to rise only slightly. The overall impact on the heat release rate was not reported but is assumed be low, since the gross indicated specific fuel consumption was found to be unaffected.

In 2015, the same group published the results of a study with natural gas injection pressure up to 600 bar [58]. The previously reported effect of the injection pressure on engine emissions was confirmed for the extended range, while the increase of the injection pressure from 280 to 600 bar improved thermal efficiency by 3 percentage points. The gain in thermal efficiency at high gas rail pressure was associated with an increase in combustion harshness and noise. Therefore, a different nozzle with reduced orifice diameter was introduced to limit the injection rate. Compared to the standard orifice, the smaller diameter allowed as fast combustion but lower peak heat release rates, and therefore earlier combustion phasing without exceeding peak cylinder pressure. PM emissions were shown to be unaffected by the reduced diameter and NO_x emissions even decreased. Accompanying CFD calculations indicated that the distribution of fuel among the equivalence ratios during injection is not significantly altered by increasing the injection pressure. This agrees with the theory of jet self-similarity stating that the amount of air entrained by the gas jet scales with the mass in the jet itself. However, the jet velocity increases with injection pressure, affecting air entrainment after EOI. The result are a faster oxidation of PM and CO during late diffusive burnout as well as higher NO formation rates.

Figure 6.8 presents the result of an injection pressure variation with the RCEM experimental setup. It was carried out to assess the effect of improved mixture formation with increased injection pressure on the heat release rates and flame luminosity, while keeping the injection duration constant. For three different nozzle orifice diameters the injection pressure was adapted so that the same amount of fuel is injected within 2.7 ms injection duration. In contrast to the studies by McTaggart-Cowan *et.al.* [58, 61], the pilot injection pressure did not have to be adjusted along with the NG injection pressure since the experimental setup allows to set

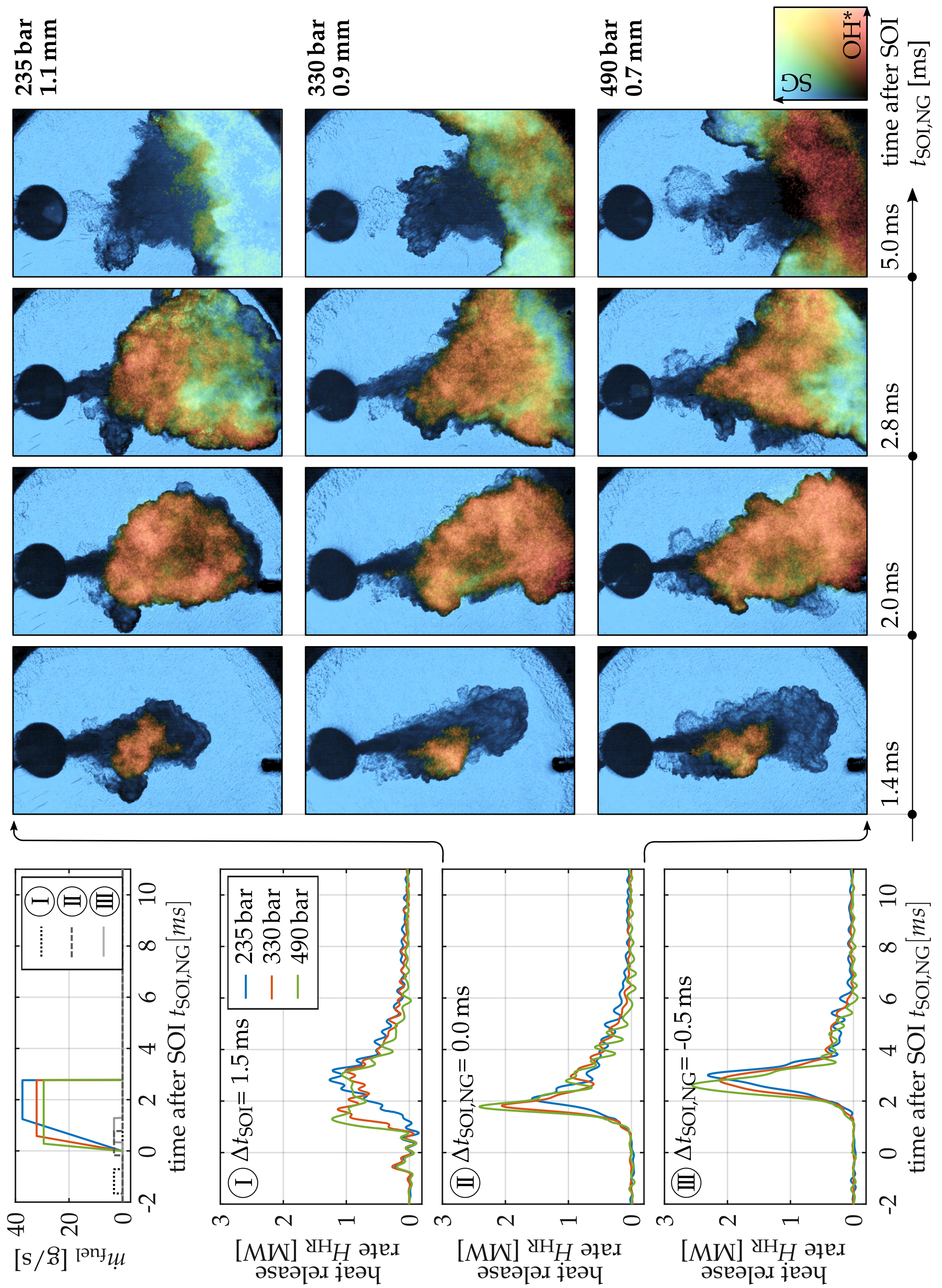

Figure 6.8: Heat release rates at OP1 for a variation of gas injection pressure at different relative injection timings Δt_{SOI} (Ⅰ-Ⅲ); image sequences showing simultaneous injection ($\Delta t_{SOI} = 0.0\,\mathrm{ms}$) at different gas injection pressures.

both pressures independently. In order to evaluate soot formation in the gas jet with minimum interference of soot from the diesel pilot, OP1 with partially-premixed diesel pilot combustion was selected. A variation of the degree of gas jet premixing is achieved with three different relative injection timings Δt_{SOI} of +1.5 ms Ⓘ, +0.0 ms Ⓘ︎Ⓘ and -0.5 ms ⅢⒾ. The needle lift is affected by the applied injection pressure and the injection rate curves are therefore not identical despite the constant injection duration, as shown in Fig. 6.8. This needs to be considered when assessing the results.

Since the first peak in heat release is attributable to premixed combustion, it provides a direct indication of the initial mixture formation and flame development. With early ignition and low premixing at Ⓘ an increase in injection pressure leads to an earlier and more intense start of combustion. Self-similarity of the steady-state jet assumes unaltered mixing rates at constant injection rate and therefore indicates that the difference in initial heat release at Ⓘ is attributable to the differences in mass flow ramp-up and flow velocity-induced flame propagation. With stronger premixing at Ⅱ, the difference in heat release among the injection pressures during premixed combustion is roughly unchanged (~2.0 ms after SOI at Ⅱ). However, the maximum heat release increases along with the amount of premixed fuel. Very late ignition at Ⅲ causes the maximum heat release due to premixed combustion to occur close to EOI, and the heat release rates for all pressure levels become very similar. This is plausible, since close to EOI the amount of injected and premixed fuel becomes independent of the injection pressure. A faster increase in heat release due to faster flame development at higher pressure remains, but is expected to diminish if the gas jet is ignited after EOI.

Because of the low number of repetitions and the small amount of energy released by only one pair of jets, the heat release rates show some oscillations. Nevertheless, a clear trend towards faster burnout can be observed with higher injection pressure after the end of injection (2.7 ms after SOI), irrespective of the degree of premixing. This is assumed to be mainly caused by faster mixing due to stronger entrainment when the injection rate is quickly ramped down to zero (see Sec. 2.1.3).

The SG/OH* image sequences show the combustion progress at different injection pressures in the case of medium premixing at Ⅱ. At the time of ignition 1.4 ms after SOI, faster jet penetration with higher injection pressures can be observed. The two cases with very similar injection rate curves (330 bar and 490 bar) show only a small difference in penetration length, again highlighting the impact of the opening ramp on the initial mixture formation. Only slightly affected by the injection pressure, the peak heat release occurs about 2.0 ms after SOI, when the flame extends across the whole jet. Regardless of the injection pressure no soot is detected up to the peak heat release, as observed in general at OP1. After the end of injection at 2.8 ms, all cases show soot luminescence but the reacting jet region differs in its shape and location. At high pressure the cone-shaped jet shows the strongest luminosity close to the chamber wall. In contrast a very large leading vortex structure is evident at low pressure, formed during the slow injection rate ramp-up. This vortex does not reach the chamber wall until EOI and shows only very low OH*- or soot luminescence close to the tip. Interestingly, the lift-off does not seem to be significantly influenced by the injection pressure. Although the intensity of soot luminescence is almost equal among all pressures at the end of injection, very late and intense soot luminescence is observed 5.0 ms after SOI at low injection pressure. The stronger post-injection mixing at higher pressures accelerates burnout, resulting in lower soot luminescence at this point in time.

The results show that high injection pressures foster fast burnout independent of the degree of premixing, which is beneficial for high engine efficiency and low emissions from incomplete combustion like PM and CO. Since the initial mixture formation is strongly affected by a faster mass flow ramp up, it is improved with increased injection pressure. In combination with the higher flow velocity, this causes an earlier and more intense start of combustion. The more intense premixed combustion does not increase the maximum heat release if the degree of premixing is low. If premixing is stronger, the peak heat release rate directly correlates with the injection pressure. Very strong premixing with late ignition close to EOI shows high peak heat release rates in general. However, the impact of the injection pressure on the heat release becomes increasingly limited at high injection pressure. It is therefore concluded that apart from the improved burnout, high injection pressures are especially beneficial for conventional

HPDF and may not be required for partially-premixed HPDF with very late ignition.

6.2.3 Sooting Propensity

This section is intended to cover the effects of various HPDF combustion parameters on soot formation. Since many of the investigations presented so far are also suitable to discuss soot formation, some figures previously introduced will be referenced again. The analysis is based on soot luminescence imaging, which is not able to provide quantitative information about the particle mass, number or size. Nevertheless, it allows a qualitative statement on how different parameters affects the local evolution and occurrence of soot. In combination with quantitative engine measurement data from literature, this understanding facilitates an assessment of the physical processes responsible for PM emissions and associated reduction strategies.

Even though studies of conventional HPDF combustion with minimum premixing (pilot injection prior to gas injection) show significantly lower engine-out PM emissions compared to conventional diesel operation, the emission levels are still relatively high [36]. Jones et al. [39] analyzed the contribution of diesel and natural gas to the overall PM emissions with an elaborate measurement approach using accelerometer mass spectrometry (AMS). Since the used diesel fuel from a biological source shows a different composition of carbon isotopes than the natural gas from a fossil source, an assignment of the black carbon in the PM to the two fuels is possible. At a load point with 12 bar gross indicated mean effective pressure (GIMEP) and no EGR, doubling of the pilot share from 2.5% to 5% resulted in only a small increase of the particle emissions attributable to the pilot by 15%. At the same time, however, the particles traced back to the natural gas combustion increased by 30% as well. Since the pilot contributes with only about 6% to the engine-out PM, a change in pilot quantity mainly affects PM formation in the gas jet. Thus, there is an amplifying effect of the pilot on soot formation in the gas jet, which could not be further analyzed in the mentioned study due to lack of optical accessibility and due to fixed jet interaction.

There are several possible reasons for this strong **effect of pilot fuel combustion** on PM emissions. On the one hand, the adjacent diesel jet reduces the entrainment of air to the gas jet and thus leads to generally richer conditions. On the other hand, soot particles and their precursors formed in the pilot jet are mixed into the gas jet, cannot oxidize in the rich zones of the gas jet and may even further promote particle inception, growth and agglomeration. It is difficult to isolate the effects experimentally, as the operating conditions, the jet arrangement and the degree of premixing have to be held constant while the pilot soot level is altered. Figure 6.9 shows the initial phase of gas jet combustion at OP4 for two different relative injection timings ($\Delta t_{\mathrm{SOI}} = +1.0\,\mathrm{ms}/\pm 0.0\,\mathrm{ms}$). Due to the early pilot injection at $\Delta t_{\mathrm{SOI}} = +1.0\,\mathrm{ms}$ the pilot soot is oxidized before the hot combustion products ignite the natural gas jet at otherwise unchanged conditions. Even though the relative injection timing is different for the two experiments shown, the degree of natural gas premixing is very similar since both jets ignite about 1.0 ms after SOI.

If the natural gas jet interacts with the pilot after being started simultaneously ($\Delta t_{\mathrm{SOI}} = +0.0\,\mathrm{ms}$), diesel pilot soot is mixed into the gas jet at the time of natural gas ignition 1.0 ms after SOI. It is carried towards the jet tip by the strong natural gas flow and intense soot luminescence is observed from the very beginning on the side facing the pilot jet. A comparison of the two image sequences indicates more intense soot luminescence across the whole gas jet due to the entrained soot from the pilot jet. In contrast, ignition by a pilot free from soot at $\Delta t_{\mathrm{SOI}} = +1.0\,\mathrm{ms}$ leads to initial flame propagation in the gas jet with hardly any visible soot concentration. Nevertheless, the region where the jets interact during ignition is the first to show soot luminescence in both cases. It is therefore concluded that strong temporal or spatial overlap between the jets is to be avoided for low PM formation caused by jet interaction. Furthermore, any measure reducing pilot soot will show an even stronger effect on soot formation within the gas jet.

This is also why the **effect of the conditions in the combustion chamber** on soot formation has to be assessed both by their influence on pilot and on gas jet combustion. As Fig. 6.7 shows, the low compression ratio at OP1 result in a positive pilot mixture dwell and thus in a pilot combustion free from soot luminescence (see also Sec. 5.1). Subsequently, no soot formation

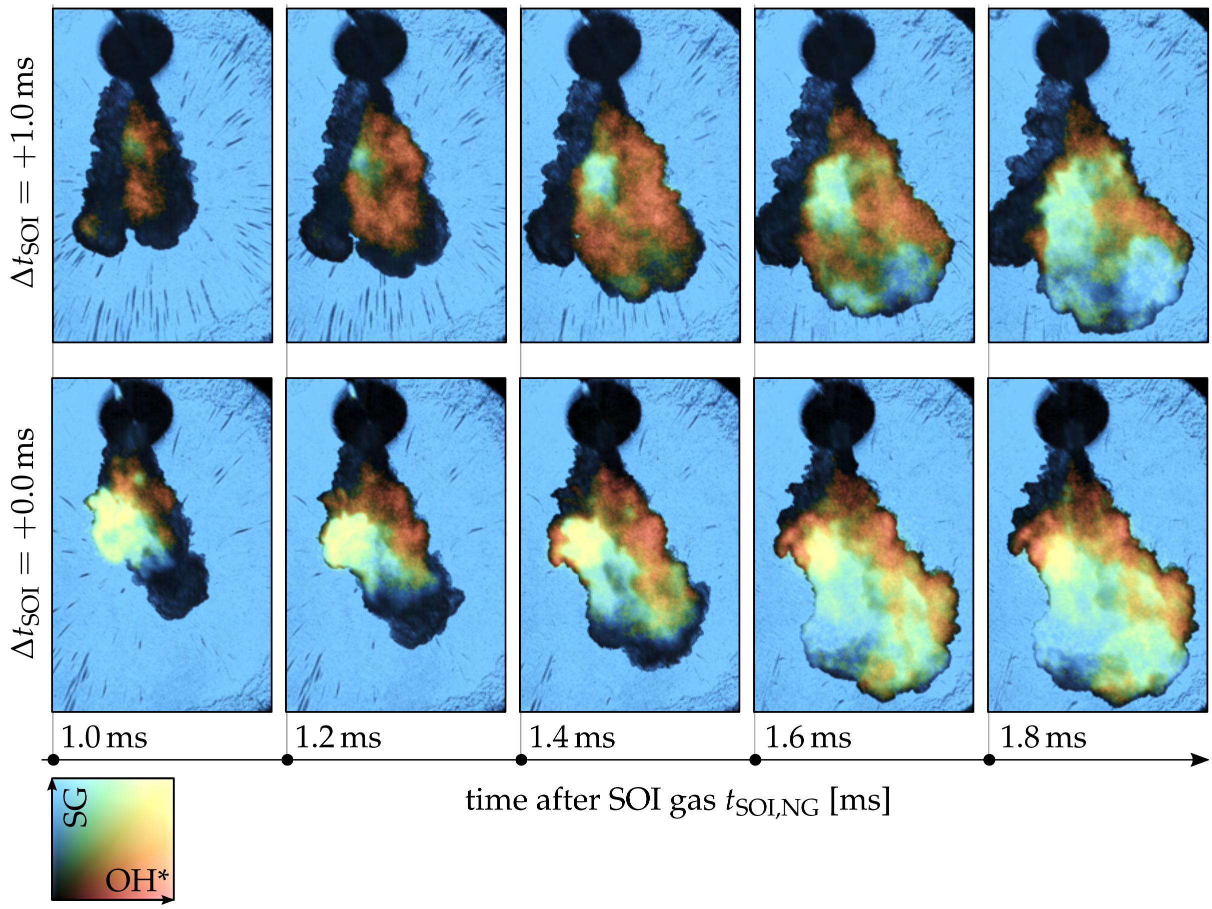

Figure 6.9: Influence of pilot soot on NG jet soot luminosity during the initial phase of natural gas combustion by comparison of early pilot injection ($\Delta t_{SOI} = +1.0\,\mathrm{ms}$) and simultaneous injection ($\Delta t_{SOI} = \pm 0.0\,\mathrm{ms}$) at OP4.

is visible in the interaction region of the two jets during initial flame spread. It is only after the peak heat release that soot distributed homogeneously across the jet cross-section is observed far downstream close to the wall. In contrast, the pilot with high soot concentration at OP4 is the starting point for early soot formation in the gas jet. At the same time not only the flame lift-off but also the lift-off of the sooting zone is shorter at OP4 after EOI at $t_{SOI,NG} = 3.0\,\mathrm{ms}$. The analysis of the operating condition's effect on the heat release rate indicated that the more intense peak in heat release at OP4 is caused by the wider burning limits. Since these wider limits cause richer mixtures to react, they are also assumed to be responsible for more intense soot formation in the gas jet. The combination of more soot from interaction with the pilot and from the natural gas jet combustion itself sums up to the notably stronger soot luminescence at OP4 in Fig. 6.7.

The strong **effect of the injection pressure** on the evolution of soot luminescence during the late combustion phase was discussed in Sec. 6.2.2 based on the results of a combined variation of injection pressure and orifice diameter in order to maintain a constant injection duration. The SG/OH* images show that soot oxidation after end of injection is accelerated if the injection pressure is increased. This is supposed to be the main reason for the positive effect of high injection pressures on low engine-out PM and CO emissions reported in the literature [58, 61].

A completely different mitigation strategy is the **suppression of soot formation by increased natural gas premixing**. In HPDF combustion this is realized by a negative relative injection timing. Experiments on a single cylinder research engine (SCRE) have shown that as soon as Δt_{SOI} is reduced below zero, a strong drop in PM can be observed [22]. The image sequence in Fig. 6.10 shows the combustion progress with late gas jet ignition 2.4 ms after SOI by $\Delta t_{SOI} = -1.0$ ms. In order to minimize the pilot's influence on soot formation, the low compression ratio at OP1 was selected. Even though natural gas jet ignition is observed just right before EOI, the jet core nevertheless shows soot luminescence starting about 0.4 ms after EOI ($t_{SOI,NG} = 3.2$ ms). At this time, the flame still propagates towards the outermost and foremost parts of the jet. These lean regions there are the last to be reached by the flame and are therefore presumably responsible for the strong increase in unburned methane emissions with enhanced premixing observed by Faghani *et al.* [22]. Another downside of this operating strategy is the high peak in heat release rate and therefore the high pressure rise rate caused by the rapid combustion of a large amount of premixed fuel (see Fig. 6.5).

It has to be noted that the freely propagating single jet pair experiments fail to fully represent the conditions in a full-scale engine application, especially when strong premixing is investigated. If the gas jet is to be ignited after EOI in the single jet configuration, the low global equivalence ratio causes the natural gas zone to become very lean and the large free path length allows it to penetrate far from the injector. In contrast, the compact piston bowl and the concentric multi-jet arrangement in a combustion engine restrict mixture formation. But if soot luminescence is observed in the single jet experiments even with strong premixing, soot

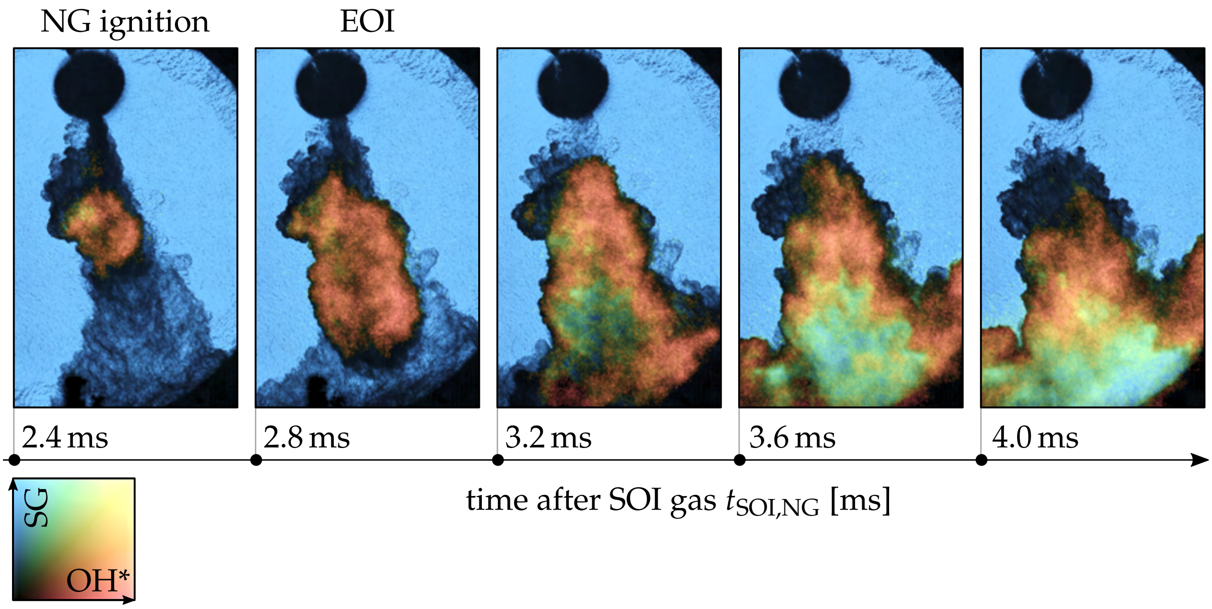

Figure 6.10: Image sequence showing the combustion progress and evolution of soot luminosity with late ignition (2.4 ms after SOI but still prior to EOI) at OP1.

formation in an engine combustion chamber at the same relative injection timing can be expected to be at least as intense.

6.2.4 Numerical Analysis

For better understanding of the simultaneous progression of mixing, reaction and pollutant formation, results from investigations with the numerical model introduced in Sec. 4.3 are analyzed. Two cases at OP4 with different levels of premixing of the gas jet at the time of ignition are selected. In both cases, the jets are arranged at an angle of α=+10°. The fuel mass distribution in the ϕ-T space is plotted for the two cases in Figures 6.11 and 6.12 at selected times relative to natural gas SOI. In addition, the plots in the center column show the mixture distribution of unburnt and burnt fuel. These curves are directly derived from the ϕ-T plots using the air charge temperature as a threshold value. For more information on the numerical data analysis method see Sec. 4.3.

Due to the late natural gas ignition, the case shown on the right hand side (relative injection timing $\Delta t_{SOI} = -1.5$ ms) allows an evaluation of the mixture formation in the non-reacting gas jet up to about 2.2 ms after

SOI. Already at $t_{\mathrm{SOI,NG}} = 1.0\,\mathrm{ms}$ the largest share of unburned fuel is found in regions with $\phi < 3$. While the maximum of the unburned fuel distribution becomes leaner as the injection proceeds, the distribution of fuel at equivalence ratios higher than this maximum does not change. The corresponding rich conditions are found in the upstream region of the jet that reaches steady state first. The mixture distribution of a non-reacting, non-confined steady-state gas jet (green dotted line) was derived from a fit to the part of the unburnt fuel distribution that does not change while injection is ongoing. An arrow marks the region where the unburned steady-state jet mixture distribution applies. Equivalence ratios below the arrow close to the maximum of the unburned fuel distribution can be mainly assigned to the tip vortex, which is supplied with fuel via the upstream steady-state jet region. The jet tip vortex increases in size and becomes leaner while it propagates. About 1.8 ms after SOI but still prior to natural gas ignition, the range of equivalence ratios where the steady-state assumption applies stops to further extend towards leaner values. Instead, an increasing amount of fuel accumulates directly below $\phi = 1.8$ (compare the unburnt mixture distribution at $t_{\mathrm{SOI,NG}} = 1.8\,\mathrm{ms}$ and $t_{\mathrm{SOI,NG}} = 2.2\,\mathrm{ms}$). This is the point in time when the jet hits the chamber wall and therefore no longer follows a trajectory towards self-similarity. The equivalence ratio of 1.8 is expected to correspond to the value at the jet axis right before intersection with the wall. Please note that the x-axes showing the relative fuel mass are scaled differently in Fig. 6.11 and 6.12 for the sake of appropriate resolution.

The series of diagrams showing strong premixing with $\Delta t_{\mathrm{SOI,NG}} = -1.5\,\mathrm{ms}$ is also suitable to discuss the process of pilot fuel ignition. Right after diesel SOI a slight temperature increase to less than 1000K of mixtures in the range of $\phi = 0.5 - 3$ can be observed at $t_{\mathrm{SOI,NG}} = 1.4\,\mathrm{ms}$, indicating the first stage of diesel auto-ignition[3]. At $t_{\mathrm{SOI,NG}} = 1.8\,\mathrm{ms}$, second stage ignition has already led to a much stronger temperature increase. The slightly higher adiabatic flame temperature of diesel compared to natural gas does not explain the large gap between the temperature of the diesel products and the NG adiabatic flame temperature line at $\phi > 2$. Rich mixtures show temperatures higher than equilibrium as a result of the simultaneously

[3]Note that diesel injection starts at $t_{\mathrm{SOI,NG}} = 1.38\,\mathrm{ms}$ in this simulation. For further information on the fuel injection rate and SOI determination see Sec. 3.2.

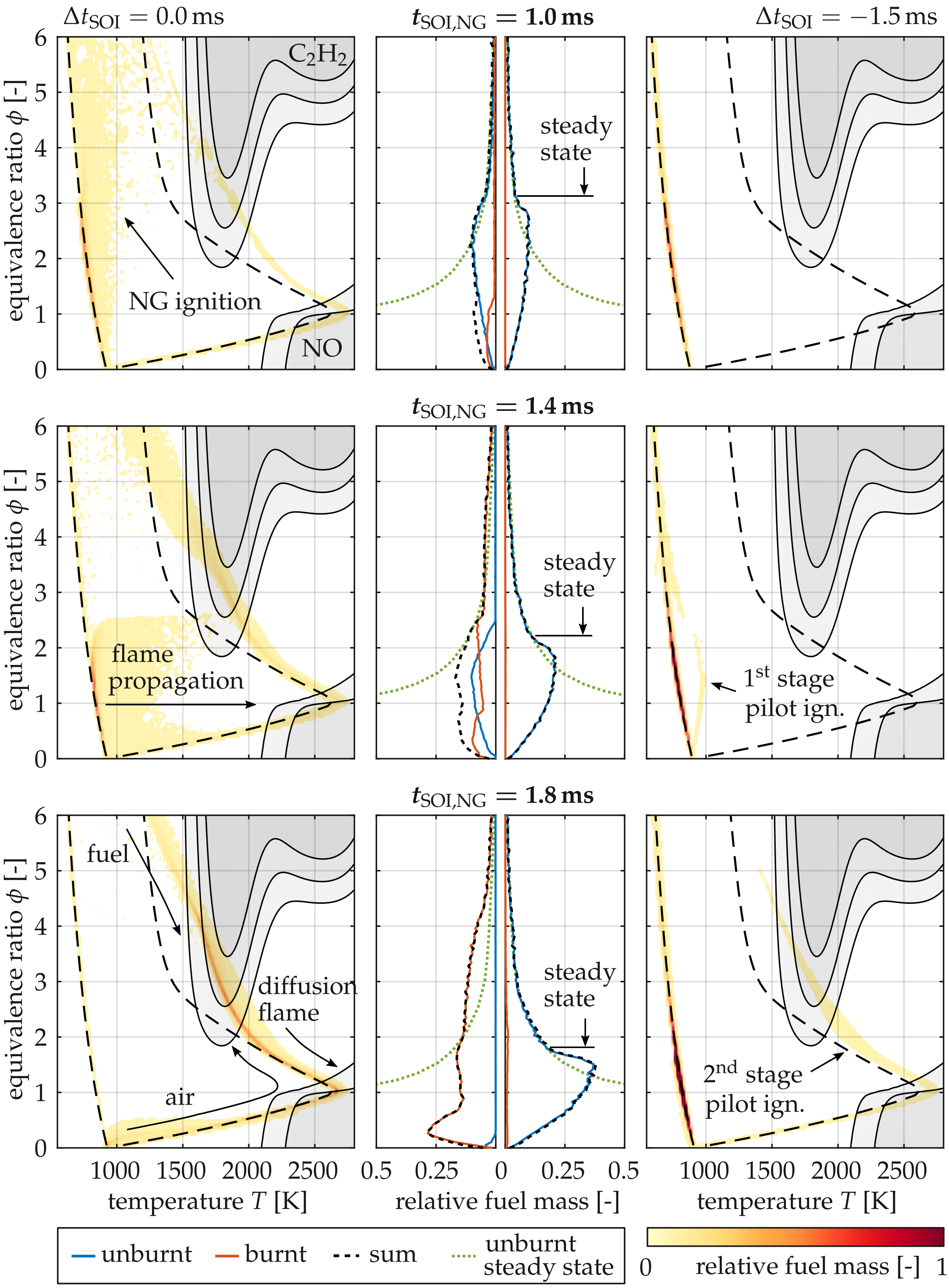

Figure 6.11: ϕ-T plots for low premixing (left, $\Delta t_{SOI} = 0.0$ ms) and strong premixing (right, $\Delta t_{SOI} = -1.5$ ms), as well as burnt/unburnt mixture distribution (middle) between $t_{SOI} = 1.0 - 1.8$ ms; continued in Fig. 6.12.

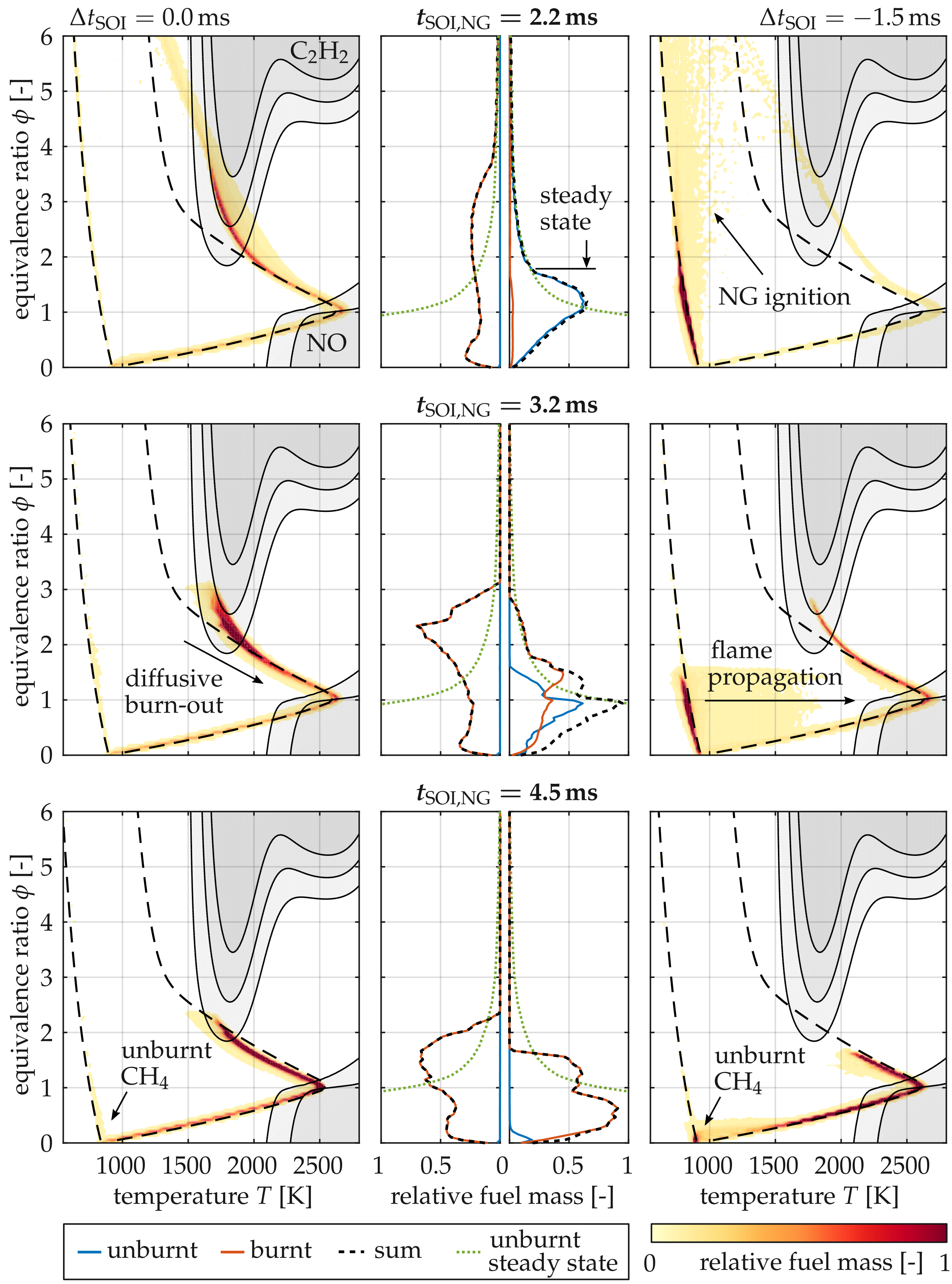

Figure 6.12: ϕ-T plots for low premixing (left, $\Delta t_{SOI} = 0.0$ ms) and strong premixing (right, $\Delta t_{SOI} = -1.5$ ms), as well as burnt/unburnt mixture distribution (middle) between $t_{SOI} = 2.2 - 4.5$ ms; continued from Fig. 6.11.

ongoing mixing and reaction progress while fuel injection is still ongoing. Since natural gas jet combustion shows the same behavior, the effect is discussed there right below.

Natural gas jet ignition is shown for both cases and can be recognized by a considerable amount of fuel starting to detach from the mixing line. The full range of mixture qualities is involved in natural gas combustion right from the beginning. This seems obvious since ignition takes place in the shear layer only a few millimeters downstream the orifice, where all equivalence ratios can be found. While the flame propagates towards the jet tip during premixed combustion, the rich zones in the jet core are the first to be consumed. In the case of low premixing ($\Delta t_{\mathrm{SOI}} = 0.0\,\mathrm{ms}$) virtually all the unburned mixture left 0.4 ms after NG ignition ($t_{\mathrm{SOI,NG}} = 1.4\,\mathrm{ms}$) is leaner than $\phi = 2.5$.

Immediately after NG ignition all reacting fuel with $\phi > 1$ shows significantly higher temperatures than the corresponding adiabatic flame temperature at chemical equilibrium. This would not be possible by burning a fuel-air mixture at constant equivalence ratio, since the temperature would increase from the mixing line and approach the adiabatic flame temperature when chemical equilibrium is reached. Therefore, the simultaneous progress of reaction and mixture formation in the jet has to be responsible for the high temperatures. Since the reaction zone covers the entire jet up to the lift-off length, the fuel-rich inner region becomes leaner downstream of the lift-off length only by mixing with combustion products from the diffusion flame in the shear layer (see also the phenomenological description of a reacting diesel jet in Sec. 2.2).

A simple 0D chemical reactor model is used to mimic this process. It employs the same reaction mechanism as the 3D CFD calculations [98] and consists of only one perfectly stirred reactor. The reactor is initialized with a stoichiometric mixture at equilibrium (2780 K and 125 bar) before a constant mass flow of cold fuel is added. This process is intended to resemble the entrainment path of a fluid element at the diffusion flame within the shear layer, gradually being fed with fuel while drawn towards the jet core. Different mixing rates are investigated by adjusting the fuel mass flow rate such that an equivalence ratio of $\phi = 4.6$ is achieved within a specified mixing time (40μs to 100 ms). Figure 6.13

shows the results of the reactor calculations, presented in the ϕ-T plot from Fig. 6.12 for $\Delta t_{SOI} = 0.0\,\text{ms}$ after premixed flame propagation at $t_{SOI,NG} = 2.2\,\text{ms}$. If any chemical reactions are suppressed, the reactor temperature follows the black dotted mixing line starting from $\phi = 1$ and $T = 2780\,\text{K}$. In the reacting case with very fast mixture formation within only 40μs, the temperature develops close to this mixing line, showing a considerable chemical limitation. But even with mixture formation slowed down by 3 orders of magnitude, the equilibrium temperature is by far not reached. When compared in the ϕ-T plane, the range of the results from the simplified model correlates very well with the region where the reacting fuel accumulates in the CFD results. Although this phase of fuel jet combustion is often referred to being mixture-limited, a considerable deviation from equilibrium can be observed.

This kind of mixture formation in a reacting jet has a strong influence on soot formation since it leads to fuel-rich mixtures in an intermediate temperature range of 1500-2000 K. As indicated by the contour lines of the soot tracer species acetylene (C_2H_2) in the ϕ-T plot (see also Sec. 4.3.2), these are exactly the conditions that lead to the highest formation rates [44]. However, the C_2H_2 contours cannot be used to quantify the effect since they

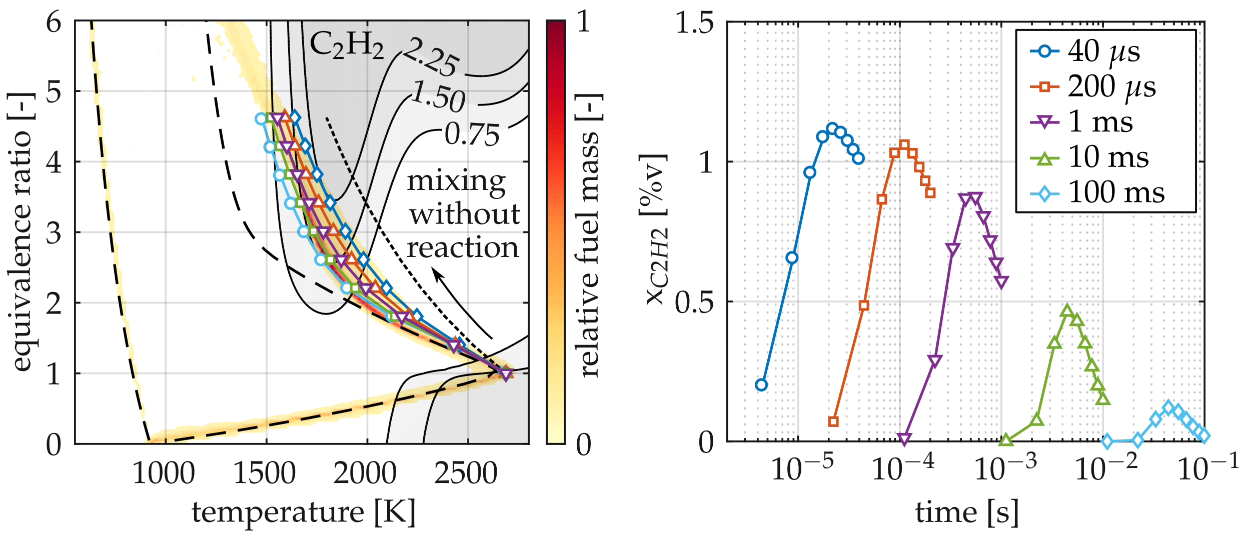

Figure 6.13: Results from Cantera constant pressure reactor calculations, initialized with $\phi = 1$ and $T = 2780\text{K}$ at equilibrium before adding fuel at different rates up to $\phi = 4.6$ within 40μs to 100ms; representation in the ϕ-T space of $\Delta t_{SOI} = 0.0\,\text{ms}$ at $t_{SOI,NG} = 2.2\,\text{ms}$ (left) and evolution of acetylene concentration (right).

were determined using stationary, isothermal reactors initialized with an unburned mixture of fuel and air. The evolution of C_2H_2 concentration in the 0D reactor gives only an indication as well, since the complex mixture formation process in the jet was strongly simplified. Nevertheless, the curves presented in Fig. 6.13 on the right show that fast mixing of fuel to a reaction zone does not only result in higher temperatures but in a higher acetylene concentration as well. It is therefore concluded that soot formation in the gas jet is not caused by the reaction of rich mixtures alone, but additionally intensified by the fact that fuel is constantly fed to and mixed with a reacting zone covered by a diffusion flame.

Figures 6.11 and 6.12 furthermore indicate a strong feedback of combustion on the mixture formation process. If the jet is ignited very early (left column), the evolution of overall mixture distribution (sum) shows a significantly higher share of fuel being accumulated in fuel-rich zones at approximately $\phi = 2 - 5$ compared to a non-reacting jet (right, up to 2.2ms after SOI). A possible explanation for inferior mixture formation at the burning jet is the decrease in density and viscosity associated with the reaction, reducing turbulent dissipation. It is therefore concluded that the occurrence of soot in a reacting NG jet is promoted by the combination of the two identified effects. Mixture temperatures above the equilibrium temperature in the rich inner parts of the jet facilitate high formation rates. As a consequence of the reaction, reduced air entrainment to the jet leads to the accumulation of fuel at exactly these equivalence ratios. The comparison between the two presented cases shows that the difference in mixture distribution is retained for a very long time even after the end of the injection. Thus not only the formation but also the oxidation of soot in the burnout phase is affected by the slower mixture formation of a reacting jet.

The numerical results show how PM emissions can be reduced with substantial premixing of the gas jet. Since the rich upstream zones are ignited first by direct interaction with the diesel pilot jet, soot formation may only be avoided if ignition is delayed beyond EOI. The downside of such strong premixing is a significant increase in unburnt CH_4 emissions because the flame reaches the lean zones at the jet tip at last (see last plot in Fig. 6.12). In contrast to the presented investigations with a freely propagating single jet pair, the smaller chamber geometry and adjacent fuel jets in a HPDF engine counteract the formation of very lean regions. Full-scale engine experiments have shown that increasing the global equivalence ratio of the charge can prevent over-mixing and thereby limit the rise in unburnt CH_4 with premixing [22]. However, the same investigation also showed that the general trade-off between PM and unburnt CH_4 emissions as a function of the degree of premixing is preserved in a full-scale combustion engine.

7 Wall-bounded Natural Gas Jet

Due to the limited size of the combustion chamber in internal combustion engines, interaction between the directly injected fuel jets and the chamber wall, i.e. the piston bowl, cannot be avoided. The wall influences mixture formation and all dependent subsequent processes. For the investigations presented in this chapter, the free path length of the fuel jets is reduced by an additional wall. The wall contour is designed using the insights from the investigation of a freely propagating jet pair in the previous chapters.

At first, the most important findings are summarized in order to formulate design guidelines. The guidelines are then applied to the wall contour design. After introducing the necessary modification of the RCEM experimental setup, the wall's effect on mixing and combustion is characterized by a comparison of the results to the ones from the freely propagating jet pair. A special focus is set to partially premixed HPDF combustion and to combustion at reduced load since these are particularly affected by the presence of a wall.

7.1 Chamber Wall Design

The piston bowl design for direct-injection engines is typically optimized with respect to mixture formation. In its simplest form, this is done by maximizing the free path length and air utilization, as for example with an ω-bowl. A different approach is the improvement of mixture formation after the jet has hit the wall by designing the contour to split and deflect the jet, eg. by a step bowl. As a result, the rich zones detach from the wall and burn out faster. In the case of HPDF combustion – and in particular with partially premixed HPDF – the wall can affect the interaction between the diesel pilot and natural gas jets by its impact on spatial mixture distribution.

Apart from improved mixture formation, the wall contour can therefore be designed to allow for an alternative ignition location and tailored flame propagation.

7.1.1 Design Guidelines

The investigations in Ch. 6 provide an in-depth understanding of the physical processes governing the diesel-piloted combustion of a natural gas jet. The potential for HPDF combustion optimization resulting from these fundamental investigations is briefly summarized first. To realize this potential, design guidelines for jet arrangement and wall contour design are then formulated.

If the interaction between the diesel pilot and natural gas jets is minimized, both are provided with the best possible air supply. Soot formed in the pilot jet can burn out freely and soot formation in the gas jet is reduced. Nevertheless, interaction must be sufficient for stable ignition. Interaction between the jets is supported by the strong entrainment of the gas jet, which is the reason why gas jet ignition is possible at angles considerably larger than 20°. A low spatial overlap furthermore reduces the disturbance of pilot mixture formation by the gas jet. As a consequence, auto-ignition of the pilot fuel jet is successful even if the amount of pilot fuel is small, the pilot injection duration is short or the pilot ignition delay is long.

Apart from jet interaction, PM emissions from HPDF combustion are affected by various other parameters as well, like e.g. fuel injection pressure or charge conditions. However, the largest potential for a general suppression lies in partially premixed combustion. The main mechanism for intense soot formation in the natural gas jet is the continuing supply of fuel to a zone with hot combustion products, resulting in a very rich mixture with a temperature above the adiabatic flame temperature (see Sec. 6.2.4). Since strong entrainment after end of injection causes very rapid degeneration of zones with $\phi > 2$, soot formation is effectively suppressed by delaying ignition after EOI.

Another argument in favor of strong premixing is the reduction of combustion duration by minimized mixture-limited burnout. This results in a considerable potential for higher thermal efficiency. At the same time the direct coupling between mixing rate and heat release rate is eliminated with premixing. Therefore the need for a very high natural gas injection pressure to realize short injection and rapid mixture formation is reduced. However, the negative effects associated with strong premixing are high pressure rise rates and combustion noise, elevated NO_x levels and severely increased CH_4 emissions [22, 62].

With an integrated, centrally located dual-fuel injector it is not possible to significantly influence the location of gas jet ignition by direct interaction with the pilot jet (see Sec. 6.1.2). Irrespective of the jet arrangement or relative injection timing, entrainment initiates gas jet combustion in a narrow region close to the orifice. Thus the initial reaction zone is formed in the richest part of the jet and spreads from there. Immediate supply of a rich fuel mixture to the reaction zone causes intense soot formation to set in right after ignition, no matter how much fuel there is already premixed further downstream. This kind of flame propagation is also responsible for the increase in unburned CH_4 emissions along with the degree of premixing since the lean downstream regions are reached by the flame at last. And finally, propagation of a flame starting close to the orifice is accelerated by the jet flow. As a result, the partially premixed zones are consumed more rapidly and the associated intense peak in heat release leads to high pressure rise rates. Such harsh combustion events have to be avoided since they impose high mechanical stress on the components, cause combustion noise and limit partially-premixed operation to part load conditions.

This summary shows that partially premixing the natural gas is beneficial in terms of avoiding soot emissions and maximizing efficiency, but also leads to some negative effects. These negative effects are caused in parts by the upstream ignition location of the propagating gas jet. If jet propagation is now affected by a chamber wall anyway, the wall design can be used to alter the mixture field and to tailor ignition location and flame propagation. The following guidelines are used to design a wall contour that is optimized for both, conventional and partially-premixed HPDF:

1. After substantial mixing with air, the natural gas jet is preferably ignited at its tip. This is only possible if the tip is redirected back

towards the injector and the pilot jet. To realize this redirection, the jet momentum needs to be preserved by gradual deflection.

2. Entrainment is low as long as the jet is in contact with the wall. Therefore, the length of wall interaction should be minimized, and the jet should be forced to detach from the wall after deflection for improved mixture formation. An overlap of the redirected jet tip with the upstream flow field would deteriorate air entrainment and should be avoided. These measures will improve late mixture formation for both, conventional and partially-premixed HPDF.

3. If the gas jet is ignited at its tip, the flame has to propagate against the mean jet flow. This is assumed to reduce the maximum heat release rates and associated pressure rise rates.

4. In order to realize both conventional and partially-premixed HPDF by simply adjusting the relative injection timing, a direct interaction between pilot fuel and natural gas jet independent of the wall interaction should be preserved. However, the spatial overlap is to be kept low for undisturbed pilot auto-ignition and maximum air supply to both fuel jets.

5. Preserving ignition due to direct interaction between the two fuel jets is desirable for partially-premixed HPDF as well. Since strong entrainment after EOI causes the upstream part of the natural gas jet to become lean very quickly, dedicated ignition of this lean mixture is expected to minimize unburnt CH_4 emissions.

6. Since the fuel mass at part load is reduced by decreasing either the injection duration or the injection pressure, the resulting lower jet momentum causes reduced jet penetration. As a consequence, the jet is not completely redirected and ignition at the tip may fail. This is another argument why direct interaction between the two jets in the upstream region is important.

As a consequence of premixing, the higher combustion temperatures are expected to result in rising NO emissions [57]. The increase in NO emissions can effectively be counteracted by EGR, which does not cause the typical NO/PM trade-off if applied to partially premixed HPDF [22,62].

Since the experimental setup with a single-shot RCEM does not allow for emission measurements, EGR was not considered. Nevertheless, the design guidelines presented here are not affected by the possible use of EGR.

7.1.2 Wall Contour Design

The CFD model introduced in Ch. 4 is not only a valuable tool for combustion analysis, but also for the design of the combustion process and the combustion chamber geometry in particular. It is used to design a wall contour according to the guidelines presented in the previous section, avoiding extensive experimental parameter variation. Only the final design is applied to the RCEM and tested.

For the design process, the numerical setup is simplified by using a constant chamber volume that is initialized with a quiescent charge. The temperature and pressure correspond to the ones at TDC of OP4, as this operating point was chosen for all experimental investigations of the wall-bounded natural gas jet. Figure 7.1 visualizes the result of a simulation of partially-premixed combustion during the design process by showing the evolution of the mixture and temperature field in the plane of maximum jet interaction. The requirement for minimum geometrical overlap is addressed with an interaction angle of $\alpha = 20°$ between the jet axes. After the gas jet has propagated freely for about 45 mm, it impinges on the wall and is gradually deflected. As soon as the jet flow has been redirected towards the diesel pilot, it detaches from the wall due to a step in the contour. This minimizes the length of wall interaction and ensures rapid entrainment after the jet has left the concave wall segment.

The depth and shape of the concave wall segment are designed in such a way that the gas jet is redirected and faces the diesel pilot when injection ends. The jet tip leaves the cavity in a well-mixed state with a maximum equivalence ration of $\phi \approx 2$. The structure of the leading jet vortex is still preserved after the deflection and can be recognized by the mushroom-shaped contours. An overlap of the jet tip with the upstream jet flow field prior to the end of injection is avoided. In the case shown, pilot injection is delayed in order to ignite the gas jet at its tip and and close to the orifice simultaneously right after the end of NG injection. Up to this moment the

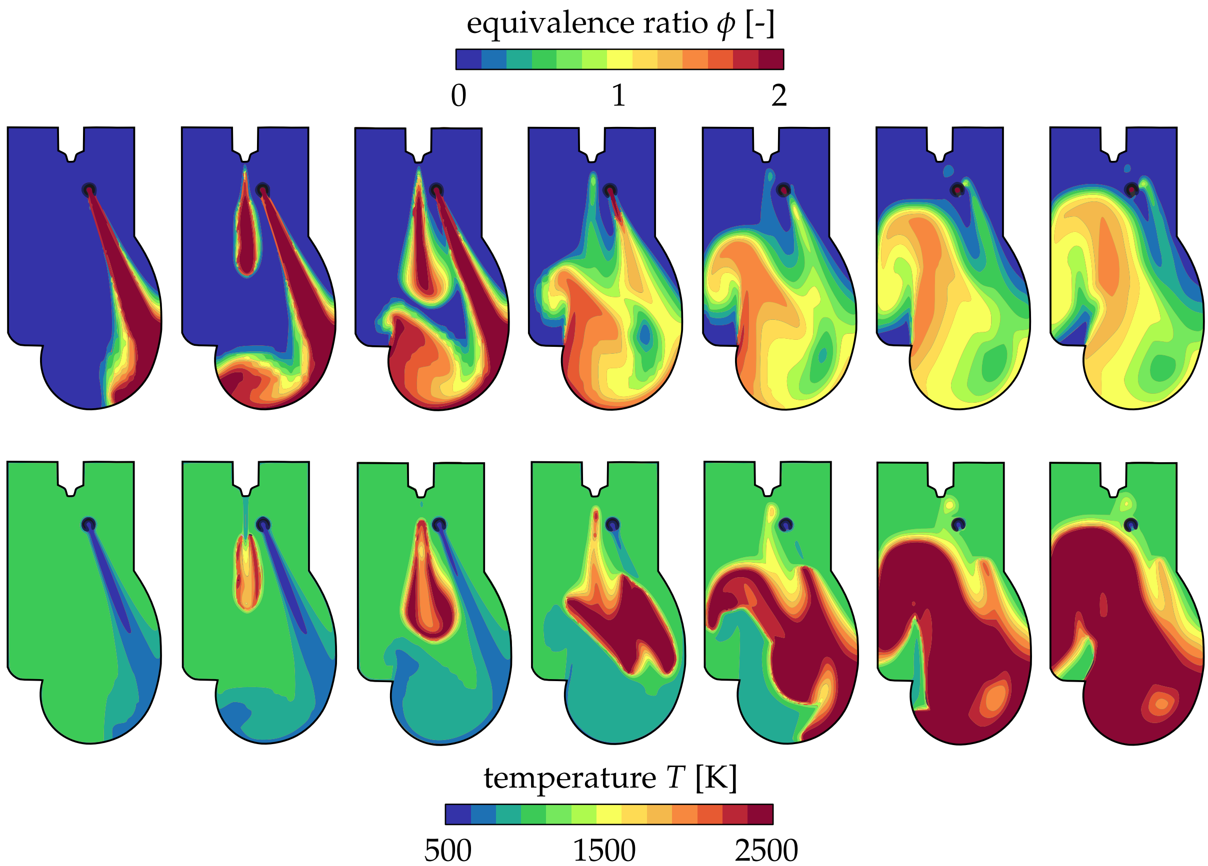

Figure 7.1: Visualization of the equivalence ratio and temperature field in the central cross-section showing partially-premixed combustion of a wall-bounded natural gas jet.

pilot can propagate, ignite and burn freely without being entrained into the gas jet core. The flame spreads slowly in the upstream jet region and simultaneously starts to cover the jet's tip vortex. After EOI, the richest zone is located close to the wall right where the jet exits the concave wall segment. This rich zone is the last one to be reached by the flame, allowing it to become leaner as long as possible. At all times, only mixtures with $\phi < 1.5$ are involved in the combustion process and no fresh fuel is fed to the reacting zone. It is therefore assumed that soot formation can be effectively avoided. Although gas jet ignition close to the the orifice is successful, some of the gas leaving the injector with low momentum after EOI is not reached by the flame. This source of unburned fuel is a general problem of direct fuel injection. The sequence indicates that the jet deflection may be further optimized for the tip to reach this unburnt mixture in the wake of the gas jet.

7.1.3 Modification of the Experimental Setup

In the experimental setup at the RCEM the chamber wall is realized by an additional part mounted to the circular volume reduction at the cylinder head, as shown in Fig. 7.2. Since the altered chamber geometry has a severely smaller cross-sectional area, the depth of the cavity is increased and the piston displacement reduced in order to achieve the compression ratio of OP4. To prevent the gas jet from escaping the cavity towards the piston, a small step ③ is introduced. This step keeps the jet compact within the desired direction of deflection. The resulting loss of observable area is low as indicated by the actual shape of the cavity in all the presented SG/OH* images.

Since the additional mount at the RCEM covers most of the free cylinder head area, the pressure sensor had to be mounted in a small recess. This causes an increase in high-frequency noise on the pressure signal and stronger signal filtering becomes necessary. In order to still provide meaningful heat release rates, each measurement point presented in this chapter was repeated six times instead of only three times.

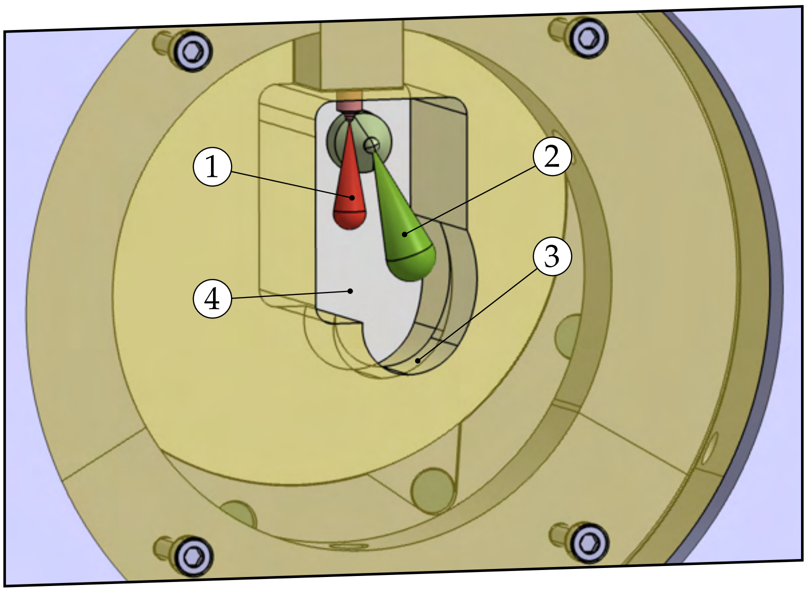

Figure 7.2: Realization of a wall-bounded natural gas jet by an additional part mounted to the RCEM cylinder head: ① diesel pilot jet, ② natural gas jet, ③ jet deflection with small step, ④ surface mirror for SG imaging.

7.2 Combustion Characterization

Since jet propagation is restrained by the wall, it affects not only the ignition location but also mixture formation. The influence of reduced air entrainment due to wall interaction on the combustion progress is investigated first for conventional HPDF, before the relative injection timing is varied for a characterization of partially premixed HPDF combustion. Finally, the injection duration is reduced to show the effect of lower fuel jet momentum and insufficient deflection on combustion at part-load conditions.

7.2.1 Mixture-Limited Combustion

Figure 7.3 demonstrates the effect of the wall on the combustion progress during predominantly mixture-limited, conventional HPDF combustion. For this purpose, the heat release from a freely propagating and a wall-bounded natural gas jet are directly compared. Minimum premixing for conevtional HPDF is achieved by a relative injection timing of $\Delta t_{\mathrm{SOI}} = +0.5\,\mathrm{ms}$, causing natural gas jet ignition at 1.3 ms after SOI. The selected case with free jet propagation is the same as Ⓑ at OP4 in Fig. 6.7, where a sequence of the SG/OH* images is presented.

The wall affects natural gas mixture formation already at a very early stage, visible by a significantly lower peak in heat release caused by partially-premixed combustion about 1.9 ms after SOI. The image sequence shows that ignition due to tangential jet interaction occurs early during jet propagation, so that the gas jet is completely covered by the flame before being deflected. Therefore the ignition location and initial flame propagation are not changed. However, air entrainment is already constrained on the side facing the wall.

After the end of injection (grey shaded area in the diagram) a relatively fast burn-out causes the heat release to drop significantly in the case of a freely propagating jet. With the wall present, the gas jet tip is just about to exit the concave wall segment at this point in time. When the tip leaves the cavity, entrainment is improved and the heat release rate

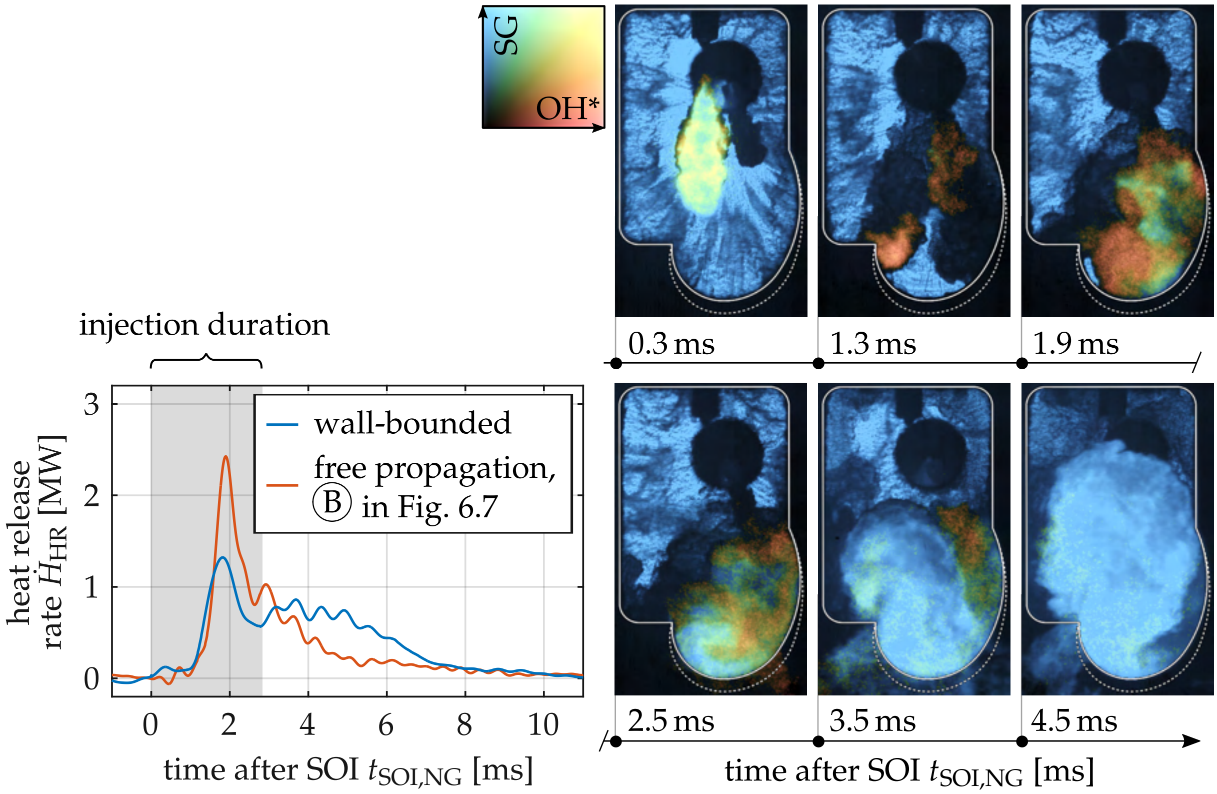

Figure 7.3: Influence of the wall on conventional HPDF combustion by comparison of heat release rates with early ignition at 1.3 ms after SOI; image sequence shows combustion progress with wall, for sequence of freely propagating gas jet see Fig.6.7.

increases slightly. Although the injection has already been completed, a sustained high conversion rate can be observed, caused by the continued burnout of fuel-rich mixture leaving the cavity. Only about 5 ms after SOI (2.3 ms after EOI) the heat release rate starts to decline. The long combustion duration is accompanied by very strong soot luminescence, which is brightest close to the trailing edge of the concave wall segment. Although the OH* signal is generally weak during diffusive natural gas burnout, the zones of improved mixture-limited oxidation behind the trailing edge of the concave wall segment and in the wake of the jet can be recognized.

7.2.2 Partially-Premixed Combustion

Partially-premixed HPDF combustion is realized by a reduction of the relative injection timing Δt_{SOI} between the pilot fuel and natural gas jet only. All other parameters remain unchanged. Figure 7.4 shows heat release rates and SG/OH* image sequences for four different relative injection timings, synchronized with respect to natural gas SOI. The case with $\Delta t_{\mathrm{SOI}} = +0.5\,\mathrm{ms}$ corresponds to the one from Fig. 7.3 and is presented here again for the sake of completeness. At this low degree of premixing, only a fraction of natural gas is consumed by premixed flame propagation. The main share is injected into an already reacting, fuel-rich region and burns off accompanied by strong soot formation.

Later pilot fuel injection relative to natural gas SOI[1] ($\Delta t_{\mathrm{SOI}} = -0.5\,\mathrm{ms}$) results in a slightly higher but mainly wider heat release rate peak. This was not observed for a freely propagating gas jet (see Fig. 6.5). The SG/OH* images show that the heat release increases until the flame reaches the wall (not shown). Then, it stays fairly constant until the whole jet is covered by the flame at $t_{\mathrm{SOI,NG}} = 2.7\,\mathrm{ms}$. In contrast to the freely propagating gas jet, the heat release rate does not increase constantly until all premixed fuel is consumed. Instead, conversion is limited while the flame propagates along the concave wall segment. Premixed combustion of the jet tip shows no soot luminescence, while at the same time soot formation is already visible close to the wall. A sharp boundary develops in between the premixed reaction zone at the tip and the sooting zone further upstream. The soot-contaminated zone subsequently expands towards the outer jet shear layer.

If the degree of premixing is further increased ($\Delta t_{\mathrm{SOI}} = -1.5\,\mathrm{ms}$), ignition at the jet tip is observed for the first time shortly after ignition close to the orifice. Since natural gas injection has not yet ended at the time of ignition, the flame spreads rapidly in the upstream part while at the same time the premixed fuel at the tip is consumed as well. This causes a very high peak heat release rate at $t_{\mathrm{SOI,NG}} = 3.2\,\mathrm{ms}$. Despite the strong premixing and in accordance with the observations at the freely propagating jet, soot formation is visible despite the strong premixing as a result of ignition prior to EOI in the upstream region.

When ignition is even further delayed ($\Delta t_{\mathrm{SOI}} = -2.5\,\mathrm{ms}$), the maximum heat release rate drops again and an additional, slightly lower peak appears. As a result, the combustion duration is short while at the same time a high peak is avoided. Since ignition occurs late after EOI, the flame

[1]Realized by earlier natural gas injection relative to the fixed pilot injection in the experiment.

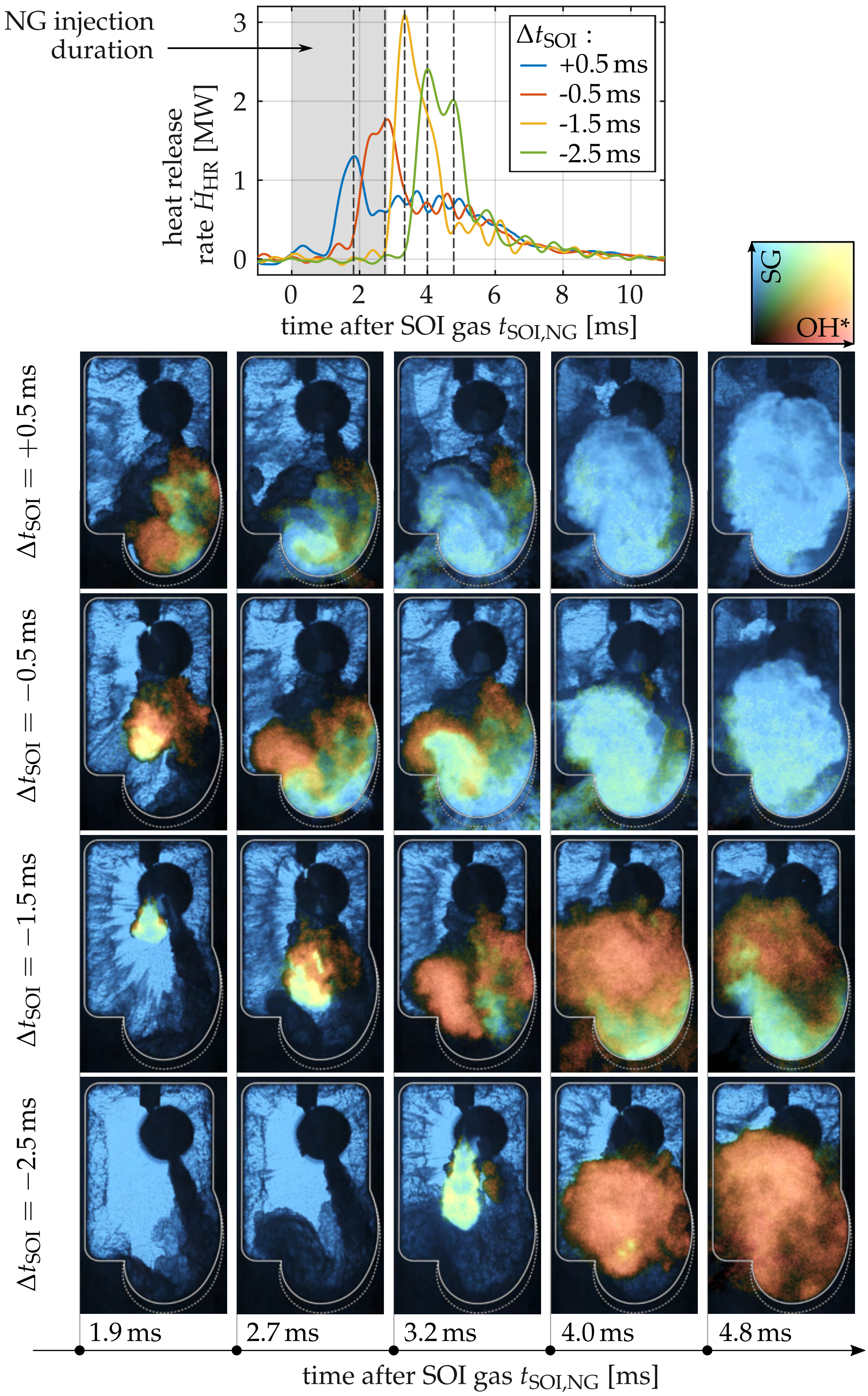

Figure 7.4: Variation of the relative injection timing Δt_{SOI} with the wall-bounded natural gas jet: heat release rates (top) and image sequences at the same times relative to natural gas SOI (bottom).

originating from the upstream ignition location spreads very slowly. At the same time, flame propagation from the jet tip towards the cavity is slow due to the opposed flow. When the heat release peaks the first time 4.0 ms after SOI, the rich zone close to the wall is not yet reached by the flame. The fuel in this zone can further mix and propagate away from the wall before it is consumed. Therefore no soot formation in the gas jet is observable at any time, and soot from the pilot fuel burns off completely when interacting with the premixed natural gas jet tip. This can be concluded since the only other explanation for the vanishing soot luminescence would be a considerable drop in temperature. However, the temperature within the reacting partially-premixed natural gas jet is well above 2000 K (see Fig. 7.1). Since the flame consumes the lean zones first and covers the whole jet area, unburnt CH_4 emissions are expected to be very low. An even more negative relative injection timing is not shown here, since in this case ignition of the very lean upstream region close to the injector orifice fails and a strong drop in combustion efficiency is expected.

7.2.3 Numerical Analysis

As previously for the freely propagating gas jet, the evolution of mixture distribution during combustion of the wall-bounded jet is analyzed in the ϕ-T space for low ($\Delta t_{\mathrm{SOI}} = +0.5\,\mathrm{ms}$) and strong premixing ($\Delta t_{\mathrm{SOI}} = -2.5\,\mathrm{ms}$). The comparison of the numerically and experimentally determined heat release rates in Fig. 7.5 proves the performance of the numerical model at altered conditions for mixing and reaction. Natural gas ignition ①, peak heat release ② and early burnout ③ are marked for each of the two cases individually. All three phases of combustion are represented in Fig. 7.6 by a pair of ϕ-T plots.

Prior to natural gas jet ignition at low premixing ($\Delta t_{\mathrm{SOI}} = +0.5\,\mathrm{ms}$) the fuel mass distribution is very similar to the one observed in a freely propagating jet (compare with Fig. 6.11). After ignition, the identified mechanism of mixture formation and reaction progress during ongoing injection (see Sec. 6.2.4) causes fuel accumulation at 1500-2000 K and $\phi > 2$ and promotes soot formation. Compared to the freely propagating jet, interaction with the wall further deteriorates air entrainment and causes the fuel distribution to

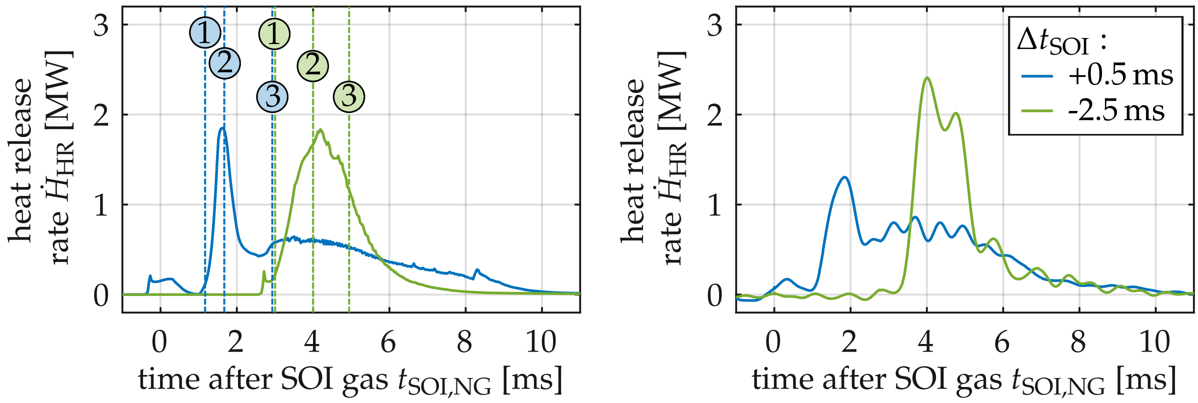

Figure 7.5: Numerically (left) and experimentally (right) determined heat release rates of wall-bounded natural gas jet combustion with low ($\Delta t_{SOI} = +0.5$ms) and strong premixing ($\Delta t_{SOI} = -2.5$ms).

extend towards even richer mixtures. Slower mixture formation is evident in the early burnout phase about 0.3 ms after EOI (3.0 ms after SOI), when the fuel distribution shows its maximum at $\phi = 3.5$ compared to $\phi = 2.5$ in case of the freely propagating jet (see Fig. 6.12). Since the partially oxidized mixture needs to detach from the wall in order to mix and react, burnout is very slow. This is not shown in a separate ϕ-T plot but can be recognized by the slowly decreasing heat release.

If the natural gas jet is strongly premixed ($\Delta t_{SOI} = -2.5$ ms), injection has already been terminated at the time of ignition, the entrainment wave has caused regions with $\phi > 2.2$ to quickly disappear and the fuel distribution shows its maximum at $\phi = 1.3$. A direct comparison of the top right to the bottom left plot in Fig. 7.6 at the same time after natural gas SOI impressively illustrates how much faster mixture formation proceeds if the jet is not reacting. The small amount of fuel indicating high C_2H_2 concentration can be attributed to diesel pilot fuel burnout. As shown by the experimental results, soot formed in the pilot jet is quickly oxidized. Only mixtures with $\phi < 1.5$ are involved in the NG reaction, even though there are still regions with up to $\phi = 2.2$ present. Mostly lean and stoichiometric mixtures are consumed up to the peak heat release rate, while the richer zones can further mix with air. A considerable amount of lean premixed ($\phi < 0.5$) and unburnt fuel is still present at in the early burnout phase. This is mainly due to missing confinement of the single jet on the side facing the piston and not to be expected in a full-scale engine configuration including neighboring jets.

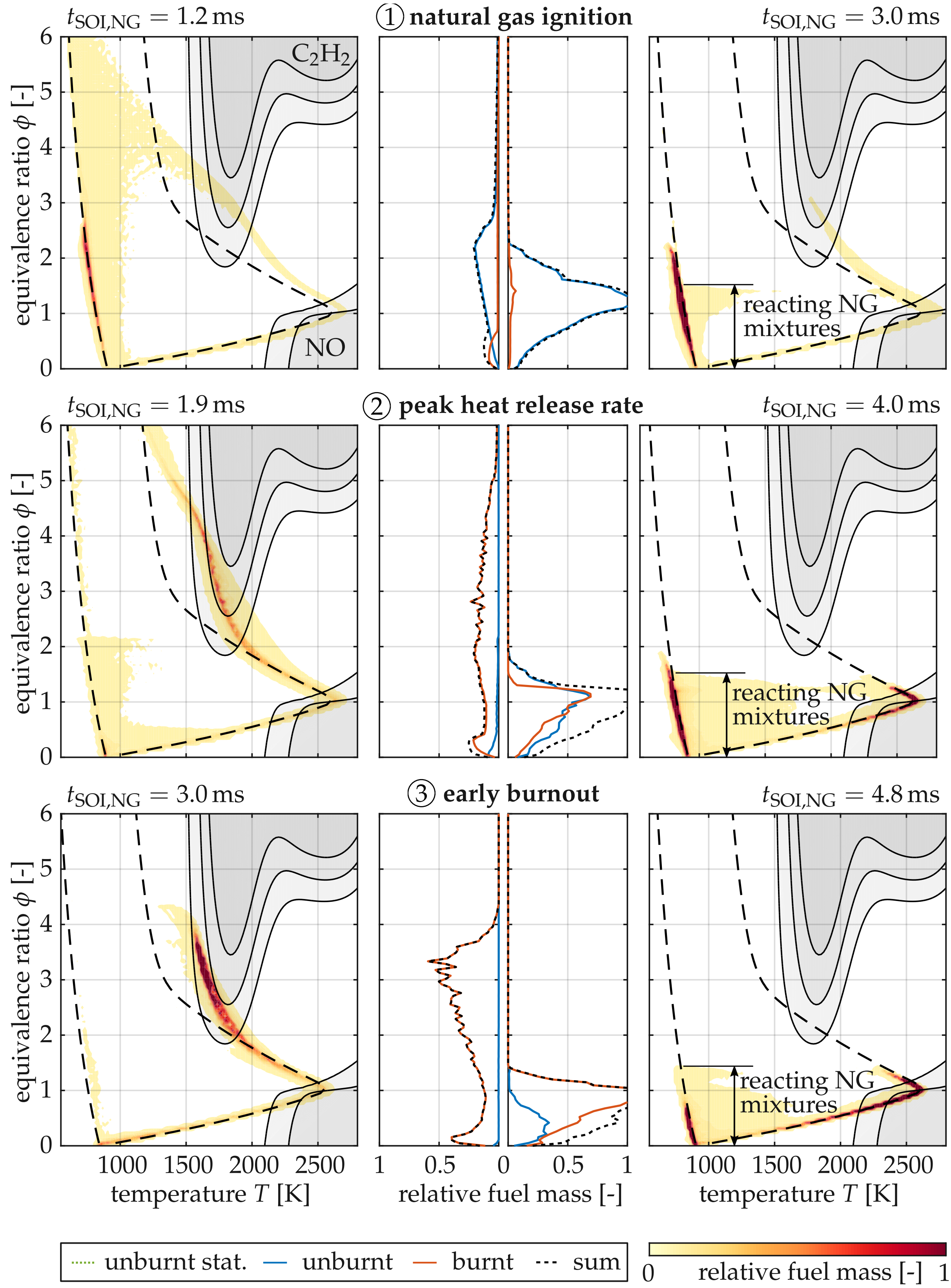

Figure 7.6: ϕ-T plots and burnt/unburnt mixture distribution for low (left: $\Delta t_{SOI} = +0.5$ ms) and strong premixing (right: $\Delta t_{SOI} = -2.5$ ms) of the wall-bounded natural gas jet; timing marked in Fig. 7.5.

The analysis shows that the full potential of wall-bounded partially-premixed HPDF may only be realized if the gas jet is ignited after natural gas EOI. This is necessary to eliminate soot formation as well as to limit the maximum heat release rates while still retaining a short combustion duration. For the presented wall design and jet arrangement, this corresponds to a relative injection timing of less than $\Delta t_{\mathrm{SOI}} \approx -2.0\,\mathrm{ms}$. However, exact relative injection timing is crucial: Too early ignition will cause harsh combustion and an increase in particle emissions. If ignition occurs too late, a significant increase in CH_4 emissions must be expected due to failing ignition of the lean region close to the injector.

7.2.4 Partially-Premixed Combustion at Part Load

Since the compression speed of the RCEM was not changed in any of the experiments, a load reduction can be implemented by simply lowering the injected natural gas fuel mass from 80 mg ($w_{\mathrm{NG}} = 100\%$) to 56 mg ($w_{\mathrm{NG}} = 70\%$) and 40 mg ($w_{\mathrm{NG}} = 50\%$). This is realized by reducing the injection duration at a constant injection pressure from 2.7 ms to 2.0 ms and 1.55 ms.

The previous section has shown that it is crucial to ignite the natural gas jet in a narrow time interval after EOI for partially-premixed HPDF combustion. This means that at different load points the timing of natural gas ignition must be kept constant with respect to EOI and that the relative injection timing Δt_{SOI} has to be adjusted (-2.0/-1.0/-0.5 ms). The heat release rates, fuel mass flow rates and image sequences in Fig. 7.7 are therefore plotted with respect to the individual time of natural gas ignition instead of SOI. Pilot fuel mass and injection duration are not altered in this investigation.

All three cases show ignition by direct jet interaction in the upstream region at the time when the first significant heat release is detected shortly after EOI ($t_{\mathrm{ign,NG}} = 0.0\,\mathrm{ms}$). With only half the natural gas fuel mass at $w_{\mathrm{NG}} = 50\%$, the gas jet is not yet deflected by the wall when injection is over and no ignition at the jet tip is observed. Since the reaction zone spreads slowly, the heat release rate shows its peak only about 1.2 ms after ignition when the tip is reached. Burnout proceeds rapidly and without

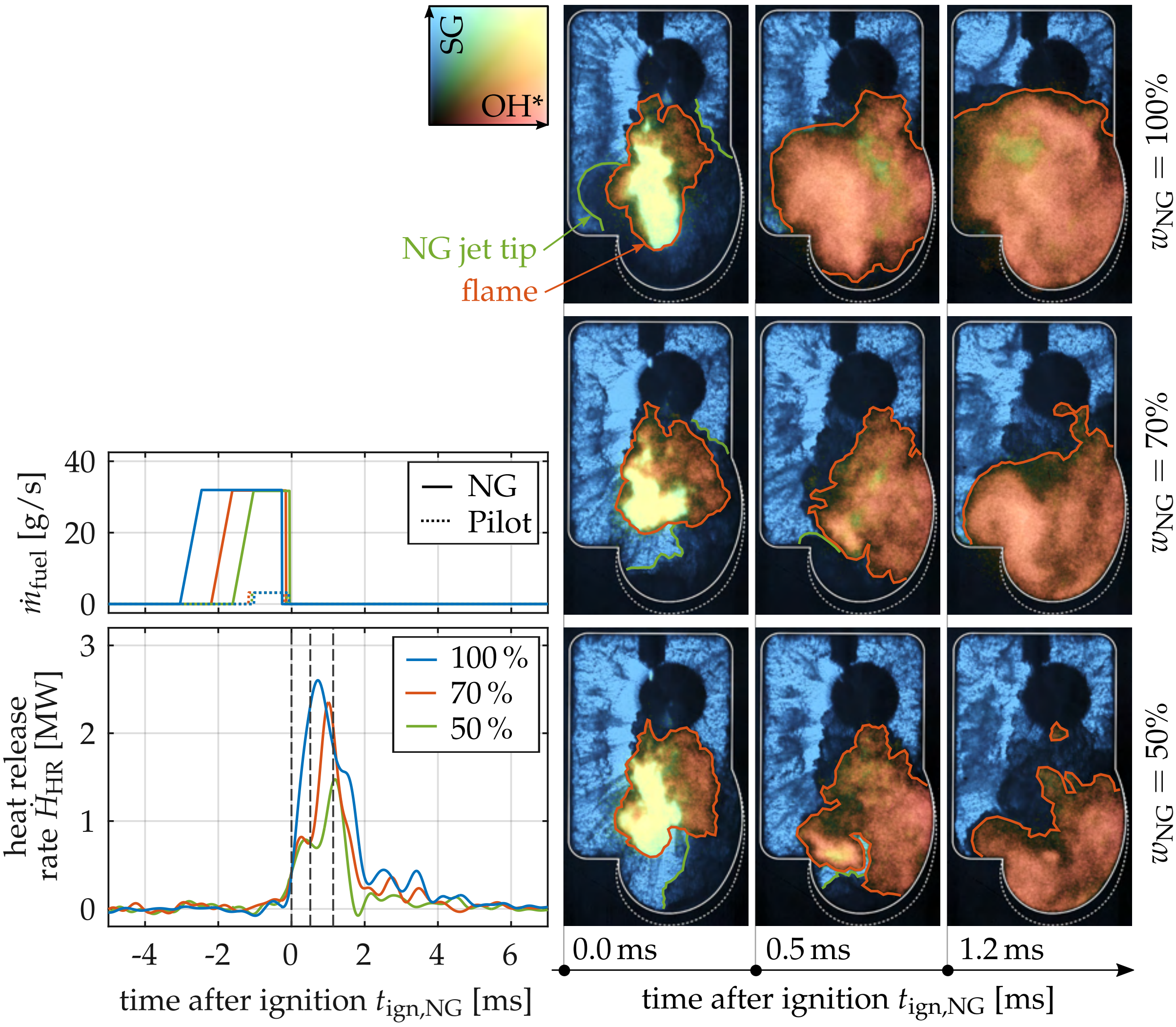

Figure 7.7: Fuel mass flow rates, heat release rates and image sequences showing the impact of load reduction by shorter natural gas injection duration on partially-premixed HPDF; note that all data is shown relative to the time of natural gas ignition.

soot luminescence. An increase to $w_{NG} = 70\%$ allows the jet to penetrate further until ignited by the pilot fuel close to the orifice at first and then at its tip as well about 0.5 ms later. This results in an earlier and stronger peak in heat release associated with combustion of the tip vortex about 1.0 ms after gas jet ignition. With the full amount of natural gas, the tip has already left the concave wall segment by the time of natural gas jet ignition. Thus ignition occurs at both locations at the same time. The maximum heat release associated with reaction at the jet tip is observed even earlier but is only slightly higher than with $w_{NG} = 70\%$. When the heat release rate drops again after the peak, a small plateau appears at $\dot{H}_{HR} = 1.5$ MW about 1.2-1.6 ms after ignition. This correlates with the time when the flame reaches the rich zone close to the wall in the outermost part of the cavity. The full load case in Fig. 7.7 is realized with a relative injection timing of $\Delta t_{\mathrm{SOI}} = 2.0\,\mathrm{ms}$. A comparison with Fig. 7.4 shows that slightly later ignition with $\Delta t_{\mathrm{SOI}} = 2.5\,\mathrm{ms}$ would reduce the first peak and increase the amount of fuel consumed during the second combustion phase.

Even though the relative injection timing was not optimized for each load point in this study, the results show a limited effect of the poorer jet deflection on the combustion characteristics with the specific wall design. Therefore, also the general emission characteristics are assumed to be similar as well. This is important since it indicates that one single pollutant emission reduction strategy – including e.g. EGR, particulate filters, UHC oxidation or NO reduction catalysts – is well suited for the whole engine load map.

8 Phenomenological Description of HPDF Combustion

In this Chapter, the findings from the various investigations in Ch. 5 to 7 are combined to formulate a generalized description of conventional HPDF combustion, as well as of partially-premixed HPDF combustion with a wall-bounded natural gas jet. The type of representation is inspired by the phenomenological descriptions of diesel combustion available in the literature, like the ones introduced in Sec. 2.2. By employing sketches of spatial fuel distribution, reaction progress and pollutant formation in combination with representative heat release rates, these descriptions are intended to cover the governing physical processes and correlations without the ambition of representing the optimum configuration.

For the graphical representation of HPDF combustion diesel-like high compression ratios, an angle of $\alpha = +20°$ between the jet axes and a natural gas injection pressure of 330 bar were selected. However, the phenomenological descriptions are also applicable to different combustion chamber conditions, jet arrangements and natural gas injection pressures since the effect of these parameters is covered as well. The applicability is limited to medium-speed large-bore engines with a piston bowl diameter of 100-150 mm due to the combustion chamber dimensions, the injected fuel mass and the injection duration of the experimental investigations they are based on. It is presumed that both fuels are injected into the combustion chamber via one single injector located centrally in the combustion chamber.

8.1 Conventional HPDF Combustion

Following the terminology used for diesel combustion, conventional HPDF refers to predominantly mixture-limited combustion of the directly injected natural gas. This is realized by early gas jet ignition due to direct interaction with the pilot fuel jets. Direct interaction means that the jets interact freely and unaffected by the combustion chamber wall. For any angle between the jet axes, the earliest possible natural gas ignition is achieved at a relative injection timing Δt_{SOI} of about +0.5 ms to +1.0 ms (see Fig. 6.6). Diesel pilot injection is thus started first and the pilot fuel ignites slightly prior to the natural gas SOI. Figure 8.1 shows the characteristic heat release rate for conventional HPDF with $\Delta t_{\mathrm{SOI}} = +0.5\,\mathrm{ms}$ along with sketches that illustrate the spatial evolution of mixing, reaction and soot formation.

The diesel pilot fuel ignites while pilot injection is still ongoing about 0.35 ms after SOI, despite the small amount and short injection duration (see Sec. 5.1). This means that the mixture dwell is negative and thus the pilot fuel combustion until EOI is covered by existing descriptions of conventional diesel combustion (see Sec. 2.2.1). Following the reduction in pilot mass flow rate at EOI, an entrainment wave forms at the orifice and propagates rapidly towards the pilot jet tip. While burnout close to the orifice is fast, it takes until $t_{\mathrm{SOI,NG}} = +1.4\,\mathrm{ms}$ for the soot at the pilot jet tip to disappear. Right before soot oxidation at the diesel pilot is about to be completed, natural gas ignition occurs at $t_{\mathrm{SOI,NG}} = +1.2\,\mathrm{ms}$. Due to the weak interaction between the jets at $\alpha = 20°$, pilot burnout can proceed almost undisturbed without the partially-oxidized mixture being entrained by the natural gas jet. A more intense interaction would not only increase particle emissions from pilot fuel combustion, but more importantly those from natural gas combustion as well (see also Fig. 6.9). Whether this is due to the reduced air entrainment only, or whether the partially oxidized diesel products additionally intensify soot formation in the natural gas jet remains unclear [39].

The strong entrainment of the natural gas jet assures reliable natural gas ignition by the diesel pilot only 10-15 mm ($9 - 14\,d$) downstream of the orifice (see also Fig. 6.2), despite the diverging jet axes. The NG jet's cross-section at this location shows a wide range of equivalence ratios, all of them

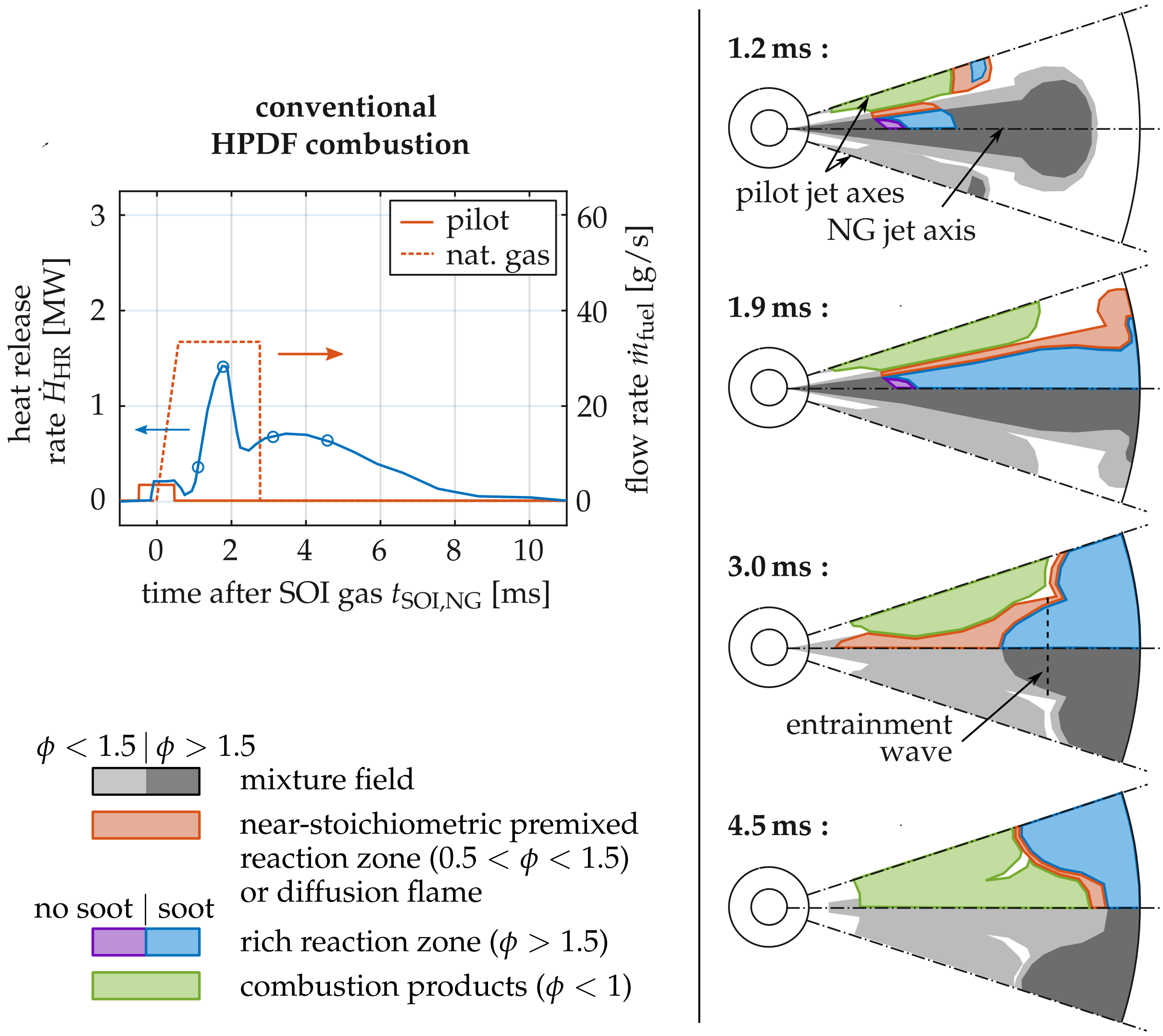

Figure 8.1: Fuel injection rates, heat release rates and simplified representation of the mixture and reaction field for a phenomenological description of conventional HPDF combustion.

being involved in the reaction when the reaction zone extends from the shear layer to the jet axis right after ignition (see Fig. 6.11). The rich reaction zone at the center of the gas jet – where soot luminescence is observed already at this early stage of combustion – spreads quickly towards the jet tip due to the high flow velocities. OH* chemiluminescence indicates premixed reaction in the shear layer slightly further upstream from the tip(see e.g. Fig. 4.10).

Right after natural gas jet ignition, all injected fuel is directly supplied to a reacting zone. The simultaneous mixing and reaction progress leads to temperatures levels of 1500-2000 K for mixtures in the range of $\phi = 2 - 5$, significantly hotter than the respective adiabatic flame temperature (see Fig. 6.13). It is this temperature range where rich mixtures show the strongest soot formation. The fact that air entrainment is lower in a reacting jet compared to a non-reacting jet furthermore causes a high share of fuel to be present at rich conditions and slows down soot oxidation. As a result, conventional HPDF generally shows relatively high engine-out PM emissions despite the low C/H-ratio of natural gas.

Since very rich mixtures with $\phi > 5$ are involved in the reaction (see Sec. 6.2.4), a reaction zone without significant soot concentration is expected to be present close to the lift-off length at the center of the jet. However, it is assumed that the strong turbulent transport quickly distributes any soot within the jet, causing the size of the rich reaction zone without soot to be very limited. The presence and extent of this zone could not be validated with the experimental results. Even if a mixture at such high equivalence ratios contains soot, natural luminescence in the visible range is low due to the low reaction temperature.

As a result of the fast spread of the flame towards the partially-premixed jet tip, the heat release rate increases sharply and peaks as soon the reaction zone extends across the whole jet at $t_{\mathrm{SOI,NG}} = +1.9$ ms. Subsequently, there is no unburnt mixture left except close to the the natural gas lift-off length, and the heat release drops again rapidly. While a turbulent diffusion flame has already been established in the upstream part of the jet during the propagation phase, it is now being formed at the jet tip as well. The soot-containing rich reaction zone expands to the outer part of the shear layer where this diffusion flame is located (see e.g. Fig. 7.4).

Before the jet tip is reached by the flame, impingement on the combustion chamber wall deteriorates mixture formation. Compared to a freely propagating jet, the heat release rate is thereby reduced during premixed combustion already and stays lower until the end of injection (see Fig. 7.3). The burnout phase after EOI is significantly influenced by the interaction with the chamber wall as well. At $t_{\mathrm{SOI,NG}} = +3.0$ ms, the entrainment wave has caused rapid oxidation of the freely propagating upstream part of the jet. The burnout rate now depends on the extent to which the wall contour design allows the soot-containing rich zones along the wall to lift off, thereby increasing the surface area of the diffusion flame and improving air supply. Even with a quickly detaching wall-bounded gas jet burnout is very slow and the heat release rate does not decline until about 2 ms after EOI at $t_{\mathrm{SOI,NG}} = +4.5\,\mathrm{ms}$.

Reducing the angle α between the pilot and gas jet axes below 20° results in a stronger interaction and therefore causes earlier ignition of the natural gas jet with respect to SOI. However, the ignition location relative to the injector orifice changes only slightly and flame propagation towards the jet tip is only marginally affected as well (see Sec. 6.1). This is the reason why the shape of heat release after ignition by direct jet interaction depends only on the ignition timing relative to SOI and thus on the degree of premixing of the gas jet, no matter what jet arrangement and relative injection timing have led to that ignition timing (see Sec. 6.2.1). If ignited earlier, the flame propagates along a gas jet that has not yet penetrated as far, causing the maximum heat release rate to be reduced and the phase of mixture-limited combustion to be extended. The phenomenological description of conventional HPDF combustion is therefore valid for a lower angle α between the jet axes as well, even though the timing and magnitude of each phase are different. As a result of the higher share of mixture-limited burnout and the more intense entrainment of partially-oxidized diesel fuel into the gas jet, higher particle emissions and slightly reduced NO emissions can be expected at a lower angle between the jet axes.

The influence of injection pressure has to be discussed in combination with the nozzle diameter and therefore also with the resulting injection duration. Even though the mean injection rate is kept constant when the natural gas injection pressure is increased while reducing the nozzle diameter to maintain the same injection duration, mixture formation is improved. Self-similarity of the jet at constant injection rate suggests the mixture distribution to be mainly affected during the start and after the end of injection. The higher injection pressure improves initial mixture formation by a faster needle lift of the hydraulically actuated injector and amplifies the entrainment wave after EOI. As a result of the faster initial mixing, premixed combustion with conventional HPDF injection timing is more intense. But since the natural gas jet can be ignited earlier, this does not necessarily result in higher peak heat release rates (see Sec. 6.2.2). After

EOI faster mixing and burnout translates into a faster decrease in heat release and in soot luminescence.

A lower temperature and pressure in the combustion chamber by e.g. early injection during compression or due to a lower compression ratio affects pilot ignition as well as natural gas combustion. If a longer ignition delay causes the diesel mixture dwell to become positive, soot formation in the pilot jet can be avoided (partially-premixed diesel pilot combustion, see Sec. 2.2.2 and Fig. 5.2). However, pilot ignition becomes less stable and any disturbance of the mixture field by strong interaction with the gas jet can inhibit pilot ignition at all (see Sec. 5.3). A lower charge temperature also reduces soot formation during natural gas combustion by shifting the upper burning limit to leaner mixtures and increasing the lift-off length. Since the natural gas ignition timing is decoupled from pilot fuel auto-ignition, conventional HPDF operation is not limited to high temperatures and pressures in the combustion chamber – as it is the case for conventional diesel combustion.

8.2 Wall-Bounded Partially-Premixed HPDF Combustion

Conventional mixture-limited HPDF combustion shows some general drawbacks. Fuel-supply to the reacting jet is responsible for an intense soot formation mechanism since it leads to rich mixtures at temperatures above equilibrium. Furthermore, the air entrainment is reduced if the jet is reacting. A high natural gas injection pressures is required to guarantee fast burnout for low particle emissions and high thermal efficiency. In contrast, soot formation can be prevented first hand if the natural gas is homogeneously premixed as for example with low-pressure dual-fuel (LPDF) combustion. However, the knocking limit of a premixed charge restricts high compression ratios and quenching in the corners and crevices of the combustion chamber causes a considerable amount of unburnt CH_4 in the exhaust stream (see Sec. 1.1).

Direct injection of both fuels allows full control over the natural gas ignition timing with respect to SOI and thus to freely adjust the degree of premixing. If the natural gas jet is ignited after EOI, the soot formation mechanism

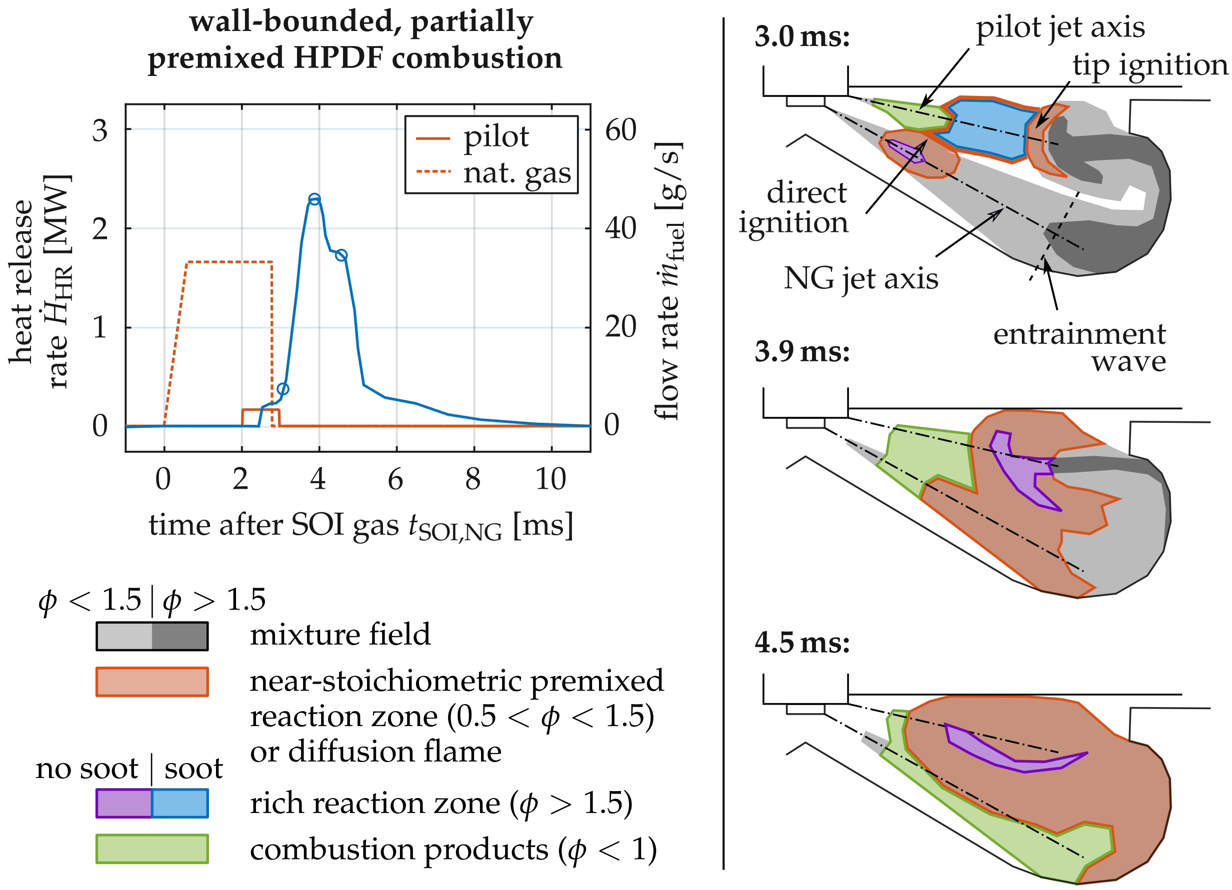

Figure 8.2: Fuel injection rates, heat release rates and simplified representation of the mixture and reaction field for a phenomenological description of wall-bounded partially-premixed HPDF combustion.

that dominates in conventional HPDF can be avoided. At the same time the stratified mixture ensures that no lean cold zones can form in the corners and crevices of the combustion chamber. This combustion strategy is termed partially-premixed HPDF. Due to late ignition, the mixture field is strongly affected by the interaction of the unburned gas jet with the chamber wall, which makes it impossible to formulate a generalized description for partially-premixed HPDF. Therefore, the phenomenological description presented here and illustrated in Fig. 8.2 refers to the special case of wall-bounded, partially premixed HPDF only. The wall contour is designed to guide the natural gas jet back to the center of the combustion chamber. This causes a second ignition location at the jet tip and also improves air entrainment after wall impingement. As for conventional HPDF the jet axes are arranged with low spatial overlap at $\alpha = 20°$ for maximum air utilization.

The diagram in Fig. 8.2 shows that diesel pilot fuel is injected and ignites while natural gas injection is still ongoing. The strong flow field of the natural gas jet therefore is still able to act on the pilot jet. As a consequence, natural gas ignition by direct interaction occurs shortly after EOI at $t_{\mathrm{SOI,NG}} = 3.0\,\mathrm{ms}$ close to the injector orifice. The entrainment wave caused by the fuel mass flow rate ramp-down at EOI has already passed the upstream ignition location at this time. The axial flow velocity is therefore low and the natural gas mixture becomes lean very quickly. As a result, flame propagation is slow in the wake of the entrainment wave, while at the same time over-mixing is successfully inhibited.

Already prior to the end of natural gas injection, deflection by the wall contour has caused the natural gas jet tip to be redirected towards the diesel pilot jet. While entrainment is low directly at the wall, it is improved again as the tip detaches. The natural gas jet tip is ignited by the pilot approximately at the same time when ignition occurs in the upstream region. Flame propagation within the tip vortex is fast, causing a sharp increase and peak in heat release rate at $t_{\mathrm{SOI,NG}} = 3.9\,\mathrm{ms}$. Over-stoichiometric zones are still present at the tip and involved in the reaction (see Fig. 7.6). But since no further fuel is supplied and mixing continues, luminescence from soot is too low to be detected. Moreover, the soot from pilot fuel combustion is quickly oxidized when interacting with the natural gas jet tip.

Subsequently, the flame spreads from both ignition locations towards the chamber wall. Propagation is relatively slow since in the upstream region the flame has to develop in a lean mixture and is assisted by only low flow velocity, and in the tip region the flame propagates against the flow velocity. As a result the heat release rate drops slightly. Once the flame covers the entire cavity at $t_{\mathrm{SOI,NG}} = 4.5\,\mathrm{ms}$, a second slightly lower plateau in heat release can be observed. Subsequently, the heat release rate drops sharply and the burnout phase begins. Since the low amount of remaining rich mixture is located in the center of the combustion chamber, burnout is fast and accompanied by only low heat release.

Exact control of injection timing is crucial for partially premixed wall-bounded HPDF. If natural gas ignition by direct interaction occurs prior to or during the passage of the entrainment wave, fast flame propagation along the jet axis causes the downstream premixed fuel to react in a short period of time and the resulting heat release rates are very high (see Fig. 7.4). If on the other hand the pilot fuel is injected too late, ignition of the very lean natural gas mixture close to the orifice fails and an increase in unburnt CH_4 emissions is to be expected. Ignition in this upstream region by direct jet interaction furthermore guarantees partially-premixed wall-bounded HPDF to be applicable at low load as well, when the natural gas jet momentum is reduced and jet deflection is insufficient for ignition at the tip (see Sec. 7.2.4).

Premixing of the natural gas is associated with an increase in NO emissions due to higher combustion temperatures. However, literature shows that exhaust gas recirculation (EGR) is particularly suitable for NO mitigation in combination with partially-premixed HPDF, since the trade-off between particle matter and NO emissions known from conventional diesel or conventional HPDF combustion does not apply [22, 57, 62]. EGR furthermore lowers the flame velocity and thus reduces combustion harshness. Even though the effect of EGR on partially-premixed wall-bounded HPDF was not covered by this study, its impact on the phenomenological description is assumed to be very limited.

9 Summary and Conclusion

This thesis presents an experimental investigation of diesel-piloted combustion of natural gas jets at conditions as they occur in internal combustion engines that employ high-pressure dual-fuel combustion (HPDF). Even though most heavy-duty engines today are still fuelled with diesel, the requirement for cleaner and more sustainable power systems drives the introduction of new fuels. Natural gas is an attractive alternative since it contains none or only very little sulphur and allows considerably reduced CO_2 emissions due to its low C/H-ratio. Most frequently, natural gas is supplied to the combustion chamber homogeneously mixed with air. Unfortunately, the premixed charge limits engine performance in terms of power density and thermal efficiency at part load, and additionally entails unburnt methane emissions. Direct injection of natural gas allows to close the performance gap while avoiding the emission of strongly climate-active methane. However, a lack in understanding of the physical processes that govern HPDF combustion prevents realization of its full potential. Hence, the experimental investigations in this work were designed to allow in-depth thermodynamic analyses and optical observations at precisely defined conditions, as well as to ensure parametric flexibility for a comprehensive analysis.

Experiments were conducted on a large-bore rapid compression-expasion machine (RCEM) with a quartz glass piston driven by compressed air. The RCEM was equipped with one separate injector for each fuel, and both injector nozzles were provided with only one single orifice. In combination with a flexible mount of the natural gas injector, this enables the variable arrangement of the fuel jets relative to each other without exchange of any equipment. A thermodynamic model of the combustion chamber capable of reproducing the heat losses in the RCEM for accurate calculation of the heat released by combustion of a small amount of fuel was successfully developed. In addition to the measurements required for thermodynamic analysis, an optical setup for simultaneous high-speed shadowgraph and OH* imaging was applied. By superposition of these images the non-reacting jets, the flame position and soot occurence can be localized. The experimental investigations were complemented by an analysis of results from CFD simulations with a numerical model whose development was not part of this work.

At first, auto-ignition and combustion of a very small amount of diesel pilot fuel (micro-pilot) was studied individually without natural gas injection. Depending on whether ignition occurs prior to or after the end of injection, the pilot either burns off mainly mixture-limited or partially-premixed. Based on this characterization, the operating conditions for all dual-fuel experiments were set to include the different modes of diesel pilot combustion. Furthermore, all dual-fuel experiments assumed both fuels to be supplied via a single injector with closely located nozzle orifices. Under these constraints, the influence of the natural gas jet on pilot fuel auto-ignition was assessed. It was found that ignition only occurs if the diesel fuel can penetrate freely up to the lift-off length without being disturbed and fully entrained by the gas jet. This finding was then used for an analysis of the location of natural gas jet ignition and of the pilot's effect on initial flame propagation in the gas jet. Independent of the jet arrangement and relative injection timing the natural gas jet is ignited at an almost invariable ignition location, governed by the pilot lift-off length and the strong entrainment of the natural gas jet. Moreover, initial flame propagation after successful natural gas ignition is only marginally affected by the interaction with the pilot jet and thus by the amount of pilot fuel entrained. This is a strong indication that reaction progress is predominantly governed by the degree of natural gas jet premixing, irrespective of jet interaction.

Direct scaling of the heat release with the degree of premixing was successfully demonstrated when characterizing the combustion of a freely propagating natural gas jet. The time between start of natural gas injection and ignition was selected as an appropriate parameter to quantify the mixing progress. This kind of self-similarity only applies at constant injection parameters and unaltered conditions in the combustion chamber. If the natural gas injection pressure is varied at a constant mean injection rate, the characteristic heat release is mainly affected by the injection pressure's effect on mixture formation following mass flow ramp-up and ramp-down. Therefore, higher injection pressures result in earlier, more intense premixed combustion and faster burn-out. The conditions in the combustion chamber influence the heat release by shifting the combustion limits, which determine the amount of fuel consumed during premixed flame propagation. Numerical analysis of the simultaneous mixture formation and reaction progress showed that the entire range of mixture qualities is involved in the reaction immediately after ignition of the natural gas. While the flame is carried towards the jet tip, the upstream rich zones are consumed first.

The analysis of fuel distribution in the ϕ-T space was also used to identify the soot formation process in the natural gas jet. Since the jet is covered by a diffusion flame, fuel supplied to the core can only become leaner by gradual mixing with the reaction products from the jet's shear layer. This causes the rich jet core to show temperatures considerably higher than the equilibrium adiabatic flame temperature. It is the resulting temperature range of 1500-2000 K where soot formation is most intense. Moreover, air entrainment by the jet is impaired as a direct consequence of the reaction – causing soot burnout to be slow and particle matter emissions to be high. The only way to effectively escape the mechanism is by ignition after injection has already ended, which implies considerable premixing. In addition to the theoretical analysis, experimental investigations were able to demonstrate how other parameters like the injection pressure, chamber conditions and interaction with the pilot jet affect soot formation due to their impact on mixture formation and reaction progress.

In the combustion chamber of a reciprocating engine jet impingement on the wall restricts propagation, thus impeding mixture formation and impairing combustion progress. But since wall interaction cannot be avoided anyway, it may be designed to tailor the spatial fuel distribution. Based on the characterization of ignition and combustion with free propagation, design guidelines for HPDF with a wall-bounded natural gas jet were formulated and then applied to the wall design. The resulting wall contour causes the jet to detach again from the wall after gradual deflection, improving mixture-limited burn-out for conventional HPDF with minimum premixing. If partially-premixed combustion is applied to the wall-bounded gas jet, the deflection causes a second ignition location at the tip of the jet. Slow flame propagation towards the wall limits the maximum heat release rate and reduces combustion harshness. Since the leanest zones are consumed first, they are prevented from further mixing with air and therefore contribute less to unburned CH_4 emissions. Finally, wall-bounded partially-premixed combustion was shown to be applicable at part load as well when lower fuel jet momentum reduces jet deflection.

The design process for wall-bounded HPDF combustion demonstrates how the insights from the fundamental investigations with only one single jet pair can be used for very specific design optimization tasks. Even more so, the broad but in-depth investigations facilitate a comprehensive understanding of HPDF combustion. Therefore, phenomenological descriptions of conventional HPDF and of partially-premixed, wall-bounded HPDF were introduced. These provide a simplified schematic overview of the physical processes and are intended as a starting point for the discussion and further investigation of diesel-piloted natural gas direct injection in internal combustion engines.

Previous Publications

Wesentliche Teile dieser Dissertation wurden vom Autor bereits standardmäßig vorab als Konferenz- und Zeitschriftenbeiträge veröffentlicht [25,26,41,42]. Alle Vorveröffentlichungen sind entsprechend der gültigen Promotionsordnung ordnungsgemäß gemeldet. Sie sind deshalb nicht zwangsläufig im Detail einzeln referenziert. Vielmehr wurde bei der Referenzierung eigener Vorveröffentlichungen Wert auf Verständlichkeit und inhaltlichen Bezug gelegt.

Parts of this Ph.D. thesis were published by the author beforehand in conference proceedings, journal papers, and reports [25, 26, 41, 42]. All of these prior printed publications are registered according to the valid doctoral regulations. However, not all of them are quoted explicitly everywhere as they are part of this present work being official documents. Whether these personal prior printed publications were referenced, depended on maintaining comprehensibility and providing all necessary context.

Bibliography

[1] Aggarwal, S. K., Awomolo, O., and Akber, K., 2011. “Ignition Characteristics of Heptane–Hydrogen and Heptane–Methane Fuel Blends at Elevated Pressures”. *International Journal of Hydrogen Energy,* ***36***(23), pp. 15392–15402.

[2] Akihama, K., Takatori, Y., Inagaki, K., Sasaki, S., and Dean, A. M., 2001. “Mechanism of the Smokeless Rich Diesel Combustion by Reducing Temperature”. In SAE World Congress & Exhibition, Vol. 2001-01-0655 of *SAE Technical Paper Series*.

[3] Albrecht, U., Schmidt, P., Weindorf, W., Wurster, R., and Zittel, W., 2013. “Kraftstoffstudie: Zukünftige Kraftstoffe für Verbrennungsmotoren und Gasturbinen”. Tech. rep., Forschungsvereinigung Verbrennungskraftmaschinen (FVV) e.V.

[4] Anderson, M., Salo, K., and Fridell, E., 2015. “Particle- and Gaseous Emissions from an LNG Powered Ship”. *Environmental Science & Technology,* ***49***(20), pp. 12568–12575.

[5] Annand, W. J. D., 1963. “Heat Transfer in the Cylinders of Reciprocating Internal Combustion Engines”. *Proceedings of the Institution of Mechanical Engineers,* ***177***(1), pp. 973–996.

[6] Annand, W. J. D., and Ma, T. H., 1970. “Instantaneous Heat Transfer Rates to the Cylinder Head Surface of a Small Compression-Ignition Engine”. *Proceedings of the Institution of Mechanical Engineers,* ***185***(1), pp. 976–987.

[7] Atassi, N., Bore, J., and Charnay, G., 1993. “Transient Behavior of an Axisymmetric Turbulent Jet”. *Applied Scientific Research,* ***51***(1-2), pp. 137–142.

[8] Becker, K. H., Haaks, D., and Tatarczyk, T., 1974. "The Natural Lifetime of OH and its Quenching by Atomic Hydrogen". *Chemical Physics Letters,* ***25***(4), pp. 564–567.

[9] Benajes, J., Molina, S., Novella, R., and Belarte, E., 2014. "Evaluation of Massive Exhaust Gas Recirculation and Miller Cycle Strategies for Mixing-Controlled Low Temperature Combustion in a Heavy Duty Diesel Engine". *Energy,* ***71***, pp. 355–366.

[10] Borée, J., Atassi, N., and Charnay, G., 1996. "Phase Averaged Velocity Field in an Axisymmetric Jet Subject to a Sudden Velocity Decrease". *Experiments in Fluids,* ***21***(6), pp. 447–456.

[11] Borée, J., Atassi, N., Charnay, G., and Taubert, L., 1997. "Measurements and Image Analysis of the Turbulent Field in an Axisymmetric Jet Subject to a Sudden Velocity Decrease". *Experimental Thermal and Fluid Science,* ***14***(1), pp. 45–51.

[12] Breidenthal, R. E., 2008. "The Effect of Acceleration on Turbulent Entrainment". *Physica Scripta,* ***T132***(14001), p. 5 pp.

[13] Bruneaux, G., 2001. "A Study of Soot Cloud Structure in High Pressure Single Hole Common Rail Diesel Injection Using Multi-Layered Laser-Induced Incandescence". In Proceedings of the International Symposium on Diagnostics and Modeling of Combustion in Internal Combustion Engines (COMODIA), Vol. 01.204.

[14] Bruneaux, G., 2008. "Combustion Structure of Free and Wall-Impinging Diesel Jets by Simultaneous Laser-Induced Fluorescence of Formaldehyde, Poly-Aromatic Hydrocarbons, and Hydroxides". *International Journal of Engine Research,* ***9***(3), pp. 249–265.

[15] California Air Resources Board, 2017. "Heavy-Duty Engines and Vehicles, Including Urban Buses, and Engines Used in Diesel or Incomplete Medium-Duty Vehicles of 8501-14000 Pound GVWR – Executive Orders 2017". Tech. rep., *(https://ww3.arb.ca.gov/msprog/onroad/cert/mdehdehdv/2017/2017.php)*.

[16] Caretto, L., Fritz, S., Hedrick, J., Iden, M., Schmid, L., Stehly, M., Trump, A., Wheeles, D., and Weldon, S., 2007. "An Evaluation of Natural Gas-Fueled Locomotives". Tech. rep., BNSF Railway Company.

[17] Chepakovich, A. C., 1993. "Visualization of Transient Single- and Two-Phase Jets Created by Diesel Engine Injectors". Master's Thesis, University of British Columbia.

[18] Dec, J. E., 1997. "A Conceptual Model of DI Diesel Combustion Based on Laser-Sheet Imaging". In SAE International Congress & Exposition, Vol. 970873 of *SAE Technical Paper Series*.

[19] Dorer, F. S., 2000. "Kompressionsmaschine zur Simulation von Brennraumvorgängen in Wasserstoff-Grossdieselmotoren". PhD Thesis, Technische Universität München.

[20] Douville, B., Ouellette, P., Touchette, A., and Ursu, B., 1998. "Performance and Emissions of a Two-Stroke Engine Fueled Using High-Pressure Direct Injection of Natural Gas". In SAE International Congress and Exposition, Vol. 981160 of *SAE Technichal Paper Series*.

[21] Dumitrescu, S., Hill, P. G., Li, G., and Ouellette, P., 2000. "Effects of Injection Changes on Efficiency and Emissions of a Diesel Engine Fueled by Direct Injection of Natural Gas". In SAE Fuels & Lubricants Meeting & Exposition, Vol. 2000-01-1805 of *SAE Technical Paper Series*.

[22] Faghani, E., Kheirkhah, P., Mabson, C. W., McTaggart-Cowan, G., Kirchen, P., and Rogak, S., 2017. "Effect of Injection Strategies on Emissions from a Pilot-Ignited Direct-Injection Natural-Gas Engine – Part II: Slightly Premixed Combustion". In SAE World Congress & Exhibiton, Vol. 2017-01-0763 of *SAE Technical Paper Series*.

[23] Fiala, T., 2015. "Radiation from High Pressure Hydrogen-Oxygen Flames and its Use in Assessing Rocket Combustion Instability". PhD Thesis, Technische Universität München.

[24] Fiala, T., and Sattelmayer, T., 2013. "A Posteriori Computation of OH* Radiation from Numerical Simulations in Rocket Combustion

Chambers". In 5th European Conference for Aeronautics and Space Sciences (EUCASS).

[25] Fink, G., Jud, M., and Sattelmayer, T., 2018. "Influence of the Spatial and Temporal Interaction Between Diesel Pilot and Directly Injected Natural Gas Jet on Ignition and Combustion Characteristics". *Journal of Engineering for Gas Turbines and Power*, ***140***(10), p. 102811 (8 pages).

[26] Fink, G., Jud, M., and Sattelmayer, T., 2019. "Fundamental Study of Diesel-Piloted Natural Gas Direct Injection Under Different Operating Conditions". *Journal of Engineering for Gas Turbines and Power*, ***141***(9), p. 12568 (8 pages).

[27] Gaydon, A. G., and Wolfhard, H. G., 1970. *Flames: Their Structure, Radiation and Temperature*. Chapman and Hall.

[28] Ghaem-Maghami, E., and Johari, H., 2007. "Concentration Field Measurements Within Isolated Turbulent Puffs". *Journal of Fluids Engineering*, ***129***(2), pp. 194–199.

[29] Ghaem-Maghami, E., and Johari, H., 2010. "Velocity Field of Isolated Turbulent Puffs". *Physics of Fluids*, **22**(115105).

[30] Glezer, A., and Coles, D., 1990. "An Experimental Study of a Turbulent Vortex Ring". *Journal of Fluid Mechanics*, **211**, pp. 243–283.

[31] Harrington, J., Munshi, S., Nedelcu, C., Ouellette, P., Thompson, J., and Whitfield, S., 2002. "Direct Injection of Natural Gas in a Heavy-Duty Diesel Engine". In SAE Fuels & Lubricants Meeting & Exhibition, Vol. 2002-01-1630 of *SAE Technical Paper Series*.

[32] Hill, P. G., and Douville, B., 2000. "Analysis of Combustion in Diesel Engines Fueled by Directly Injected Natural Gas". *Journal of Engineering for Gas Turbines and Power*, **122**(1), pp. 141–149.

[33] Hill, P. G., and Ouellette, P., 1999. "Transient Turbulent Gaseous Fuel Jets for Diesel Engines". *Journal of Fluids Engineering*, **121**(1), pp. 93–101.

[34] Hindmarsh, A. C., Brown, P. N., Grant, K. E., Lee, S. L., Serban, R., Shumaker, D. E., and Woodward, C. S., 2005. "SUNDIALS: Suite of Nonlinear and Differential/Algebraic Equation Solvers". *ACM Transactions on Mathematical Software,* ***31***(3), pp. 363–396.

[35] Hodgins, K. B., Gunawan, H., and Hill, P. G., 1992. "Intensifier-Injector for Natural Gas Fueling of Diesel Engines". In SAE Future Transportation Technology Conference & Exposition, Vol. 921553 of *SAE Technical Paper Series*.

[36] Hodgins, K. B., Hill, P. G., Ouellette, P., and Hung, P., 1996. "Directly Injected Natural Gas Fueling of Diesel Engines". In SAE Future Transportation Technology Conference & Exposition, Vol. 961671 of *SAE Technical Paper Series*.

[37] Idicheria, C. A., and Pickett, L. M., 2006. "Formaldehyde Visualization Near Lift-off Location in a Diesel Jet". In SAE Powertrain & Fluid Systems Conference and Exhibition, Vol. 2006-01-3434 of *SAE Technical Paper Series*.

[38] Irimescu, A., 2013. "Convective Heat Transfer Equation for Turbulent Flow in Tubes Applied to Internal Combustion Engines Operated under Motored Conditions". *Applied Thermal Engineering,* ***50***(1), pp. 536–545.

[39] Jones, H. L., McTaggart-Cowan, G. P., Rogak, S. N., Bushe, W. K., Munshi, S. R., and Buchholz, B. A., 2005. "Source Apportionment of Particulate Matter from a Diesel Pilot-Ignited Natural Gas Fuelled Heavy Duty DI Engine". In SAE Fuels & Lubricants Meeting, Vol. 2005-01-2149 of *SAE Technical Paper Series*.

[40] Jud, M., 2019. "Numerische Simulation der Zündung und Verbrennung von mit Diesel pilotierten Erdgasstrahlen". PhD Thesis, Technische Universität München.

[41] Jud, M., Fink, G., and Sattelmayer, T., 2017. "Predicting Ignition and Combustion of a Pilot Ignited Natural Gas Jet Using Numerical Simulation Based on Detailed Chemistry". In Proceedings of the ASME 2017 Internal Combustion Engine Division Fall Technical Conference, Vol. ICEF2017-3533.

[42] Jud, M., Wieland, C., Fink, G., and Sattelmayer, T., 2018. "Numerical Analysis of the Combustion Process in Dual-Fuel Engines With Direct Injection of Natural Gas". In Proceedings of the ASME 2018 Internal Combustion Engine Division Fall Technical Conference, Vol. ICEF2018-9579.

[43] Karim, G. A., 2015. *Dual-Fuel Diesel Engines*. CRC Press.

[44] Kitamura, T., Ito, T., Senda, J., and Fujimoto, H., 2002. "Mechanism of Smokeless Diesel Combustion with Oxygenated Fuels Based on the Dependence of the Equivalence Ratio and Temperature on Soot Particle Formation". *International Journal of Engine Research, **3***(4), pp. 223–248.

[45] Kojima, J., Ikeda, Y., and Nakajima, T., 2005. "Basic Aspects of OH(A), CH(A), and C2(d) Chemiluminescence in the Reaction Zone of Laminar Methane–Air Premixed Flames". *Combustion and Flame, **140***, pp. 34–45.

[46] Kook, S., Bae, C., Miles, P. C., Choi, D., and Pickett, L. M., 2005. "The Influence of Charge Dilution and Injection Timing on Low-Temperature Diesel Combustion and Emissions". In SAE Powertrain & Fluid Systems Conference & Exhibition, Vol. 2005-01-3837 of *SAE Technical Paper Series*.

[47] Kosaka, H., Aizawa, T., and Kamimoto, T., 2005. "Two-Dimensional Imaging of Ignition and Soot Formation Processes in a Diesel Flame". *International Journal of Engine Research, **6***(1), pp. 21–42.

[48] Lauer, M. R. W., 2011. "Determination of the Heat Release Distribution in Turbulent Flames by Chemiluminescence Imaging". PhD Thesis, Technische Universität München.

[49] Lavoie, G. A., Heywood, J. B., and Keck, J. C., 1970. "Experimental and Theoretical Study of Nitric Oxide Formation in Internal Combustion Engines". *Combustion Science and Technology, **1***(4), pp. 313–326.

[50] Lawton, B., 1987. "Effect of Compression and Expansion on Instantaneous Heat Transfer in Reciprocating Internal Combustion

Engines". *Proceedings of the Institution of Mechanical Engineers, Part A: Power and Process Engineering,* ***201***(3), pp. 175–186.

[51] Lee, D., and Hochgreb, S., 1998. "Rapid Compression Machines: Heat Transfer and Suppression of Corner Vortex". *Combustion and Flame,* ***114***(3-4), pp. 531–545.

[52] Li, G., Ouellette, P., Dumitrescu, S., and Hill, P. G., 1999. "Optimization Study of Pilot-Ignited Natural Gas Direct-Injection in Diesel Engines". In SAE International Fuels & Lubricants Meeting & Exposition, Vol. 1999-01-3556 of *SAE Technical Paper Series*.

[53] Luque, J., and Crosley, D. R., 1998. "Transition probabilities in the electronic system of OH". *The Journal of Chemical Physics,* ***109***(2), pp. 439–448.

[54] Majewski, W. A., and Jääsekeläinen, H., 2018. "Methane Emission Control Catalysts". Tech. rep., DieselNet Technology Guide *(https://www.dieselnet.com/tech/catalyst_methane.php)*.

[55] MAN Diesel & Turbo, 2014. "ME-GI Dual Fuel MAN B&W Engines: A Technical, Operational and Cost-effective Solution for Ships Fuelled by Gas". Tech. rep.

[56] McBride, B. J., Gordon, S., and Reno, M. A., 1993. "Coefficients for Calculating Thermodynamic and Transport Properties of Individual Species". *NASA Technical Memorandum,* ***4513***.

[57] McTaggart-Cowan, G., Bushe, W. K., Hill, P. G., and Munshi, S. R., 2005. "NOx Reduction from a Heavy-Duty Diesel Engine with Direct Injection of Natural Gas and Cooled Exhaust Gas Recirculation". *International Journal of Engine Research,* ***5***(2), pp. 175–191.

[58] McTaggart-Cowan, G., Mann, K., Huang, J., Singh, A., Patychuk, B., Zheng, Z. X., and Munshi, S., 2015. "Direct Injection of Natural Gas at up to 600 Bar in a Pilot-Ignited Heavy-Duty Engine". *SAE International Journal of Engines,* ***8***(3), pp. 981–996.

[59] McTaggart-Cowan, G. P., 2006. "Pollutant Formation in a Gaseous-Fuelled, Direct Injection Engine". PhD Thesis, University of British Columbia.

[60] McTaggart-Cowan, G. P., Bushe, W. K., Rogak, S. N., Hill, P. G., and Munshi, S. R., 2003. "Injection Parameter Effects on a Direct Injected, Pilot Ignited, Heavy Duty Natural Gas Engine with EGR". In SAE Powertrain & Fluid Systems Conference & Exhibition, Vol. 2003-01-3089 of *SAE Technical Paper Series*.

[61] McTaggart-Cowan, G. P., Jones, H. L., Rogak, S. N., Bushe, W. K., Hill, P. G., and Munshi, S. R., 2007. "The Effects of High-Pressure Injection on a Compression–Ignition, Direct Injection of Natural Gas Engine". *Journal of Engineering for Gas Turbines and Power,* ***129***(2), pp. 579–588.

[62] McTaggart-Cowan, G. P., Mann, K., Huang, J., Wu, N., and Munshi, S. R., 2012. "Particulate Matter Reduction From a Pilot-Ignited, Direct Injection of Natural Gas Engine". In Proceedings of the ASME 2012 Internal Combustion Engine Division Fall Technical Conference, Vol. ICEF2012-92162.

[63] McTaggart-Cowan, G. P., Rogak, S. N., Munshi, S. R., Hill, P. G., and Bushe, W. K., 2009. "Combustion in a Heavy-Duty Direct-Injection Engine Using Hydrogen-Methane Blend Fuels". *International Journal of Engine Research,* ***10***(1), pp. 1–13.

[64] McTaggart-Cowan, G. P., Rogak, S. N., Munshi, S. R., Hill, P. G., and Bushe, W. K., 2010. "The Influence of Fuel Composition on a Heavy-Duty, Natural-Gas Direct-Injection Engine". *Fuel,* ***89***(3), pp. 752–759.

[65] Merker, G. P., and Teichmann, R., 2012. *Grundlagen Verbrennungsmotoren: Funktionsweise, Simulation, Messtechnik*. Springer Vieweg.

[66] Mittermayer, F., 2011. "CFD-Simulation der Zündung und Verbrennung in einem vorkammergezündeten Großgasmotor". PhD Thesis, Technische Universität München.

[67] Miyake, M., Biwa, T., Endoh, Y., Shimotsu, M., Murakami, S., and Komoda, T., 1985. "Development of High Output, Highly Efficient Gas Burning Engines". In Proceedings of the 15th International Congress on Combustion Engines, pp. 1193–1216.

[68] Murata, Y., Nishio, Y., Kusaka, J., Daisho, Y., Kawano, D., Suzuki, H., Ishii, H., and Goto, Y., 2010. "Numerical Analysis of Miller-Premixed Charge Compression Ignition Combustion on a Dynamic Phi-T Map". *International Journal of Engine Research,* ***11***(2), pp. 89–98.

[69] Musculus, M. P., Miles, P. C., and Pickett, L. M., 2013. "Conceptual Models for Partially Premixed Low-Temperature Diesel Combustion". *Progress in Energy and Combustion Science,* ***39***(2-3), pp. 246–283.

[70] Musculus, M. P. B., and Kattke, K., 2009. "Entrainment Waves in Diesel Jets". *SAE International Journal of Engines,* **2**(1), pp. 1170–1193.

[71] Musculus, M. P. B., Lachaux, T., Pickett, L. M., and Idicheria, C. A., 2007. "End-of-Injection Over-Mixing and Unburned Hydrocarbon Emissions in Low-Temperature-Combustion Diesel Engines". In SAE World Congress & Exhibition, Vol. 2007-01-0907 of *SAE Technical Paper Series*.

[72] Ouellette, P., 1996. "Direct Injection of Natural Gas for Diesel Engine Fueling". PhD Thesis, University of British Columbia.

[73] Pachauri, R. K., Myles R. Allen, Vicente R. Barros, et al., 2014. "Climate Change 2014: Synthesis Report. Contribution of Working Groups I, II, and III to the Fifth Assessment Report of the Intergovernmental Panel on Climate Change". Tech. rep., IPCC.

[74] Peters, N., 2000. *Turbulent Combustion*. Cambridge University Press.

[75] Pickett, L. M., Manin, J., Genzale, C. L., Siebers, D. L., Musculus, M. P. B., and Idicheria, C. A., 2011. "Relationship Between Diesel Fuel Spray Vapor Penetration/Dispersion and Local Fuel Mixture Fraction". *SAE International Journal of Engines,* **4**(1), pp. 764–799.

[76] Pickett, L. M., and Siebers, D. L., 2006. "Soot Formation in Diesel Fuel Jets Near the Lift-Off Length". *International Journal of Engine Research,* ***7***(2), pp. 103–130.

[77] Pischinger, R., Klell, M., and Sams, T., 2009. *Thermodynamik der Verbrennungskraftmaschine*. Springer.

[78] Poinsot, T., and Veynante, D., 2005. *Theoretical and Numerical Combustion*. R. T. Edwards.

[79] Prechtl, P., 2000. "Analyse und Optimierung der innermotorischen Prozesse in einem Wasserstoff-Dieselmotor". PhD thesis, Technische Universität München.

[80] Pribicevic, I., 2013. "Dieselmotorische Gemischbildung und Verbrennung bei Einspritzdrücken bis 300 MPa". PhD thesis, Technische Universität München.

[81] Reitz, R. D., and Beale, J. C., 1999. "Modelling Spray Atomization with the Kelvin-Helmholtz/Rayleigh-Taylor Hybrid Model". *Atomization and Sprays,* ***9***(6), pp. 623–650.

[82] Reitz, R. D., and Diwakar, R., 1987. "Structure of High-Pressure Fuel Sprays". In SAE International Congress and Exposition, Vol. 870598 of *SAE Technical Paper Series*.

[83] Richards, J. M., 1965. "Puff Motions in Unstratified Surroundings". *Journal of Fluid Mechanics,* ***21***(01), p. 97.

[84] Richards, K. J., Senecal, P. K., and Pomraning, E., 2016. "CONVERGE (v2.3) Manual". Tech. rep., Convergent Science, Inc.

[85] Ricou, F. P., and Spalding, D. B., 1961. "Measurements of Entrainment by Axisymmetrical Turbulent Jets". *Journal of Fluid Mechanics,* ***11***(1), pp. 21–32.

[86] Rizk, W., 2006. "Experimental Studies of the Mixing Processes and Flow Configurations in Two-Cycle Engine Scavenging". *Proceedings of the Institution of Mechanical Engineers,* ***172***(1), pp. 417–437.

[87] Rochussen, J., McTaggart-Cowan, G., and Kirchen, P., 2019. "Parametric Study of Pilot-Ignited Direct-Injection Natural Gas Combustion in an Optically Accessible Heavy-Duty Engine". *International Journal of Engine Research,* ***121***.

[88] Rolke, P., Fritsch, B., and Bärow, E., 2019. "Injection Rate Measurement System for Gas Injectors and Test Rig Analysis of Injectors for Medium Speed Engines". In Proceedings of the 11th

Dessau Gas Engine Conference, pp. 224–237.

[89] Sangras, R., Kwon, O. C., and Faeth, G. M., 2002. “Self-Preserving Properties of Unsteady Round Nonbuoyant Turbulent Starting Jets and Puffs in Still Fluids”. *Journal of Heat Transfer*, ***124***(3), p. 460.

[90] Schiffner, M., Jud, M., and Sattelmayer, T., 2017. “Reaction Kinetics Analysis of Dual Fuel Internal Combustion Engines Based on Ignition Delay Times Using n-Heptane/Methane Fuel Blends”. In Proceedings of the European Combustion Meeting, pp. 1005–1010.

[91] Schmidt, D. P., and Rutland, C. J., 2000. “A New Droplet Collision Algorithm”. *Journal of Computational Physics*, ***164***(1), pp. 62–80.

[92] Settles, G. S., 2006. *Schlieren and Shadowgraph Techniques: Visualizing Phenomena in Transparent Media*. Springer.

[93] Siebers, D. L., and Higgins, B., 2001. “Flame Lift-Off on Direct-Injection Diesel Sprays Under Quiescent Conditions”. In SAE World Congress & Exhibition, Vol. 2001-01-0530 of *SAE Technical Paper Series*.

[94] Smith, G. P., Golden, D. M., Frenklach, M., Moriarty, N. W., Eiteneer, B., Goldenberg, M., Bowman, C. T., Hanson, R. K., Song, S., Gardiner Jr, W. C., et al., 1999. “GRI 3.0 Mechanism”. *Gas Research Institute (http://combustion.berkeley.edu/gri-mech)*.

[95] Smith, T. W. P., Jalkanen, J. P., Anderson, B. A., Corbett, J. J., Faber, J., and Hanayama, 2015. “Third IMO GHG Study 2014”. Tech. rep., International Maritime Organization.

[96] Stenersen, D., and Thonstad, O., 2017. “GHG and NOx Emissions from Gas Fuelled Engines”. Tech. rep., SINTEF Ocean AS.

[97] Stocker, T. F., Qin, D., Plattner, G.-K., et al., 2013. *Climate Change 2013: the Physical Science Basis: Contribution of Working Group I to the Fifth Assessment Report of the Intergovernmental Panel on Climate Change*. Cambridge University Press.

[98] Tao, F., Reitz, R. D., and Foster, D. E., 2007. “Revisit of Diesel Reference Fuel (n-Heptane) Mechanism Applied to

Multidimensional Diesel Ignition and Combustion Simulations". In Seventeenth International Multidimensional Engine Modeling User's Group Meeting at the SAE World Congress & Exhibition.

[99] Taschek, M., Koch, P., Egermann, J., and Leipertz, A., 2005. "Simultaneous Optical Diagnostics of HSDI Diesel Combustion Processes". In SAE Powertrain & Fluid Systems Conference & Exhibition, Vol. 2005-01-3845 of *SAE Technical Paper Series*.

[100] Toepler, A., 1864. *Beobachtungen nach einer neuen optischen Methode: Ein Beitrag zur Experimental-Physik*. Max Cohen & Sohn.

[101] Turner, J. S., 1962. "The 'Starting Plume' in Neutral Surroundings". *Journal of Fluid Mechanics,* ***13***(3), pp. 356–368.

[102] Turns, S. R., 2012. *An Introduction to Combustion: Concepts and Applications*. McGraw-Hill.

[103] Unfug, F., 2016. "Investigation on Dual Fuel Engine Gas Combustion using Tomographic In-Cylinder Measurement Technique and Simultaneous High Speed OH-Chemiluminescence Visualization". In SAE International Powertrains, Fuels & Lubricants Meeting, Vol. 2016-01-2308 of *SAE Technical Paper Series*.

[104] Weber, S., Stegmann, R., Prager, M., and Wachtmeister, G., 2018. "The Effect of Inlet Valve Timing and Engine Speed on Dual Fuel NG-Diesel Combustion in a Large Bore Engine". *SAE International Journal of Engines,* ***11***(2), pp. 229–246.

[105] Witze, P. O., 1980. "The Impulsively Started Incompressible Turbulent Jet". Tech. rep., Sandia Laboratories.

[106] Witze, P. O., 1983. "Hot-Film Anemometer Measurements in a Starting Turbulent Jet". *AIAA Journal,* ***21***(2), pp. 308–309.

[107] Woschni, G., 1967. "A Universally Applicable Equation for the Instantaneous Heat Transfer Coefficient in the Internal Combustion Engine". In SAE National Fuels and Lubricants, Powerplants, Transportation Meetings, Vol. 670931 of *SAE Technical Paper Series*.

[108] Yakhot, V., and Orszag, S. A., 1986. "Renormalization Group Analysis of Turbulence. Basic Theory". *Journal of Scientific Computing*, ***1***(1), pp. 3–51.

[109] Zhang, Q., and Johari, H., 1996. "The Effects of Acceleration on Turbulent Jets". *Physics of Fluids*, ***8***(8), pp. 2185–2195.

[110] Zhao, H., 2010. *Advanced Direct Injection Combustion Engine Technologies and Development*. CRC Press.